

Magnetic Properties Near the Surface of Cuprate Superconductors Studied Using Beta-Detected NMR

by

Hassan Saadaoui

B.Sc., Université Mohammed Premier, 2001

M.Sc., Laurentian University, 2004

A THESIS SUBMITTED IN PARTIAL FULFILLMENT OF
THE REQUIREMENTS FOR THE DEGREE OF

DOCTOR OF PHILOSOPHY

in

The Faculty of Graduate Studies

(Physics)

THE UNIVERSITY OF BRITISH COLUMBIA

(Vancouver)

December, 2009

© Hassan Saadaoui 2009

Abstract

Beta-detected Nuclear Magnetic Resonance (β -NMR) uses highly spin polarized β -emitting nuclei as a probe. Besides its use in nuclear physics, it has also become a powerful and sensitive tool in condensed matter physics and materials science. At TRIUMF, β -NMR of $^8\text{Li}^+$ has been developed to study materials in a depth-resolved manner, where the implantation depth of $^8\text{Li}^+$ is controlled via electrostatic deceleration. In this thesis, β -NMR of $^8\text{Li}^+$ has been used to study high- T_c cuprate superconductors (HTSC). The objective of this work is to search for spontaneous magnetic fields generated by a possible time-reversal symmetry breaking (TRSB) superconducting state near the surface of hole-doped $\text{YBa}_2\text{Cu}_3\text{O}_{7-\delta}$ (YBCO), and study the nature of the vortex lattice (VL) in YBCO and electron-doped $\text{Pr}_{2-x}\text{Ce}_x\text{CuO}_{4-\delta}$ (PCCO). For several advantages, our measurements were carried out by implanting $^8\text{Li}^+$ in thin silver films evaporated on the superconductors.

In our TRSB studies, the magnetic field distribution $p(B)$ is measured 8 nm away from the Ag/YBCO interface in magnetic fields $B_0 = 5$ to 100 G, applied parallel to the interface. $p(B)$ showed significant broadening below the T_c of ab- and c-axis oriented YBCO films. The broadening signals the existence of weak disordered magnetic fields near the surface of YBCO. From the broadening's temperature and field dependence we draw an upper limit of 0.2 G on the magnitude of spontaneous magnetic fields associated with TRSB.

To study the VL, $p(B)$ is measured at average implantation depths ranging from 20 to 90 nm away from the Ag/YBCO or Ag/PCCO interface in $B_0 = 0.1$ to 33 kG, applied perpendicular to the surface. $p(B)$ showed a dramatic broadening below T_c as expected from the emerging field lines of the VL in the superconductor. In YBCO, $p(B)$ is symmetric and the de-

Abstract

pendence on B_0 is much weaker than expected from an ideal VL, indicating that the vortex density varies across the face of the sample on a long length scale, likely due to vortex pinning at twin boundaries. In PCCO, a 2D VL is established due to the high anisotropy of the superconductor leading to a nearly symmetric $p(B)$.

Table of Contents

Abstract	ii
Table of Contents	iv
List of Tables	v
List of Figures	vi
Acknowledgments	vii
Statement of Co-Authorship	ix
1 Introduction	1
1.1 The β -NMR Technique	4
1.1.1 Production of Spin-Polarized $^8\text{Li}^+$	5
1.1.2 The High-Field Spectrometer	8
1.1.3 The Low-Field Spectrometer	9
1.1.4 Implantation Profiles	11
1.1.5 β -NMR Resonance Spectra	12
1.1.6 Comparison of β -NMR with NMR and μSR	14
1.2 Generic Properties of HTSC	17
1.2.1 Crystal Structure	17
1.2.2 Electronic Configuration	19
1.2.3 Doping Phase Diagram	20
1.3 Theoretical Foundations	21
1.3.1 London Theory	22
1.3.2 Ginzburg-Landau Theory	24

Table of Contents

1.3.3	BCS Theory	26
1.4	Time-Reversal Symmetry Breaking in HTSC	28
1.4.1	Which Order Parameters Break TRS?	28
1.4.2	Theories	31
1.4.3	Experiments	35
1.5	Vortex Lattice in HTSC	40
1.5.1	Regular VL Characteristics	40
1.5.2	Disorder	47
1.5.3	Anisotropy and Thermal Fluctuations	49
1.5.4	Temperature Dependence of λ	53
1.5.5	Proximal Detection of the VL	54
1.6	Thesis Outline	55
	Bibliography	57
2	Search for Broken Time-Reversal Symmetry Near the Surface of (110) and (001) $\text{YBa}_2\text{Cu}_3\text{O}_{7-\delta}$ Films	66
2.1	Introduction	66
2.2	Experimental Details	69
2.3	Results	72
2.4	Discussion and Conclusions	75
	Bibliography	78
3	Vortex Lattice Disorder in $\text{YBa}_2\text{Cu}_3\text{O}_{7-\delta}$ Probed Using β-NMR	82
3.1	Introduction	82
3.2	The Magnetic Field Distribution $p(B)$ in the Vortex State	84
3.3	Experimental Details	92
3.4	Results	95
3.5	Discussion and Conclusions	102
	Bibliography	105

Table of Contents

4 Vortex Lattice Near the Surface of $\text{Pr}_{1.85}\text{Ce}_{0.15}\text{CuO}_{4-\delta}$	111
4.1 Introduction	111
4.2 Experimental Details	112
4.3 Results and Discussion	113
Bibliography	119
5 Summary and Conclusions	122
Bibliography	127
 Appendices	
A RF Modes	129
A.1 CW RF Mode	129
A.2 Pulsed RF Mode	130
B β-NMR Resonance in Ag	133
B.1 Field and Temperature Dependence	133
B.2 Effect of the Dewetting Transition in Ag	134
C Obtaining Zero-Field	140
D Spin-Lattice Relaxation	143
D.1 Spin-Relaxation Signal	143
D.2 Ag	145
D.3 Ag/YBCO	150
D.4 PCCO	152
E Sample Characteristics	154

List of Tables

1.1	Example of isotopes suitable for β -NMR compared to μ^+ . Intrinsic characteristics of nuclei are given by nuclear spin, I , half life $T_{1/2}$, gyromagnetic ratio γ , and asymmetry. Production of rate μ^+ used in Low-energy μ SR, and of isotopes produced at TRIUMF and world-wide labs are given.	5
1.2	Summary of the characteristics of high and low-field spectrometers. Both spectrometers have an ultra high vacuum (UHV) cryostat with a temperature range ~ 3 -300 K, and are mounted on high voltage platforms allowing the variation of $^8\text{Li}^+$ energy.	8
1.3	Electron configurations of common atoms in cuprate HTSC. .	19
E.1	Characteristics of the samples used in thesis thesis. TW: twinned crystal, DTW: detwinned crystal. d is the nominal thickness of the films, d_{Ag} the thickness of deposited Ag if applicable, and R_a the RMS surface roughness of the samples after Ag was deposited found measured by AFM.	156

List of Figures

1.1	A simplified mean-field magnetic field-temperature phase diagram of a type II superconductor. The superconductor expels the applied field from the bulk below B_{c1} , and is in the vortex state for fields up to B_{c2}	2
1.2	(a) Layout of the polarizer and β -NMR spectrometers. (b) Polarization of ${}^8\text{Li}^+$ using optical pumping. (c) Sodium cell scan shows the dependence of the asymmetry on Na cell bias.	6
1.3	Experimental setup used to measure the spin polarization of ${}^8\text{Li}^+$ in (a) the high-field, and (b) the low-field β -NMR spectrometers.	9
1.4	TRIM simulation of the stopping distribution of 20000 ions of ${}^8\text{Li}^+$ implanted in a 1000 nm Ag layer. The energy of ${}^8\text{Li}^+$ is varied from 1 keV to 28 keV leading to mean depths from 5 nm to 104 nm. A significant fraction of ${}^8\text{Li}^+$ is back scattered by the Ag surface.	10
1.5	(a) Angular distribution, $W(\theta)$, of the electrons emitted after the ${}^8\text{Li}^+$ β -decay: when all energies are sampled with equal probability, the asymmetry parameter has the value $a = -1/3$. (b) Energy distribution of the emitted electrons after the ${}^8\text{Li}^+$ decays.	12

List of Figures

1.6	(a) Asymmetry of the betas emitted after implanting a 28 keV $^8\text{Li}^+$ beam into a 120 nm Ag film. Both helicities are shown. (b) The difference of the asymmetries of the two helicities is plotted. The solid line is a fit to a Lorentzian, and the dashed line refers to the Larmor frequency. The spectra are taken in $B_0 = 152.6$ G, and $T = 100$ K.	15
1.7	Typical crystal structure of $\text{YBa}_2\text{Cu}_3\text{O}_7$ (left) and $\text{Pr}_{2-x}\text{Ce}_x\text{CuO}_4$ (right).	18
1.8	The typical doping phase diagrams of hole (right) and electron-doped (left) high- T_c cuprates are shown. The various phases are explained in the text.	20
1.9	Idealized spatial variation of the magnetic field B and order parameter ψ for $\kappa \ll 1$ (type I) and $\kappa \gg 1$ (type II) superconductors.	25
1.10	Normalized amplitude and phase of the main candidate order parameters in HTSC are shown. The order parameter is written as $\Delta = \Delta e^{i\phi} = \Delta g(\theta)$. Here θ is a polar angle in momentum space $\mathbf{k} = k(\cos \theta, \sin \theta)$; $g(\theta) = \cos(2\theta + \alpha)$, where $\theta = 0$ for s -wave and finite for d - and d_{xy} -wave; $\alpha = 0$ ($\pi/2$) for s -wave and d -wave (d_{xy} -wave).	30
1.11	Left: the μSR relaxation rate in Sr_2RuO_4 showing the appearance of spontaneous magnetic fields below T_c [3]. Right: absence of spontaneous magnetic fields in YBCO ($T_c=90$ K) and BSCCO ($T_c=85$ K) systems [65]. In μSR , the relaxation rate is a measure of the spread of the internal fields.	36
1.12	Top: conductance in YBCO/Cu tunnel junction showing splitting of the ZBCP as a function of external field [56]. Bottom: absence of the splitting of the ZBCP in the normalized conductance spectra taken on the (110) surface of YBCO with a Pt-Ir tip at 4.2 K for an STM tunnel junction (main panel) and for a point contact (left inset). Right inset shows the expected curves from $d+s$ and $d+is$ symmetries. [54].	37

List of Figures

1.13 (a) Spontaneous magnetic field generated by a thin YBCO film plotted versus temperature, as measured by Carmi <i>et al.</i> [78]. (b) Scanning SQUID microscope image of an area with a 45° asymmetric <i>c</i> -axis YBCO bicrystal grain boundary of 180 nm thickness. The flux through the grain boundary is shown [79]. (c) Scanning SQUID images of (100)/(103) YBCO cooled in 3mG. The corresponding flux distribution is shown. A broader field distribution is observed in (001), although it has the same average flux as in (103) [80].	39
1.14 (a) Simulated field distribution using Eq. (1.45) at depths $z = 2000$ nm and $z = -10$ nm, and $B_0 = 1$ T. Parameters relevant to YBCO at $T \ll T_c$ have been used: $\lambda_{ab} = 150$ nm, $\xi = 2$ nm. A Gaussian cutoff is used where $b = 0$. Solid (dotted) lines are lineshapes of triangular (square) lattice. Top inset shows the positions of the low-field cutoff (A), most probable field (B) and high-field cutoff (C) in a triangular lattice. Bottom inset: field distribution measured in a YBCO crystal by μ SR at 0.5 T fitted by the London model convoluted with a Gaussian distribution [88].	43
1.15 Variance of the field distribution as a function of depth, with $z > 0$ ($z < 0$) corresponding to inside (outside) the superconductor. The parameters $\lambda_{ab} = 150$ nm, $\xi = 2$ nm, and a Gaussian cutoff ($b = 0$) have been used.	45
1.16 Variance of the field distribution inside the superconductor at $z = 50$ nm for (a) and (c), and outside at $z = -50$ nm for (b) and (d). Parameters relevant to YBCO (PCCO) have been used where $\lambda_{ab} = 150$ (300) nm and $\xi = 2$ (6) nm. Also, plotted is the variance for $\xi = 0, 20$ nm. A Gaussian cutoff is used in all, where $b = 0$ is taken for YBCO, and $b = B/B_{c2}$ ($B_{c2}=9$ T) is used for PCCO.	46

List of Figures

1.17	Top panel: the vortex configuration in YBCO crystals obtained using Bitter decoration technique [93]: images of (a) a twinned and (b) a twin-free area are taken after cooling in 20 G. The marker is 10 μm . Bottom panel: STM images of twinned YBCO single crystals at 4 K, with the magnetic field applied parallel to the c -axis, and perpendicular to the surface [94]. (c) Image taken after field cooling in 3 T. (d) Topographic images of the YBCO surface showing the twin boundary.	48
1.18	The field distribution in BSSCO crystals measured by μSR in an external field of 1.5049 T applied along the c -axis. The measured lineshape is not well fitted by a 3D model (dashed line), and well fitted by a 2D model [13].	51
1.19	(a) The μSR field distribution measured in low and high applied fields. The low field lineshape is that of a regular VL, but the high field is due to a melted lattice. (b) The skewness parameter $\alpha = \langle \Delta B^3 \rangle^{1/3} / \langle \Delta B^2 \rangle^{1/2}$ of the field distribution is shown [101].	52
1.20	(a) T -dependence of the second moment $\sigma \propto 1/\lambda^2$ in a sintered YBCO sample measured in a field of 350 mT. The data is well fitted by the two-fluid model suggesting an s -wave pairing symmetry [104]. (b) T -dependence of $1/\lambda^2$ in a high quality YBCO single crystal in 5 kG external field. The data is well fitted by the d -wave order parameter, and strongly deviates from s -wave [105].	53
2.1	Geometry of the experiment where the field is applied along the surface. The orientation of the YBCO films is shown: Ag/YBCO(110) on the right and Ag/YBCO(001) on the left.	68

List of Figures

2.2	Typical β -NMR spectra in Ag taken above and below T_c at 2 keV, about 8 nm from the (110)-oriented YBCO interface, in an external field of $B_0 = 10$ G (FC) applied along the surface of the film. Solid lines are fits to a Lorentzian of amplitude A , HWHM Δ and resonance frequency ω_L , i.e. $\mathcal{L}(\omega) = \frac{A}{4(\omega-\omega_L)^2+\Delta^2}$. Inset: simulated implantation profile for the $^8\text{Li}^+$ in a 15nm Ag layer on YBCO from TRIM.SP [28]. The $^8\text{Li}^+$ stops at an average depth of 8 nm away from the Ag/YBCO interface.	70
2.3	The T -dependence of the Lorentzian HWHM of the $^8\text{Li}^+$ resonance at 2 keV, i.e. 8 nm from the Ag/YBCO(110), Ag/YBCO(001), and Ag/STO (open circles) interface. The data on the Ag/YBCO(110) and Ag film was taken while cooling in $B_0 = 10$ G. The data on Ag/YBCO(001) was collected in $B_0 = 10$ after ZFC to 5 K. The widths were independent of field-cooling conditions. The dashed lines represent the average Ag width, the arrows point to the T_c of the YBCO films, and the solid lines are guide to the eye.	73
2.4	The 10 K linewidth (HWHM) of the NMR resonance versus the applied field B_0 taken in Ag on (110)- and (001)-oriented YBCO films. The data were taken after ZFC and gradually increasing the field, except in the (110) films which was FC. The solid lines are fits to the linewidth in the Ag on YBCO(001) at 10 and 100 K.	74
2.5	Extra broadening, $\Delta(10\text{ K}) - \Delta(100\text{ K})$, versus the average depth of $^8\text{Li}^+$ into a 50nm thick Ag on (001) YBCO film, ZFC in 10 G and 100 G.	75

List of Figures

3.1	(a) Simulation of $p(B)$ in an applied field of 52 mT at a distance 90 nm from the superconductor using Eq. (3.5) convoluted with a Lorentzian of width Δ_D . (b) The broadening of $p(B)$ versus the applied field. Solid lines represent σ from Eq. (3.6) in the bulk, and 40 and 90 nm away from the superconductor. Long dashed line shows σ at 90 nm from Eq. (3.9) for $D = 4 \mu\text{m}$ and $f = 0.1$. Inset: sketch of a possible vortex arrangement including vortex trapping at twin boundaries spaced by D and a regular triangular vortex lattice elsewhere. In all figures $\lambda(0) = 150 \text{ nm}$	87
3.2	$\sigma(T)$ (normalized at $T = 0$), from Eq. (3.9) for $B_0 = 52 \text{ mT}$, $z = -90 \text{ nm}$, and $f = 0.1$, is plotted against T/T_c for different values of D . A d -wave temperature dependence of $\lambda(T)$ is used [37], where $\lambda(0) = 150 \text{ nm}$	88
3.3	Implantation profiles of $^8\text{Li}^+$ at energies of (a) 5 keV into 60 nm of Ag with the mean at 40 nm away from YBCO film, and (b) 8 keV into 120 nm of Ag with the mean at 90 nm away from YBCO crystals, as calculated via TRIM.SP (Ref. [45]). Solid lines are phenomenological fits.	93
3.4	βNMR resonances in Ag/YBCO (crystal I) at temperatures 100 K, 80 K, 20 K, and 4.5 K measured in a magnetic field B_0 of 52.3 mT applied along YBCO c -axis. The solid lines are best fits using a Lorentzian.	96
3.5	The vortex-related broadening below T_c , $\Delta_{\text{sc}}(T) = \Delta(T) - \Delta_{\text{ns}}$ of the twinned (full symbols) and detwinned (opaque squares) YBCO crystals in an applied field B_0 . $\Delta(T)$ is the linewidth at temperature T of the Lorentzian fits and Δ_{ns} is the constant linewidth in the normal state. Solid lines represent a fit using $\Delta_{\text{DVL}} = 2.355\sigma$ where σ is given in Eq. (3.9) and D and f are varied to fit the data. A d -wave temperature dependence of $\lambda(T)$ in YBCO is used, (Ref. [37]) where $\lambda(0) = 150 \text{ nm}$	98

List of Figures

3.6	Comparison of the field distributions in the three samples taken at temperatures 100 K (top panel), 5 K (crystals) and 10 K (film). The x -axis is shifted by B_0 , the applied field which is 52.3 (51.7) mT for the crystals (film). Solid lines are Lorentzian fits and dashed lines are simulation described in the text.	99
3.7	Superconducting broadening $\Delta_{sc}(T)$ of β -NMR resonance spectra at temperatures ~ 4.5 -10 K in the three samples. The experimental broadening is compared with the linewidth of an ideal VL Δ_{VL} (dashed lines), and Δ_{DVL} of a disordered VL (solid lines), which are both weighted by the ${}^8\text{Li}^+$ profile given in Fig. 3.3.	101
4.1	TRIM simulation of ${}^8\text{Li}^+$ stopping profile into 40 nm of Ag on 300 nm of PCCO, at energies of 5 keV and 28 keV.	112
4.2	Spin relaxation spectra in Ag/PCCO at 5 K, taken in an applied static magnetic field $B_{app} = 200$ G, and ${}^8\text{Li}^+$ energies of 5 and 28 keV. The solid line is a fit using a phenomenological biexponential function for beam on (0 to 4 s) and beam off (4 s to 8 s) [8].	114
4.3	The β NMR asymmetry spectra of ${}^8\text{Li}^+$ implanted at 5 keV in the Ag/PCCO at different temperatures. The dashed line shows the Larmor frequency in the applied magnetic field of $B_{app} = 216$ G. The solid lines are Lorentzian fits.	116
4.4	(a) The resonance frequency, B_{res} , versus T in an applied field $B_{app} = 216.62$ G (dashed line), fitted by $B_{app} + 0.8(1 - (T/22)^4)^2$ (solid line). (b) The linewidth (FWHM) versus T . The solid line represents $\text{FWHM}_{NS} + 4.2(1 - (T/22)^{2.2})^2$, where $\text{FWHM}_{NS} = 0.74$ G is the normal state broadening (dashed line). All data are extracted from Lorentzian fits of the resonances.	117

List of Figures

A.1	(a) Pulsed RF sequence where RF is on during a time interval $t_p = 80$ ms. The excited frequencies have a bandwidth $\Delta\omega = 200$ Hz. The functional form is ln-sech, and the pulse sequence controls when the RF is delivered. (b) The spectra in Ag(15 nm)/YBCO at $E = 2$ keV, $T = 10$ K, and $B_0 = 100$ G taken using CW and pulsed RF modes with similar power (B_1) are shown. The width is broadened by a factor of two using CW RF. The width of the resonance taken with the pulsed RF is 348 Hz, which is close to the ideal intrinsic dipolar broadening in Ag of 250 Hz.	131
B.1	The temperature dependence the Larmor frequency, FWHM, amplitude and baseline of Lorentzian fits of β -NMR resonances in an 15 nm film thick Ag evaporated on SrTiO ₃ . The data is taken with a 2 keV $^8\text{Li}^+$ beam in an external field $B_0 = 10$ G, applied parallel to the surface of the substrate.	135
B.2	(a) β -NMR resonances in Ag(120 nm) on YBCO twinned crystal at $B_0 = 3.33$ T and $E = 8$ keV. Solid lines are fits to one (two) Lorentzian(s) at 100 (85) K. (b) The shift and amplitude of the S and O peaks are plotted against temperature at 3 T. Copied from G. D. Morris <i>et al.</i> , Phys. Rev. Lett. 93 , 157601 (2004).	136
B.3	The β -NMR spectra in Ag(15 nm)/STO at room temperature where $B_0 = 10$ G, and $E_{\text{Li}} = 2$ keV. The linewidth increases from 314 Hz, when measured in December 2007, to 504 Hz in August 2008.	137
B.4	AFM of silver films showing an increase in the surface roughness with time. (a) AFM is done immediately after evaporating 15 nm of Ag onto an STO substrate. (a) AFM done 8 months after 15 nm of Ag was evaporated onto an STO substrate (this sample is different from the one used in (a)).	138

List of Figures

B.5	Auger depth profile of (a) fresh Ag(15 nm)/STO, and (b) few weeks old sample. Ion bombardment time is given in seconds. The sample was sputtered by Ar, removing layers at a rate of ≈ 0.1 nm/s. Carbon, oxygen, and Sulfur atoms have been identified in the first top layers.	139
C.1	Variation of the Larmor frequency, ω_L , with the currents I_x , I_y , I_z which run into three Helmholtz coils and create fields along x , y , and z direction, respectively.	141
D.1	Spin relaxation spectra recorded in $B_0 = 150$ G. The asymmetry recorded with a Laser of positive (A^+) and negative (A^-) helicity are shown. The overall asymmetry $a = A^+ - A^-$ is also plotted. Solid lines are fits explained in the text.	144
D.2	(a) T -dependence of the spin relaxation in $25 \mu\text{m}$ silver foil at $B_0 = 150$ G. The 28 keV $^8\text{Li}^+$ beam is implanted into the sample in 4 s pulses every 20 s. Solid lines are fits using Eq. (D.5) with two components. (b) $\lambda = 1/T_1$ (slow component) extracted from (a) compared with the baseline of the resonance in an Ag film (50 nm) taken at 3 T.	147
D.3	The B_0 and T -dependence of the amplitude, A , and relaxation rate, $1/T_1$, of $^8\text{Li}^+$ polarization implanted at full energy into a silver foil. The data was extracted by fitting the asymmetry to a pulsed exponential function. A and $1/T_1$ of the slow relaxing part of the function is shown here. The solid lines are fits using a Lorentzian form described in the text.	149
D.4	Spin relaxation of $^8\text{Li}^+$ of energy (a) 13 keV and (b) 28 keV implanted into Ag(50 nm)/YBCO(600 nm) at 100 G applied field under zero field conditions. Solid lines are single exponential fit to the beam off asymmetry. (c) Spin-relaxation spectra versus energy at 10 K.	151

List of Figures

D.5	Temperature dependence of $1/T_1$ in Ag(50 nm)/YBCO(600 nm), at two different energy extracted from Fig. D.4. Also, shown is $1/T_1$ in a Ag foil extracted using single exponential fit to the beam off asymmetry. Inset: energy dependence of $1/T_1$ in Ag/YBCO at 10 K.	152
D.6	The Spin relaxation of $^8\text{Li}^+$ at full energy implanted into a 300 nm thick PCCO film, in $B_0 = 150$ G.	153

Acknowledgments

First and foremost I would like to thank my co-supervisors Rob Kiefl and Andrew MacFarlane for their support and advice throughout the course of my PhD. Their enthusiasm combined with patience and accessibility are what made this work possible. I am very grateful for their responses to my inquiries and availability during my entire stay at UBC. I would also like to thank my committee members: D. A. Bonn, M. Franz, and J. H. Brewer for their comments, and for reading the thesis.

This thesis has benefited a lot from the help and expertise of Gerald Morris who was always willing to help and go an “extra mile”. Gerald’s great passion for what he does makes him a brilliant collaborator. I would also like to thank Zaher Salman who taught me the first lessons of how to use β -NMR and analyze the data. Zaher’s involvement and encouragements never stopped even after he moved to another laboratory.

I wish also to thank my colleagues in β -NMR group. Special thanks to Susan Q. Song for helping with the characterization of samples at AMPEL and Masrur Hossein for helping with computer-related issues. My colleagues Terry Parolin, Dong Wang, Micheal Smadella, Masrur Hossein, Susan Q. Song, and others have spent many nights taking the actual data; for that and for the helpful discussions and good times we had together, I am very grateful.

The data in this project was taken over many years and a lot of people, other than the ones that have been already mentioned above, have helped to take shifts, tune the spectrometers,...etc. I would like to mention R. Abasalti, D. Arseneau, K. H. Chow, S. Dunsiger, B. Hitti, I. Fan, T. Keeler, C. D. P. Levy, A. I. Mansour, R. Miller, M. R. Pearson, and D. Vyas. Many thanks to AMPEL staff for showing me how to use the characterization

Acknowledgments

tools. I would especially like to thank Ruixing Liang, Pender Dosanjh, Micheal Whitwick, and Mustafa Masnadi.

My friends at UBC have always been a source of encouragement. To all, I say thank you very much for your support and encouragement, and for making my stay in Vancouver so enjoyable and memorable. The support of my family has been and is still exceptional, and I would not have gotten here without that; I don't have the words to thank them enough.

Statement of Co-Authorship

Chapters 2, 3, and 4 of this thesis have been written as journal papers by myself as the first author. The co-authors have been partly involved in taking the data and tuning the β -NMR spectrometers and optical polarizer, reviewing and commenting on the manuscripts, or supplying the studied samples. The design of research methods, literature review, data analysis, and manuscript preparation were all done by myself in consultation with my supervisors: Drs. R. F. Kiefl and W. A. MacFarlane. The pulsed RF technique employed in chapter 2 was a collaborative effort of S. R. Kreitzman, R. F. Kiefl, Z. Salman, R. I. Miller, W. A. MacFarlane, myself, and others.

Chapter 1

Introduction

Following the discovery of zero resistance in mercury below 4.19 K by H. Kammerlingh Onnes in 1911, the *superconducting* materials showed another striking phenomenon by expelling the magnetic field from the bulk as seen by Meissner and Ochsenfeld in 1933. Because of the negligible power dissipation, Onnes predicted the use of superconductors for high-field electromagnets which was realized in the 1960s. These magnets, among other uses, are pivotal for magnetic resonance imaging. Today, there are many applications of superconductivity. The study of this exotic state has not only led to new applications, but was also a driving force for new experimental techniques and theoretical methods for studying systems with strong electron-electron interactions, generating significant concepts in physics and related fields.

After the discovery of superconductivity, it took almost 50 years until it was understood microscopically, when in 1957 Bardeen, Cooper and Schrieffer published their BCS theory. This theory, however, predicted that superconductivity can only be realized below low critical temperatures $T_c \sim 23$ K. In 1986, Bednorz and Müller discovered a new material $\text{La}_{2-x}\text{Ba}_x\text{CuO}_{4-\delta}$ that superconducts at $T_c = 35$ K. A year later they were awarded the Nobel Prize in physics. Within a few months, new materials were made to superconduct at temperatures as high as 93 K in $\text{YBa}_2\text{Cu}_3\text{O}_{7-\delta}$. Because of their high T_c s, these materials are called high- T_c superconductors (HTSC).

Up to the present, the mechanism behind HTSC remains a major focus of condensed matter research. The unique properties of HTSC has challenged and keeps challenging, not only well-established theories, but also experimental detection techniques. HTSC are type II superconductors where an external magnetic field, above a lower critical field B_{c1} , penetrates in the superconductor in quantized vortices each carrying a flux quantum

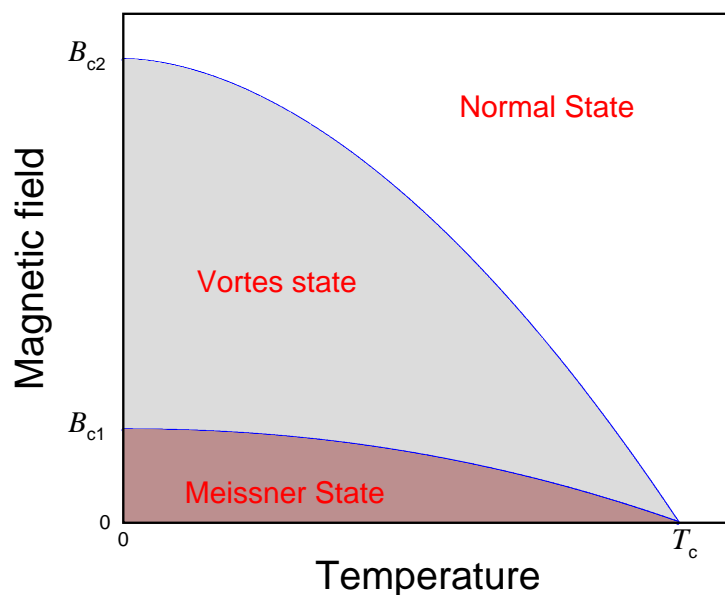


Figure 1.1: A simplified mean-field magnetic field-temperature phase diagram of a type II superconductor. The superconductor expels the applied field from the bulk below B_{c1} , and is in the vortex state for fields up to B_{c2} .

$\Phi_0 = \frac{h}{2e} = 2.067 \times 10^7$ G nm. These vortices form cylindrical normal state regions surrounded by superconducting regions, a state known as the mixed or vortex state. In contrast, in type I superconductors, an applied magnetic field above B_{c1} penetrates uniformly and bulk superconductivity disappears. The field-temperature phase diagram of type II superconductors is shown in Fig. 1.1.

Investigations of the magnetic properties of HTSCs have been central to uncover the existence of striking new phenomena. In the Meissner state, although the flux expulsion suggests that the bulk material is free of magnetic fields, some magnetic order may develop near the surface, grain boundaries, or impurities where the magnetic shielding is not perfect. As a result, a spontaneous magnetic field may appear, indicating a *broken time-reversal symmetry* state analogous to ferromagnetism [1]. Such a state has been observed in several superconductors such as heavy Fermion su-

perconductors $U_{1-x}Th_xBe_{13}$ [2], and Ru-based superconductors Sr_2RuO_4 [3], and $PrOs_4RuSb_{12}$ [4]. The most direct evidence of spontaneous fields in these superconductors was provided by conventional muon-spin rotation (μ SR), which is a bulk probe. In HTSC the effect is thought to be more pronounced near the surface of materials such as $YBa_2Cu_3O_{7-\delta}$ and the associated magnetic fields may be local and small in magnitude. Several experimental investigations have been done reaching different conclusions, where the effect is apparent in some and absent in others. Therefore, the need is clear for a sensitive magnetic probe to detect such magnetic fields near the surface.

In the vortex state, the vortices often form a regular lattice of flux lines of triangular symmetry. This leads to a periodic variation of the magnetic field in space, which is maximum at the core, and decays exponentially over a length scale called the magnetic penetration depth λ . The latter is a fundamental length scale of superconductivity because $1/\lambda^2$ is proportional to the modulus of the superconducting order parameter, and its temperature dependence is determined by the pairing symmetry of the superconducting wave-function. Impurities, grain and twin boundaries, and anisotropy affect the vortex lattice, leading to a disordered lattice and modifying the magnetic field variation from that of a regular lattice. This makes the accurate extraction of the penetration depth difficult, as disorder may strongly modify the spatial variation of the magnetic field. Thus, it is important to understand the effect of disorder on the vortex lattice.

In this thesis, I have used β -detected nuclear magnetic resonance (β -NMR) as a local probe to detect any spontaneous magnetic fields near the surface of $YBa_2Cu_3O_{7-\delta}$ HTSC superconductors in the Meissner state, and to study the features of the field distribution of $YBa_2Cu_3O_{7-\delta}$ and $Pr_{2-x}Ce_xCuO_{4-\delta}$ superconductors in the vortex state. The β -NMR technique is unique in its capability to measure directly the field distribution in a depth resolved manner, on a 2-500 nm length scale. In this chapter, I will introduce the reader to the topics presented in this thesis. In Section 1.1, the β -NMR technique will be described and compared to other techniques. In Section 1.2, some generic properties of HTSC materials will be briefly in-

troduced. In Section 1.3, some established theories of superconductivity will be discussed. In Section 1.4, the notion of time-reversal symmetry breaking and its manifestation in HTSC will be reviewed. In Section 1.5, the physics of the vortex lattice and its dependence on disorder will be discussed. In Section 1.6, an outline of the thesis will be given.

1.1 The β -NMR Technique

Like most other nuclear methods, β -NMR is a sensitive local technique offering a wealth of information gained via the radioactive decay of the probe nuclei. The technique has made great contributions to the understanding of nuclear structure of unstable nuclei [5, 6]. It has also become a powerful and sensitive tool in condensed matter physics and materials science for investigating micro-structures, local magnetism, Knight shifts, spin relaxation, impurities and defects [7]. The technique is similar to NMR, but more sensitive; NMR needs in general $\approx 10^{18}$ probe nuclei, while β -NMR requires only 10^7 probe nuclei. The high sensitivity of β -NMR is due primarily to the method of detecting the spin polarization through the properties of the radioactive decay of highly spin polarized short-lived nuclei. Once implanted into the material, and during their lifetime, the probe nuclei are interacting with internal and external magnetic fields within the sample. All these interactions can affect the spin polarization of the probe nuclei, which emit β -particles with an anisotropic angular distribution that is correlated with the nuclear spin direction. The polarization can be destroyed by applying an RF field with a frequency matching the spin resonance condition, leading to isotropic emission of β electrons. By placing two detectors facing each other with the sample in between, one can measure the asymmetry of the emitted β electrons, therefore determining the polarization of the probe at the moment of its decay, which is a function of the local environment. In the following I will describe the technique in more details.

1.1. The β -NMR Technique

Isotope	I	$T_{1/2}$ (s)	γ (MHz/T)	Asymmetry	Production rate (ions/s)
μ^+	1/2	2.2×10^{-6}	135.5	0.33	10^4
^8Li	2	0.84	6.013	0.33	10^8
^{11}Be	1/2	13.8	22	~ 0.2	10^7
^{15}O	1/2	122	10.8	0.7	10^8

Table 1.1: Example of isotopes suitable for β -NMR compared to μ^+ . Intrinsic characteristics of nuclei are given by nuclear spin, I , half life $T_{1/2}$, gyromagnetic ratio γ , and asymmetry. Production of rate μ^+ used in Low-energy μSR , and of isotopes produced at TRIUMF and world-wide labs are given.

1.1.1 Production of Spin-Polarized $^8\text{Li}^+$

A 500 MeV proton beam is produced at the 9 m radius TRIUMF cyclotron, and is used as a driver for the Isotope Separator and Accelerator (ISAC) facility. At ISAC, the high intensity proton beam strikes a special production target, such as tantalum or SiC, which is heated to 2000 °C and is sitting on a high-voltage (HV) platform. The radioactive ions created by nuclear reactions diffuse out of the target with thermal energies and are accelerated as they leave the HV platform. A high resolution mass separator is used to select the isotope of interest. In β -NMR, any β emitting isotope is in principle usable, provided it meets some basic requirements such as: (i) high production rate and facile ionization, (ii) ability to have polarized nuclear spins, and (iii) high β -decay asymmetry and small nuclear spin for simple spectra [8]. $^8\text{Li}^+$ meets many of these requirements (see Table 1.1) and is easily produced at ISAC with high intensity (10^8 ions/s). The ions are then accelerated to 28 keV (± 1 eV) in a low energy beam transport (LEBT) line and delivered to the polarizer.

A schematic view of the polarizer and low and high-field β -NMR stations is given in Fig. 1.2-(a). a high nuclear spin polarization of $^8\text{Li}^+$ is achieved by optical pumping with circularly polarized light from a single frequency ring dye laser (300 mW CW power). The first step in the procedure is to neutralize the ion beam by passing it through a Na vapor cell. The neutral

1.1. The β -NMR Technique

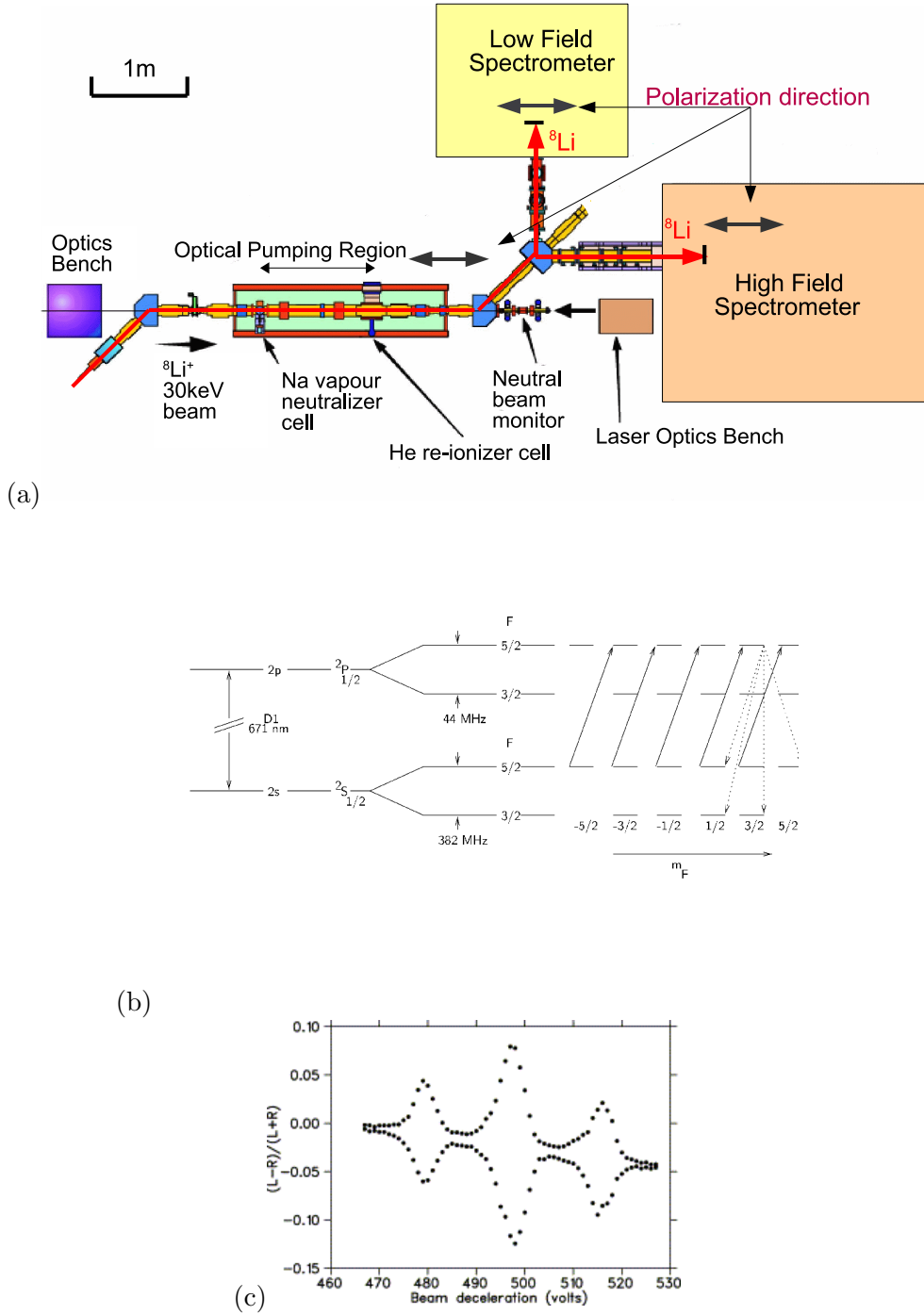


Figure 1.2: (a) Layout of the polarizer and β -NMR spectrometers. (b) Polarization of ${}^8\text{Li}^+$ using optical pumping. (c) Sodium cell scan shows the dependence of the asymmetry on Na cell bias.

1.1. The β -NMR Technique

beam then drifts 1.9 m in the optical pumping region in the presence of a small longitudinal magnetic field of 1 mT. The remaining charged fraction is removed electrostatically by two deflection plates and dumped onto a metallic cup known as Faraday cup.

The wavelength of the circularly polarized laser is tuned to 671 nm corresponding to the D1 atomic transition of neutral ${}^8\text{Li}$; $2s^2S_{1/2} \rightarrow 2p^2P_{1/2}$. The polarization scheme is shown in Fig. 1.2-(b). The ground and first excited atomic states are split by the hyperfine coupling between total ($s = 1/2$ electron+nucleus $I = 2$) spin states $F = 5/2$, and $3/2$. For circularly polarized light with positive helicity, only $M_F^i + 1 \rightarrow M_F^f$ ($\Delta M_F = 1$, M_F is the total atomic magnetic quantum number) transitions are allowed during excitation, whereas, the atom decays spontaneously with $\Delta M_F = 1, 0, -1$. The quantization axis is established by the helicity direction and maintained by a small magnetic field produced by coils co-axial with the beam line. After about 10-20 cycles of absorption and emission, a high degree of electronic and nuclear spin polarization is achieved. About 70 % of the spins are polarized in an atomic state $F = 5/2$, $M_F = 5/2$ for the positive helicity and $F = 5/2$, $M_F = -5/2$ for the negative helicity of the laser. The nuclear polarization $p \equiv (1/I) \sum_m p_m m$ (m is the nuclear magnetic quantum number $m = \pm 2, \pm 1, 0$ for $I = 2$, and p_m is the normalized occupation of sublevel m) is $p \sim 70$ % for spins in a state $m = 2$ for the positive helicity, or $m = -2$ for the negative helicity. The highest polarization is tuned by making small adjustment of the ion energy via the Na cell bias voltage (Fig. 1.2-c), which changes the Doppler shift and brings the atom into resonance with the laser light. Calibration using an unpolarized beam is easily carried out simply by blocking the laser.

By passing the neutral beam through a He gas cell, the valence electron is stripped. The charged polarized beam exits the polarizer, and is then passed through 45° electrostatic bending elements and delivered to the β -NMR low- or high-field spectrometers. The remaining neutral fraction goes undeflected into a neutral beam monitor placed outside the polarizer. To preserve the polarization only electrostatic elements are used in the beam line optics after the polarizer. The polarization of ${}^8\text{Li}^+$ is parallel to the

1.1. The β -NMR Technique

Station	Field and Polarization	Detector positions	Magnetic Field (T)	RF freq. (MHz)	Energy (keV)
High-field	\perp to surface	B, F	0.01 - 6.5	0.05 - 45	1 - 60
Low-field	\parallel to surface	L, R	0.0 - 0.02	DC - 0.2	1 - 28

Table 1.2: Summary of the characteristics of high and low-field spectrometers. Both spectrometers have an ultra high vacuum (UHV) cryostat with a temperature range ~ 3 -300 K, and are mounted on high voltage platforms allowing the variation of ${}^8\text{Li}^+$ energy.

momentum at the high-field spectrometer and perpendicular at the low-field station. The characteristics of both stations are summarized in Table 1.2, and discussed next.

1.1.2 The High-Field Spectrometer

A schematic of the detectors in the high-field spectrometer is shown in Fig. 1.3-(a), where the beam enters from the left, passing through a small hole in the back (B) detector, and lands in the sample to be studied. The beam spot on the sample depends primarily on focusing Einzel lenses, three adjustable collimating slits placed before the spectrometer, and on the applied magnetic field, and the beam energy at the spectrometer. Pictures taken with a charge coupled device (CCD) camera show a beam spot of 2-4 mm in diameter depending on the above conditions. As mentioned above, the polarization is along the beam axis, which is also parallel to a magnetic field $\mathbf{B}_0 = B_0\hat{z}$ ($100 \text{ G} < B_0 < 6.5 \text{ T}$) generated by a high homogeneity superconducting solenoid. A small Helmholtz coil is used to apply a transverse radio-frequency (RF) field $\mathbf{B}_1(t)$ ($B_{1,\text{max}} \sim 1 \text{ G}$) at frequency ω in the horizontal direction, perpendicular to both the beam and initial polarization. See Appendix A for more details about the type of RF field used in this thesis.

Two plastic scintillators are placed in front and behind the sample to detect the outgoing β electrons emitted after the ${}^8\text{Li}^+$ β -decay. The emitted electrons of an average energy 6 MeV can easily pass through thin stainless steel windows in the UHV chamber to reach the detectors. The B detector is located outside the bore of the magnet, since the emitted electrons, when

1.1. The β -NMR Technique

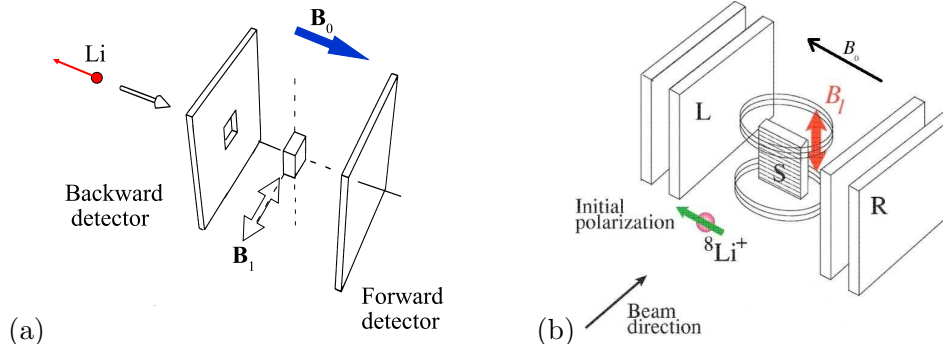


Figure 1.3: Experimental setup used to measure the spin polarization of ${}^8\text{Li}^+$ in (a) the high-field, and (b) the low-field β -NMR spectrometers.

inside, are confined to the magnet axis in high magnetic fields above about 1 Tesla. The focusing effect of the high magnetic field leads to similar detection efficiencies in both detectors although they have different solid angles as the forward detector is closer to the sample. The sample is mounted on a UHV cold finger cryostat. UHV is critical to avoid the buildup of residual gases on the surface of the sample at low temperature. The pressure in the main chamber can be reduced to 10^{-10} torr using differential pumping. Temperatures from 300 K to 3 K are obtained by cooling with cryogenic liquid He.

1.1.3 The Low-Field Spectrometer

This spectrometer is complementary to the high-field one, and allows for low field measurements (up to 220 G) in a transverse geometry. A schematic of the the low-field spectrometer is shown in Fig. 1.3-(b). A set of three orthogonal magnetic coils are wrapped around the sample chamber, where the main coil allows one to apply a static uniform magnetic field $\mathbf{B}_0 = B_0 \hat{y}$ with $0 < B_0 < 220$ G, applied parallel to the initial polarization direction and parallel to the surface of the sample. The other two coils are used to cancel the x, z components of residual magnetic fields (see Appendix C).

A small Helmholtz coil is used to apply an RF oscillating magnetic field $\mathbf{B}_1(t)$ ($B_{1,\text{max}} \sim 1$ G) at a frequency ω in the vertical direction, perpendicular

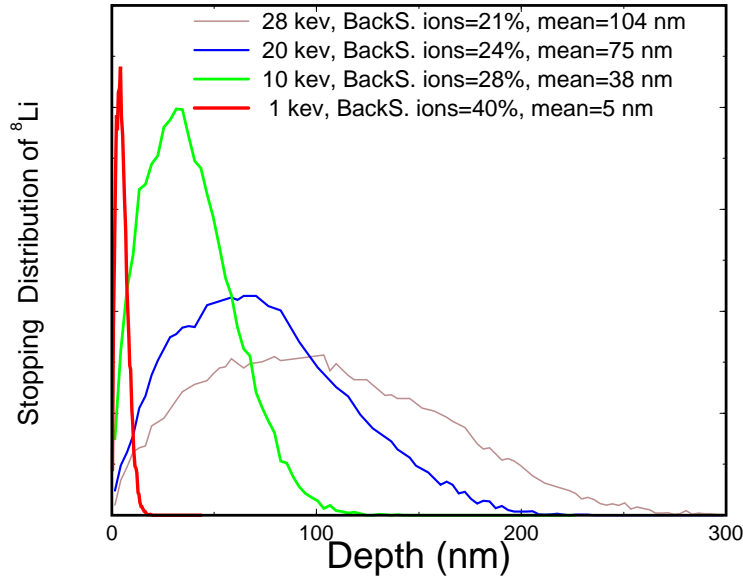


Figure 1.4: TRIM simulation of the stopping distribution of 20000 ions of ${}^8\text{Li}^+$ implanted in a 1000 nm Ag layer. The energy of ${}^8\text{Li}^+$ is varied from 1 keV to 28 keV leading to mean depths from 5 nm to 104 nm. A significant fraction of ${}^8\text{Li}^+$ is back scattered by the Ag surface.

to both the beam and initial polarization. The sample is sitting inside a UHV chamber at a pressure $\sim 10^{-10}$ torr. Four plastic scintillators measuring $10\text{ cm} \times 10\text{ cm} \times 0.3\text{ cm}$ are placed outside the UHV chamber: two coincidence detectors on the (R) right and two on the left (L) of the sample. The emitted β electrons can easily pass through thin stainless steel windows in the UHV chamber and reach the detectors. A CCD camera placed outside the UHV chamber is used to image the beam spot (2-4 mm in diameter) centered on the sample. The sample can be cooled from 300 K to 3 K. Currently, a cryostat is under design to allow cooling with ${}^3\text{He}$ to lower temperatures ($T < 1\text{ K}$), and to add an oven to reach higher temperatures above 300 K.

1.1.4 Implantation Profiles

The most important aspect of the high and low-field spectrometers at TRIUMF is the ability to decelerate the beam. Both spectrometers are mounted on separate HV platforms which are electrically isolated from ground. The implantation energy is controlled by adjusting the platform voltage bias. Using this setup, the energy of ${}^8\text{Li}^+$ can be varied from 28 keV down to 1 keV corresponding to implantation depths from 500 nm to 2 nm, allowing for depth-resolved surface and interface studies.

The profile of the implanted ions in materials can be simulated using the Stopping and Range of Ions in Matter (SRIM) or Transport of Ions in Solids (TRIM) codes introduced by Ziegler *et al.* [9, 10]. Both programs use Monte Carlo algorithms based on the binary collision approximation model for atomic collision processes in solids. The accuracy of both programs in calculating ion range distributions in various materials is well established, and they are routinely used in similar depth controlled experiments such as Low-Energy μSR [11]. By specifying the energy, charge, and mass of the probe ions, and the mass density and atomic numbers of the elements of the probed material, one is able to simulate the implantation profile using SRIM or TRIM, which both lead to comparable results. An example of stopping profiles of ${}^8\text{Li}^+$ in a thin Ag layer is given in Fig. 1.4, which shows the characteristic asymmetric and positively skewed distribution of ${}^8\text{Li}^+$ ions into Ag. The mean depth in Fig. 1.4 increases from as low as 5 nm to about 100 nm at full energy (28 keV). At low energy, a significant fraction of ${}^8\text{Li}^+$ is back scattered from the sample and deposited mainly on the thermal radiation shield surrounding the sample. This is mainly copper in the high-field spectrometer and aluminum in the low-field. The signal from ${}^8\text{Li}^+$ stopping outside the sample does not affect the resonance, since these ions do not see the RF field. This background signal, however, may slightly shift the baseline, *i.e.* the off-resonance asymmetry, which has no effect on the resonance features that are presented in this thesis.

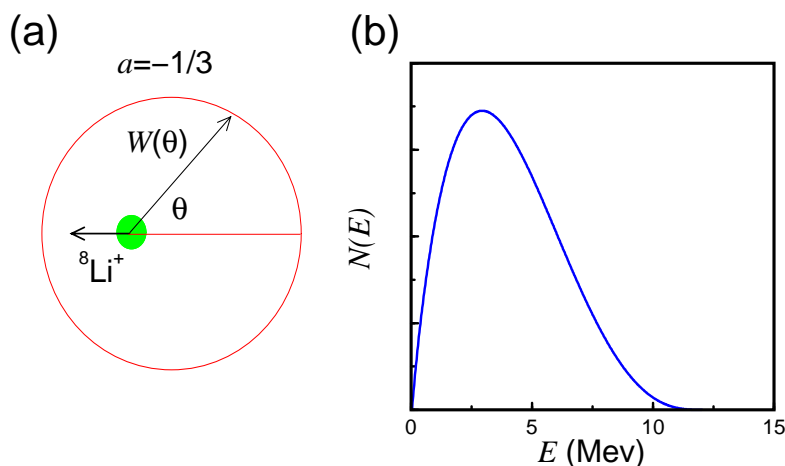


Figure 1.5: (a) Angular distribution, $W(\theta)$, of the electrons emitted after the ${}^8\text{Li}^+$ β -decay: when all energies are sampled with equal probability, the asymmetry parameter has the value $a = -1/3$. (b) Energy distribution of the emitted electrons after the ${}^8\text{Li}^+$ decays.

1.1.5 β -NMR Resonance Spectra

${}^8\text{Li}^+$ β -decays after a lifetime of $\tau = 1.209$ s according to



This decay occurs predominantly to an excited state in ${}^8_4\text{Be}$ at approximately 3 MeV rather than to the ground state [12]. The parity violation in weak interactions leads to an angular distribution W of the emitted electrons,

$$W(\theta) = 1 + ap\frac{v}{c}\cos\theta, \quad (1.2)$$

where v is the average velocity of the β electrons, c is the speed of light (in general $v \approx c$), $a = -\frac{1}{3}$ is the asymmetry factor of the beta-decay of ${}^8_3\text{Li}$, p is the nuclear polarization, and θ is the angle between the β -emission direction and spin polarization axis (Fig. 1.5-(a)). Thus, the β s are preferentially emitted along the direction of the arrow of $W(\theta)$ in Fig. 1.5-(a). The highest probability is for electrons emitted opposite to the spin polarization

1.1. The β -NMR Technique

of ${}^8\text{Li}^+$ nuclei at the moment of their decay. The β particles have an average energy of ~ 6 MeV, with an end-point energy of $E_{max} = 12.5$ MeV (Fig. 1.5-(b)). This energy is different from the Q -value of the β -decay because ${}^8_3\text{Li}$ decays, as mentioned above, mostly to an excited state in ${}^8_4\text{Be}$ [12].

The nuclear polarization has an initial value of p_0 and evolves in time due to interactions with the local environment. In two scintillators facing each other at 180° , the ratio, R , of the right detector counting rate N_R to that of the left detector N_L yields

$$R = \frac{N_R}{N_L} = \frac{\epsilon_R W(\theta = 0^\circ)}{\epsilon_L W(\theta = 180^\circ)} = \frac{\epsilon_R(1 + ap)}{\epsilon_L(1 - ap)}. \quad (1.3)$$

Here ϵ_R (ϵ_L) is the detection efficiency of the right (left) detector. If one assumes similar detection efficiencies and solid angles of both detectors ($\epsilon_R \approx \epsilon_L$), one easily finds

$$ap = \frac{N_R - N_L}{N_R + N_L} \equiv A(t). \quad (1.4)$$

This means that the final polarization, p , of ${}^8\text{Li}^+$ just before it decays can be deduced by measuring the asymmetry $A(t)$ of the β rates as a function of time.

In our experiment, we place the two detectors either at the left/right (low-field station) or at the back/front (high-field station) of the sample surface. The measured asymmetry is smaller than expected due to scattering of the electrons in the sample, background count rates, and the geometrical inequalities between the two detectors. To minimize these instrumental effects, we measure the asymmetry for the positive (A^+) and negative (A^-) helicities of the laser, *i.e.* ${}^8\text{Li}^+$ with nuclear spins polarized in a state of $m = 2$ or -2 . The final asymmetry is given by

$$a(t) = A^+(t) - A^-(t). \quad (1.5)$$

To measure the spin resonance we use a similar method to NMR. In NMR, a small degree of nuclear spin polarization of some atoms is achieved by a large static external magnetic field B_0 . By applying a continuous

1.1. The β -NMR Technique

wave (CW) RF field B_1 of frequency ω perpendicular to B_0 , one can induce a transition between the spin states when ω equals the Larmor frequency $\omega_L = \gamma B_0$,¹ where γ is the gyromagnetic ratio of the polarized nuclei, thus destroying the polarization. A pickup coil is used to detect the induced voltage from the ensemble's nuclear spin polarization. In β -NMR, one applies the same principle, except one measures the NMR signal using the asymmetry of the emitted electrons rather than a pick-up coil. One records the β -decay asymmetry as a function of the RF frequency, while the continuous beam of polarized ^8Li is implanted into the sample. Two modes of RF have been used in this thesis: a CW mode, and a pulsed mode. More details about these modes are provided in Appendix A. When ω matches the Larmor frequency $\omega_{^8\text{Li}} = \gamma_{^8\text{Li}} B_{\text{local}}$, determined by the gyromagnetic ratio $\gamma_{^8\text{Li}} = 0.63015$ kHz/G and the local field B_{local} , the ^8Li spins precess about B_{local} , causing depolarization, thus a reduction in the measured average asymmetry. Here, the resonances are conventionally plotted pointing downward in contrast to NMR.

The Larmor frequency is a local property determined by the applied field B_0 and the internal magnetic field at the probe site. Thus, B_{local} may be distributed over a range of values, broadening the nuclear magnetic resonance. The resonance offers insightful information about the magnetic and electronic properties in the material. The linewidth of the resonance measures the inhomogeneities in the static magnetic field sensed by the ^8Li . While, a relative shift of the resonance frequency indicates the presence of a homogeneous static field causing paramagnetic enhancement or diamagnetic reduction of the external field by the electrons surrounding the nucleus. An example of β -NMR resonance is given in Fig. 1.6.

1.1.6 Comparison of β -NMR with NMR and μSR

β -NMR is similar to both NMR and μSR techniques; NMR is the oldest of these three. In all these nuclear techniques, one can measure the static magnetic field distribution and nuclear spin-relaxation. Since the distances

¹Zeeman energy is $E_{\text{mag}} = -\boldsymbol{\mu} \cdot \mathbf{B}_0 = -m\gamma B_0$, where $\boldsymbol{\mu} = \gamma \mathbf{I}$ is the magnetic moment, \mathbf{I} the nuclear spin, and m spin quantum number. The energy splitting is $\Delta E_{\text{mag}} = \gamma B_0$.

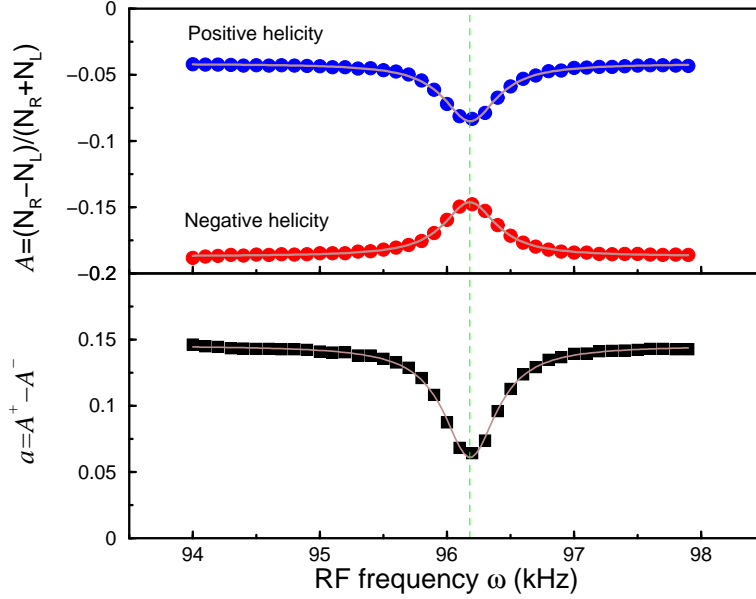


Figure 1.6: (a) Asymmetry of the betas emitted after implanting a 28 keV $^8\text{Li}^+$ beam into a 120 nm Ag film. Both helicities are shown. (b) The difference of the asymmetries of the two helicities is plotted. The solid line is a fit to a Lorentzian, and the dashed line refers to the Larmor frequency. The spectra are taken in $B_0 = 152.6$ G, and $T = 100$ K.

between the probe nuclei in a material are small relative to the source of the field inhomogeneities, the magnetic field distribution is sampled by measuring the fields at the sites of the probe. As long as the probe is uniformly distributed, the sampling is volume-weighted and the field distribution is randomly measured.

There are limitations and difficulties associated with each technique. For example to measure the field distribution of the vortex lattice (VL) in the bulk using NMR, magnetically aligned powders are often used due to the limited sensitivity [13]. However, powders have strong pinning of the vortices at the crystallite surface. It is also challenging to obtain a complete alignment of the crystallites. The penetration of the RF field also limits the range over which the VL can be sampled. Active NMR nuclei in HTSC such as copper and oxygen have quadrupole moments and chemical shifts which

1.1. The β -NMR Technique

complicate data analysis. ${}^8\text{Li}^+$ nucleus of spin $I = 2$ is also quadrupolar and is coupled to the electric field gradient (EFG). The latter is zero by symmetry for ions in cubic sites. Thus, the quadrupolar interaction is only significant when ${}^8\text{Li}^+$ occupies sites of non-cubic symmetry. One can overcome this complication using a probe with zero nuclear quadrupole moment ($I = 1/2$). Currently β -NMR with ${}^{11}\text{Be}$ of $I = 1/2$ is under development.

In a μSR experiment, positively charged muons are implanted one at a time into the sample. The positive muon has a spin $1/2$, a mass that is 206 times the mass of an electron, a gyromagnetic ratio $\gamma_\mu/2\pi = 135.5342$ MHz/T, and a magnetic moment of $4.84 \times 10^{-3} \mu_B$. The muons are naturally 100% polarized due to parity violation. Once implanted into the sample, the muon spin precesses about the local magnetic field B_{local} with a Larmor frequency

$$\omega_L = \gamma_\mu B_{\text{local}}. \quad (1.6)$$

After a life of $\tau_\mu = 2.2 \mu\text{s}$, the positive muon β decays according to

$$\mu^+ \rightarrow e^+ + \nu_e + \bar{\nu}_\mu. \quad (1.7)$$

Similar to β -NMR, the distribution of the decay positrons is asymmetric with respect to the spin polarization of the muon, and the highest probability is along the direction of the muon spin. Thus, the time evolution of the muon spin polarization is monitored by measuring the count rates in scintillators placed around the sample. In μSR , however, one only measures the spectrum in the time domain, and a Fourier transform is needed to find the field distribution in the frequency domain. Measuring the spectrum in the time domain is also an advantage though because one samples all frequencies at once. Another difference between μSR and β -NMR is the time scale of the probe: ${}^8\text{Li}^+$ decays after 1.2 s, and μ^+ after 2.2 μs . Thus, β -NMR is sensitive to spin relaxation processes on much longer times scales than μSR . The smaller beam spots in β -NMR (2-4 mm) compared to μSR (1-2 cm) is an advantage which allows one to study small samples. Conventional μSR is typically done with muons at a high implantation energy of 4.1 MeV, making it a bulk probe with a range $\approx 120 \text{ mg/cm}^2$. Similar to β -NMR,

low-energy muons can be also produced in the lab; thus depth-controlled μ SR is possible. Low-energy μ SR (LE- μ SR), developed at Paul Scherrer institute (PSI) [14], has a lower efficiency for achieving low-energy muons ($10^4/s$) compared to low-energy $^8\text{Li}^+$ in β -NMR ($10^8/s$). Another difference between LE- μ SR and β -NMR is the field range: LE- μ SR is limited to fields below 2 kG, while β -NMR can be done with fields as high as 6.5 T. The above techniques have been very successful in studying HTSC. Some properties of HTSC will be discussed in the next section.

1.2 Generic Properties of HTSC

After the discovery of superconductivity in mercury in 1911, many other superconductors have been discovered (Pb, Nb...etc), but until 1973 the highest T_c was only 23 K in Nb_3Ge . In 1986, a new kind of superconductors was discovered, when Bednorz and Müller detected superconductivity in $\text{La}_{2-x}\text{Ba}_x\text{CuO}_4$ (LBCO) [15]. Rapidly within months, Chu *et al.* were able to drive the initial transition temperature of 35 K up to 50 K using high pressure [16]. One year later another high- T_c material, $\text{YBa}_2\text{Cu}_3\text{O}_{7-\delta}$, was discovered with a transition temperature of 90 K [17]. Since then, by varying the pressure, crystal structure...etc, higher T_c 's have been achieved. Recently, in 2008, new HTSC materials were discovered, containing FeAs as the active layers rather than CuO_2 [18]. A wide variety of FeAs-based materials have been discovered in the last few months, and some hold strong similarities to the CuO_2 -based superconductors.

1.2.1 Crystal Structure

The crystal structure of all cuprate HTSC can be viewed as a stacking of CuO_2 layers sandwiched between planes containing atoms like Cu, O, Ba, La...etc, yielding highly two-dimensional (2D) electronic properties. The mobile superconducting electrons reside in the CuO_2 planes. In Fig. 1.7, the crystal structures of $\text{YBa}_2\text{Cu}_3\text{O}_{7-\delta}$ (YBCO) and $\text{Pr}_{2-x}\text{Ce}_x\text{CuO}_{4-\delta}$ (PCCO) are shown (for $\delta = 0$). YBCO has an orthorhombic unit cell with nearly

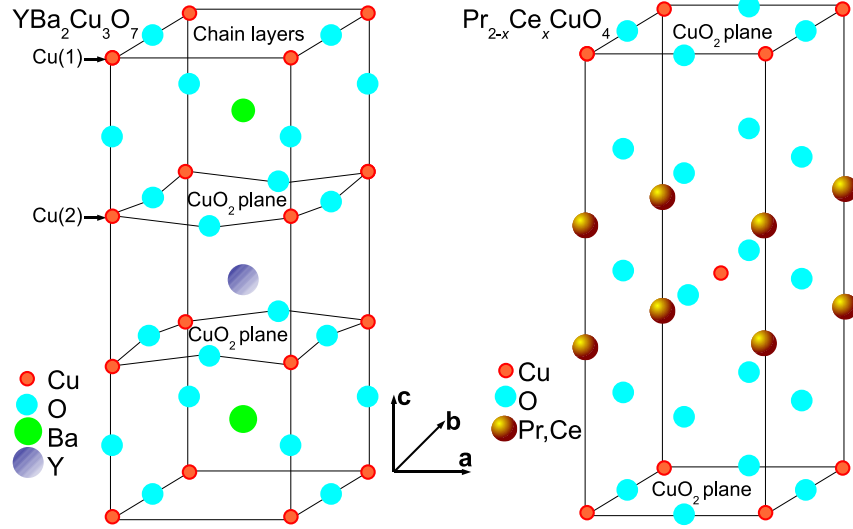


Figure 1.7: Typical crystal structure of $\text{YBa}_2\text{Cu}_3\text{O}_7$ (left) and $\text{Pr}_{2-x}\text{Ce}_x\text{CuO}_4$ (right).

equal in-plane lattice constants $a \approx b$, i.e. it is almost tetragonal, with two CuO_2 planes per unit cell. The $\text{CuO}_{1-\delta}$ plane involves Cu-O chains along the **b** direction, where the oxygen is linear with Cu(1) atoms. It is the missing oxygen between two Cu(1) atoms along the **a** direction that leads to an orthorhombic distortion of the crystal structure [19]. For $\delta = 1$, the Cu-O chains are fully depleted of oxygen and the material becomes an insulating antiferromagnet. PCCO contains one CuO_2 per unit cell, and has the so-called T' tetragonal structure, where the oxygen environment of each Cu atom is in the form of a planar square. In all cuprates, the non- CuO_2 planes are called charge reservoir planes, which capture or give away electrons from or to the CuO_2 planes upon doping [20]. Since it is possible to change the number of copper planes per unit cell and the composition of the layered planes by doping, a large number of compounds has been discovered [21, 22].

1.2. Generic Properties of HTSC

Symbol	Atom number	Atom Configuration	No. of Valence electrons	Ion	Ion configuration
O	8	[He]2s ² 2p ⁴	4	O ¹⁻ O ²⁻	2p ⁵ 2p ⁶
Cu	29	[Ar]3d ¹⁰ 4s ¹	11	Cu ¹⁺ Cu ²⁺ Cu ³⁺	3d ¹⁰ 3d ⁹ 3d ⁸
Sr	38	[Kr]5s ²	2	Sr ²⁺	—
Y	39	[Kr]4d ¹ 5s ²	3	Y ³⁺	—
Ba	56	[Xe]6s ²	2	Ba ²⁺	—
La	57	[Xe]5d ¹ 6s ²	3	La ³⁺	—
Ce	58	[Xe]4f ⁵ 6s ²	4	Ce ⁴⁺	—
Pr	59	[Xe]4f ³ 6s ²	5	Pr ³⁺	6s ²

Table 1.3: Electron configurations of common atoms in cuprate HTSC.

1.2.2 Electronic Configuration

The electronic configuration of some common atoms in cuprates is given in Table 1.3. The most common atom, Cu, has an unusual oxidation state, and assumes a mixed valence state. For example, in YBCO, assuming that Y, Ba, and O have states of 3+, 2+, and 2−, respectively, then for neutrality, Cu must be an average of 2.33+, which could be understood as a mixture of 3+ and 2+ states. The generic oxidation states of the layers in the superconducting YBa₂Cu₃O₇ compound is (CuO)⁺ (BaO) (CuO)²⁻ Y³⁺ (CuO)²⁻ (BaO) with zero net charge per unit cell. The Cu(2) atoms in Cu-O chains appear to be the most oxidized (Cu³⁺), whereas Cu²⁺ are primarily involved in the superconducting CuO₂ planes. Thus, the Cu(2) atoms are regarded as a “sink” which can accept electrons from the superconducting planes in a charge transfer process [23]. It is, however, debatable that instead of oxidation state Cu³⁺ of Cu(2), some of the oxide ions are oxidized to O⁻ rather than O²⁻. Upon reduction of the oxygen in Cu-O chains, the average oxidation state of Cu is reduced and consequently reducing or destroying superconductivity. The parent non-superconducting YBa₂Cu₃O₆ compound (of a tetragonal structure) has no oxygen in the Cu-O chains and the Cu(2) is unaffected (Cu²⁺), whereas Cu(1) is reduced from

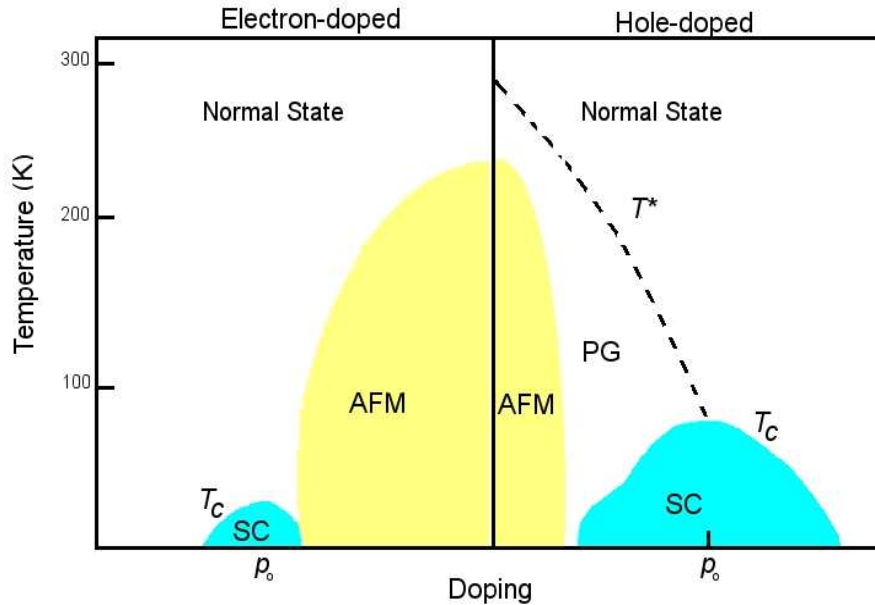


Figure 1.8: The typical doping phase diagrams of hole (right) and electron-doped (left) high- T_c cuprates are shown. The various phases are explained in the text.

Cu^{3+} to Cu^+ .

1.2.3 Doping Phase Diagram

The metallic and superconducting states in most cuprate superconductors are achieved by altering the chemical composition of the parent compounds. For example, in $\text{La}_{2-x}\text{Sr}_x\text{CuO}_{4-\delta}$, one replaces La^{3+} with Sr^{2+} (cation substitution), leading to the loss of one electron by a CuO_2 layer creating more holes in the CuO_2 layers. This is known as hole-doping, which may also be done by oxygen intercalation (in the case of YBCO) or by a combination of these [24]. Superconductivity in PCCO is achieved by substituting trivalent Pr atom by tetravalent Ce, which dopes more electrons into the CuO_2 planes. This is known as electron-doping.

The typical phase diagram of HTSC's is shown in Fig. 1.8. Near zero doping, the material is an antiferromagnetic (AFM) insulator, where the

spins are arranged anti-parallel to one another on adjacent copper atoms in the CuO_2 layers. In hole-doped materials, by increasing the doping, the AFM ordering is destroyed. Below T_c and for adequate doping, the superconducting (SC) state is achieved. The doping level that yields the maximum T_c for a given HTSC material is called *optimal doping* (p_o). The region below (above) p_o is called the underdoped (overdoped) region. In the underdoped (UD) phase with $p < p_o$, the material is in a poor metallic state showing strong 2D anisotropy. This phase is characterized by an intriguing feature of the HTSC's, namely the so-called pseudogap state (PG), where a partial gap opens up in the excitation spectrum below a characteristic temperature T^* [25]. The normal-state of the strongly overdoped regime is believed to be more or less a "Fermi liquid" (FL), i.e. a conventional metallic state. The applicability of the FL theory is questionable in the region close to the optimal doping where the so-called marginal FL theory seems more appropriate [26]. The phase diagram of the electron-doped side of Fig. 1.8 looks similar to hole doping, however the AFM long-range order is robust up to higher doping than the hole-doped side, and the maximum T_c is substantially lower.

There is great interest in the region near the underdoped-overdoped boundary, which is characterized by sharp maxima in a variety of properties near zero temperature [27]. It has been suggested that this is a quantum critical point (QCP) where the quantum critical fluctuations are the origin of strong superconducting pairing and unusual normal state properties in this region such as the PG state [26]. Below the proposed QCP, the system is believed to be in a state of co-existence superconductivity with other competing phases like AFM or PG below T_c , and in a PG state above [27].

1.3 Theoretical Foundations

The search for HTSC's has been and is still empirical, since there is no predictive theory for this type of superconductivity [20]. The famous Bardeen-Cooper-Schrieffer (BCS) [28] theory of conventional superconductivity does not explain the physics of HTSC as it failed to predict their high T_c 's. In

addition to BCS, London [29], and Ginzburg-Landau [30] theories are widely used to discuss the physics of HTSC. These theories will be reviewed in this section.

1.3.1 London Theory

The application of a time-dependent magnetic field to a superconductor generates an electric field. In an ordinary metal this creates the eddy currents; whereas, in a superconductor persistent currents are established [21]. The currents in turn generate a magnetic field of their own, which opposes the applied field. Using Newton's law, $m \frac{d\mathbf{v}}{dt} = -e\mathbf{E}$, the induced current density $\mathbf{J} = -en_s\mathbf{v}$ obeys the equation,

$$\frac{d\mathbf{J}}{dt} = \frac{n_s e^2}{m} \mathbf{E}, \quad (1.8)$$

where n_s is the density of conduction electrons, and m and e are the mass and the charge of an electron, respectively. Using Faraday's law $\nabla \times \mathbf{E} = -\frac{1}{c} \frac{\partial \mathbf{B}}{\partial t}$, and Maxwell's equations $\nabla \times \mathbf{B} = \frac{4\pi}{c} \mathbf{J}$ (c is the speed of light) and $\nabla \cdot \mathbf{B} = 0$, Eq. (1.8) leads to

$$\frac{d}{dt} \left[\nabla^2 \mathbf{B} - \frac{4\pi n_s e^2}{mc^2} \mathbf{B} \right] = 0. \quad (1.9)$$

Initially $\mathbf{B} = 0$, hence the field inside the material would remain zero when an applied field is turned on. The induced magnetization can be obtained via $\mathbf{B} = \mu_0 \mathbf{H} + \mu_0 \mathbf{M} = \mu_0 (\mathbf{H} + \chi \mathbf{H}) = 0$, with μ_0 being the magnetic permeability of free space. Therefore, in addition to its property as a perfect conductor, a superconductor is also a perfect diamagnet ($\chi = -1$), since the induced magnetization completely cancels the applied field.

F. London and H. London explained the Meissner effect by proposing that the term between brackets in Eq. (1.9) must vanish [21]. This leads to the London equation

$$\nabla^2 \mathbf{B} - \frac{\mathbf{B}}{\lambda^2} = 0, \quad (1.10)$$

1.3. Theoretical Foundations

where λ is the London penetration depth

$$\lambda = \left(\frac{mc^2}{4\pi n_s e^2}\right)^{1/2}. \quad (1.11)$$

For an external field B_0 applied parallel to the z -axis, and to the surface of a superconductor occupying half space ($z > 0$), the London equation has a solution of the form

$$B_z = B_0 e^{-z/\lambda}. \quad (1.12)$$

The decrease of the magnetic induction inside the sample in Eq. (1.12) is a result of the *screening* of the external field by the superconducting currents given by

$$J_y = cB_0 e^{-z/\lambda}/4\pi\lambda, \quad (1.13)$$

which flow within a surface layer of thickness λ .

The empirical temperature dependence of λ can be easily found using the phenomenological two-fluid model. One can approximate the free energy of the conduction electrons as [22],

$$F(x, T) = \sqrt{x}f_n(T) + (1-x)f_s(T), \quad (1.14)$$

which depends on the fraction $x = n_n/n$ of the density of the normal state electrons (n_n) to the total density of electrons ($n = n_n + n_s$). The free energy of normal electrons is $f_n(T) \propto -T^2/2$, and the superconducting condensation energy f_s is a constant below T_c and zero above. Minimization of the total free energy with respect to x for fixed T yields

$$x = n_n/n = (T/T_c)^4. \quad (1.15)$$

Using Eqs. (1.11) and (1.15), one finds the temperature dependence of the penetration depth,

$$\lambda(T) = \frac{\lambda(0)}{[1 - (T/T_c)^4]^{1/2}}. \quad (1.16)$$

Reasonable agreement of measured $\lambda(T)$ with the above form is seen in some conventional superconductors like lead [31], although deviations are found

in other materials especially HTSC.

1.3.2 Ginzburg-Landau Theory

Ginzburg and Landau introduced a pseudo-wavefunction $\psi(\mathbf{r}) = |\psi(\mathbf{r})|e^{i\phi}$, which is a complex order parameter of phase ϕ , to represent the local density of the superconducting electrons $n_s(\mathbf{r}) = |\psi(\mathbf{r})|^2$. The free energy of the quantum state proposed by Ginzburg-Landau (GL) theory in 1951 takes on the form

$$F = F_n + \alpha|\psi(\mathbf{r})|^2 + \frac{\beta}{2}|\psi(\mathbf{r})|^4 + \frac{1}{2m} \left| \left(-i\hbar\nabla - \frac{2e\mathbf{A}}{c} \right) \psi \right|^2 + \frac{B^2}{8\pi}, \quad (1.17)$$

where F_n is the free energy of the normal state, \mathbf{A} the vector potential related to the external field $\mathbf{B} = \nabla \times \mathbf{A}$, and $\frac{B^2}{8\pi}$ is the magnetic energy density. By minimizing this free energy with respect to ψ and \mathbf{A} , it is found that the parameter α must change sign at T_c , while β assumes a constant value. The GL equations determining the spatial variations of the order parameter and the vector potential are given by

$$\xi^2 \left[\nabla + \frac{2\pi i}{\Phi_0} \mathbf{A} \right] \psi + \left(1 - \frac{\beta|\psi|^2}{|\alpha|} \right) \psi = 0, \quad (1.18)$$

$$\lambda^2 \frac{\beta}{\alpha|\psi|^2} \nabla \times \nabla \times \mathbf{A} + \mathbf{A} = -\frac{\Phi_0}{2\pi} \nabla \phi. \quad (1.19)$$

The length scales entering these equations are the London penetration depth $\lambda(T)$ (Eq. (1.11)) and the coherence length $\xi(T)$,

$$\xi^2(T) = \frac{\hbar^2}{2m\alpha} = \xi_0^2(1 - T/T_c)^{-1}, \quad (1.20)$$

$$\lambda^2(T) = \frac{mc^2\beta}{16\pi e^2|\alpha|^2} = \lambda_0^2(1 - T/T_c)^{-1}, \quad (1.21)$$

determining the length scale of variations in the order parameter and vector potential, respectively. The GL results only apply very close to T_c where ψ

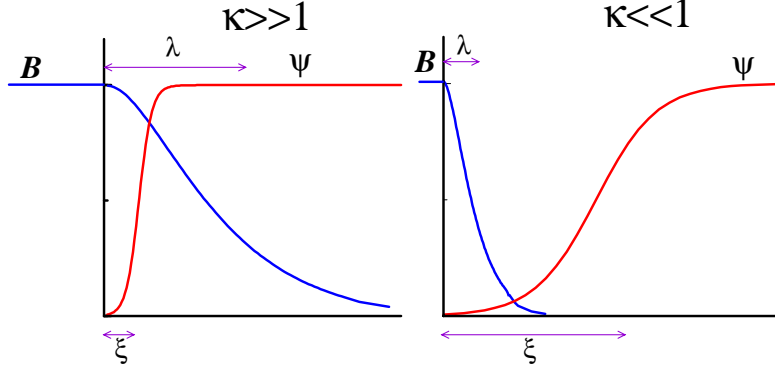


Figure 1.9: Idealized spatial variation of the magnetic field B and order parameter ψ for $\kappa \ll 1$ (type I) and $\kappa \gg 1$ (type II) superconductors.

is small. The dimension-less Ginzburg-Landau parameter is defined by

$$\kappa = \frac{\lambda(T)}{\xi(T)}. \quad (1.22)$$

The boundary between the normal and superconducting region involves a surface energy. A crossover from positive to negative surface energy occurs for $\kappa = 1/\sqrt{2}$. For $\kappa > 1/\sqrt{2}$ the negative surface energy causes penetration of quantized vortices in type II superconductors, whereas $\kappa < 1/\sqrt{2}$ in type I superconductors. The spatial variations of the order parameter and magnetic field inside type I and II superconductors is shown in Fig. 1.9.

The GL equations are only applicable near T_c as the order parameter in that region is weak with small variations in space. However if one ignores the spatial variation of the order parameter, one can construct an approximate free energy valid at all temperatures from the magnetic density and kinetic energy of the currents,

$$F = \frac{1}{8\pi} \left(\mathbf{B}^2 + \lambda^2 (\nabla \times \mathbf{B})^2 \right). \quad (1.23)$$

Variation of this free energy with respect to \mathbf{B} leads to the London equation given in Eq. (1.10). Gor'kov showed that the Ginzburg-Landau theory could be also derived from BCS theory, and leads to similar results close to T_c [32].

1.3.3 BCS Theory

The superconducting state in conventional superconductors has been explained microscopically by the BCS theory [28]. The latter is based on an effective attractive interaction between electrons induced by phonon exchange. This attraction dominates the repulsive Coulomb interaction for electrons at the Fermi level. In the superconducting ground state, the electrons are virtually excited in pairs of electrons with opposite spin and momentum known as Cooper pairs. The BCS theory uses a many-body theory to construct an explicit wave-function for the ground state, which is then used to calculate different quantities. The BCS Hamiltonian takes on the form [28]

$$H = \sum_{\mathbf{p}\sigma} \epsilon_{\mathbf{p}} c_{\mathbf{p}\sigma}^{\dagger} c_{\mathbf{p}\sigma} + \frac{1}{2} \sum_{\mathbf{q}\mathbf{p}\mathbf{p}'\mathbf{s}\mathbf{s}'} V(q) c_{\mathbf{p}+\mathbf{q},\mathbf{s}}^{\dagger} c_{\mathbf{p}'-\mathbf{q},\mathbf{s}'}^{\dagger} c_{\mathbf{p}',\mathbf{s}'} c_{\mathbf{p},\mathbf{s}}. \quad (1.24)$$

Here, $\epsilon_{\mathbf{p}} = \frac{\mathbf{p}^2}{2m}$ is the single-electron kinetic energy and $c_{\mathbf{p},\sigma}$ ($c_{\mathbf{p}\sigma}^{\dagger}$) is the creation (annihilation) operator of an electron of momentum \mathbf{p} and spin σ . The attractive interaction $V(q)$ between electrons in the neighborhood of the Fermi surface is essential to establish the formation of Cooper pairs. Solving the BCS Hamiltonian leads to the energy spectrum $E_p = \sqrt{\epsilon_{\mathbf{p}}^2 + \Delta^2}$ where Δ is the energy gap with a spherical symmetry (s -wave symmetry).

The BCS theory successfully predicts a transition temperature of the form

$$k_B T_c = 1.14 \hbar \omega_c \exp\left(-\frac{1}{N_F V_0}\right), \quad (1.25)$$

where N_F is the density of states near the Fermi level. The phonon cutoff frequency ω_c is related to the Debye frequency $\omega_D \propto 1/\sqrt{M}$, where M is the atomic mass, which explains why $T_c \propto 1/\sqrt{M}$, i.e. the isotope effect. The energy gap in the weak limit $\Delta \ll \hbar \omega_D$ is found to be proportional to T_c and is given by the ratio

$$\frac{2\Delta(0)}{k_B T_c} \approx 3.5. \quad (1.26)$$

The temperature dependence of the gap is given implicitly by

$$\Delta(T) = \Delta(0)e^{f(\Delta(T)/k_B T)}, \quad (1.27)$$

where f is a universal function of the ratio $\Delta(T)/k_B T$. Near T_c ,

$$\Delta(T) = 1.74\Delta(0)(1 - T/T_c)^{1/2}. \quad (1.28)$$

The penetration depth in BCS at low temperatures follows

$$\frac{\lambda(T) - \lambda(0)}{\lambda(0)} = \sqrt{\pi\Delta(0)/2k_B T} e^{-\Delta(0)/k_B T}. \quad (1.29)$$

The BCS gap function also provides the microscopic interpretation of the Ginzburg-Landau order parameter. Gor'kov showed that the BCS gap function Δ is simply proportional to the Ginzburg-Landau parameter ψ

$$\psi \propto \Delta. \quad (1.30)$$

This is somewhat expected since both ψ and Δ are complex functions, and both vanish above T_c . Below T_c , when the gap opens up at the Fermi level, the order parameter becomes non-zero. Thus, these two parameters are related to each and have the same symmetry, and both reflect the symmetry of the pairing interaction. The latter, in HTSC, is now widely accepted to be of a $d_{x^2-y^2}$ -wave (d -wave) nature in contrast to the s -wave symmetry of conventional superconductors like Nb. However, near the surface and defects, order parameters of other symmetries may compete with the d -wave symmetry leading, to co-existence of more than one order parameter that could potentially break *time-reversal symmetry* (TRS) [1]. This will be discussed in the next section.

1.4 Time-Reversal Symmetry Breaking in HTSC

Under time-reversal one transforms time t , spin \mathbf{S} , and momentum \mathbf{p} to $-t$, $-\mathbf{S}$, $-\mathbf{p}$, respectively. Time-reversal symmetry also transforms an order

parameter $\psi = |\psi|e^{i\phi}$ to its complex conjugate

$$\mathcal{T}[\psi] = \psi^* = |\psi|e^{-i\phi}. \quad (1.31)$$

This symmetry is considered broken if the state under this operation is different from the original one (not only by a phase factor). For example, for a combination of two order parameters $\psi + \psi'$, TRS is broken if

$$\mathcal{T}[\psi + \psi'] \neq e^{i\gamma}(\psi + \psi'), \quad \text{for } \gamma \equiv \phi - \phi' \neq 0, \pi. \quad (1.32)$$

Thus, the order parameter $\psi + \psi'$ and its time inverse $\psi^* + \psi'^*$ are degenerate, i.e. they have the same free energy.

1.4.1 Which Order Parameters Break TRS?

There are many allowed symmetries of the pairing state of superconductivity [33]. The amplitude and phase of the leading candidates are plotted in Fig. 1.10. The simplest is the isotropic s -wave pairing state which occurs in most conventional superconductors, where the order parameter is independent of the wave-vector \mathbf{k} and has a spherical symmetry,

$$\Delta(\mathbf{k}) = \Delta_0. \quad (1.33)$$

In real metals, the crystal structure leads to a small anisotropy of the isotropic s -wave, giving rise to an anisotropic s -wave. In HTSC, the d -wave symmetry is now well established, with a gap function

$$\Delta(\mathbf{k}) = \Delta_0[\cos(k_x a) - \cos(k_y a)]. \quad (1.34)$$

Here Δ_0 is the maximum gap value and a is the in-plane lattice constant. This gap has strong anisotropic magnitude with nodes ($\Delta(\mathbf{k}) = 0$) along the (110) direction in \mathbf{k} space and a sign change in the order parameter between the lobes in the k_x and k_y directions. Physically, this sign change indicates a relative phase of π in the superconducting condensate wave function for Cooper pairs with orthogonal relative momenta. In the cuprates, this state is

believed to describe the order parameter in the CuO_2 planes, with the lobes being aligned with the in-plane lattice vectors \mathbf{a} and \mathbf{b} . Another candidate symmetry is the d_{xy} -wave which is similar to the d -wave but rotated by 45° , and has the gap function

$$\Delta(\mathbf{k}) = \Delta_0 \sin(k_y a) \sin(k_x a). \quad (1.35)$$

A variety of experiments have been performed to determine the symmetry of the order parameter. One class of experiments considers the properties of the quasi-particle excitations in the superconducting state which modifies the low temperature dependence of various thermodynamic quantities such as the penetration depth. The microwave measurements of the temperature dependence of the penetration depth were the first to confirm the d -wave nature in YBCO crystals [34]. Later angle resolved photo emission spectroscopy (ARPES) [35], NMR [36], Raman scattering [37], μSR [38], neutron scattering [39], and other experiments have all reached the same conclusion. Another class of experiments probes the pairing symmetry by studying the relative phase of the gap between different points on the Fermi surface. Studies of the magnetic flux modulation of DC superconducting quantum interference devices (SQUID) provided direct evidence of d -wave from the π shift between pairs tunneling along the a and b directions [40].

All conventional superconductors conserve time-reversal symmetry because of the single isotropic s -wave pairing symmetry. In the bulk, HTSC, also appears to conserve TRS due to the single component d -wave symmetry. However, near surfaces, interfaces, vortices, impurities, or structural defects, local pair breaking effects can suppress the d -wave order parameter and lead the way for an order parameter of different symmetry, like d_{xy} -wave or s -wave. The new pairing component together with the dominant d -wave component can form a complex order parameter. Complex mixtures of the above symmetries namely the $d + is$ and the $d + id_{xy}$ states are respectively given by

$$\Delta(\mathbf{k}) = \Delta_0 \left\{ (1 - \epsilon) [\cos(k_y a) - \cos(k_x a)] + i\epsilon \right\}, \quad (1.36)$$

1.4. Time-Reversal Symmetry Breaking in HTSC

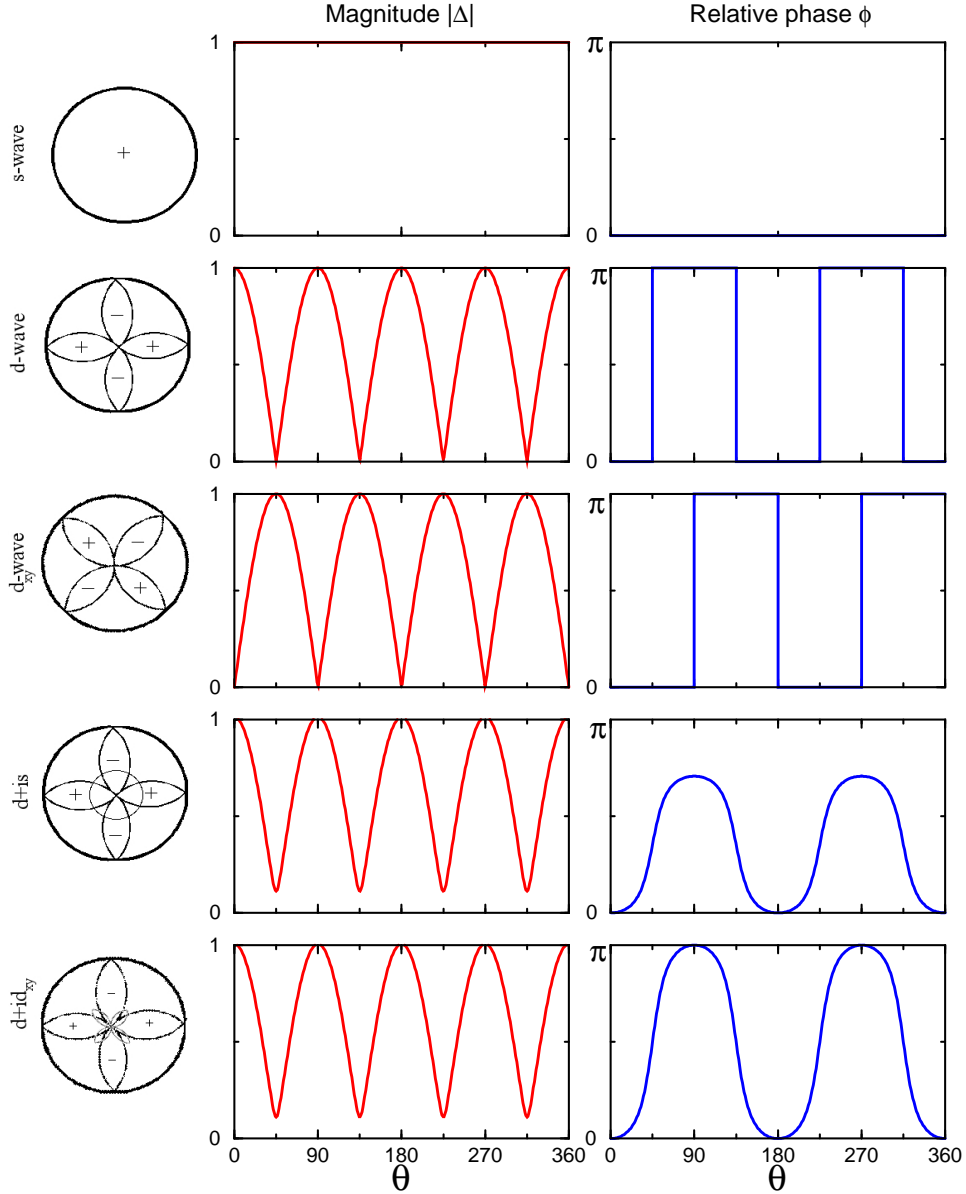


Figure 1.10: Normalized amplitude and phase of the main candidate order parameters in HTSC are shown. The order parameter is written as $\Delta = |\Delta|e^{i\phi} = |\Delta|g(\theta)$. Here θ is a polar angle in momentum space $\mathbf{k} = k(\cos \theta, \sin \theta)$; $g(\theta) = \cos(2\theta + \alpha)$, where $\theta = 0$ for s -wave and finite for d - and d_{xy} -wave; $\alpha = 0$ ($\pi/2$) for s -wave and d -wave (d_{xy} -wave).

$$\Delta(\mathbf{k}) = \Delta_0 \left\{ (1 - \epsilon) [\cos(k_y a) - \cos(k_x a)] + i\epsilon \sin(k_y a) \sin(k_x a) \right\}, \quad (1.37)$$

where ϵ is the fraction of the sub-component s or d_{xy} . The ferromagnetic states $d + id_{xy}$ can directly couple to an external magnetic field via its net orbital momentum or spin [41, 42].

These complex order parameters represent a TRS broken state, and are also associated with the opening of a gap in the quasi-particle density of states which lowers the local free energy density [1]. A direct evidence of a TRSB state is the presence of spontaneous supercurrents and magnetic fields if the Cooper pairs carry a finite angular momentum of either the spin or orbital (or both) parts of the pair wave-function [1]. TRSB superconductors must still exhibit the Meissner effect where the compensating screening currents are set up to ensure that $B = 0$ in the bulk of the sample. Although these effects mean that no large bulk magnetic moment is to be expected, the sample will always contain surfaces and defects where the Meissner screening of the TRSB fields is not perfect, and a small magnetic signal is thus expected locally. Other features include unusual tunneling spectra and the appearance of fractional vortices [1]. The occurrence of TRSB in HTSC is still controversial as different studies have lead to contradictory results. The findings of a few leading experimental and theoretical studies will be summarized in the rest of this section. Due to the large number of papers published about this topic, I will only discuss those most relevant to the experiments described in Chapter 2.

1.4.2 Theories

Let me briefly review some of the leading theories that addressed the possible occurrence of TRSB in HTSC. Several theories have been formulated, but one can classify most of them into those that: (i) considered the effect of intrinsic and extrinsic structural defects such as grain boundaries, twin boundaries, Josephson junctions, and domains walls, (ii) proposed a locally broken TRS near the interface of d -wave superconductors, and (iii) studied the effect of magnetic impurities on the order parameter which may induce

spontaneous magnetic moments in the vicinity of the impurities.

Structural Defects

Sigrist and co-workers have studied the current and field distribution near grain boundary junctions between two superconductors with different order parameters on each side of the boundary [43, 44, 45]. Their calculations, in the framework of GL theory, showed the appearance of fractional vortices at the boundary below temperatures $T^* \ll T_c$. This is generated by circular currents flowing in the x-y plane which cancel in the homogeneous superconducting phase but survive in the inhomogeneous region near the interface [45]. The magnetic field generated by these currents has a peak near the interface with a width of the order of the coherence length. Away from the interface, the field changes sign and decays on the length scale of λ . It was shown that the positive and negative parts of the field cancel each other leading to zero net magnetization [45]. Amin *et al.* studied the current and field distribution in systems with grain boundaries involving a mixture of *s* and *d*-wave symmetries by numerically solving the self-consistent quasi-classical Eilenberger equations [46]. The magnitude of the calculated field is of the order of a mG, and decays on the length scale of few coherence lengths. The total flux generated by these TRSB states is thus very small and difficult to detect.

Several papers considered the role of twin boundaries [47, 48, 49, 50, 51]. Feder *et al.* used the Bogoliubov-deGennes formalism to study TRSB near the twin boundaries in *d*-wave superconductors [47]. They assumed an induced *s*-wave pairing potential below a temperature T^* which depends strongly on the electron density in the twin boundary. This leads to signs of TRSB below $T^* \sim 0.1T_c$. Belzig *et al.* used a quasi-classical formalism of superconductivity to study the effect of twin boundaries on the electronic structure [49]. They found that at low temperatures (~ 5 K), a localized TRSB state near the twin boundary appears, and spontaneous currents flow parallel to the twin boundary. In Ref. [48], it was found that an admixture of *s*- and *d*-wave near the twin boundaries due to the orthorhombic distortion

in materials such as $\text{YBa}_2\text{Cu}_3\text{O}_{7-\delta}$ may lead to spontaneous fields of the order 5 – 50 G which decay on the length scale of the twin inter-spacing. Yang and Hu also suggested in Ref. [52], that a small s -wave component may arise due to the orthorhombic distortion in YBCO and may lead to TRSB.

Quasi-Particle Reflection from the Surface

C.-R. Hu was the first to suggest that a quasi-particle reflecting from a surface of a d -wave superconductor, with nodes of the order parameter being normal to the sample surface, experiences a sign change in the order parameter leading to zero energy states (ZES) at the surface [53]. These states are also expected if the superconductor is coated with a normal metal, and are absent in s -wave superconductors as well as at the (100) surface of a d -wave superconductor [52]. The consequence of the ZES is an increase in the local density of states at the Fermi level at the surface, resulting in zero-bias conductance peak (ZBCP) anomaly observed in tunneling spectroscopy of HTSC [54]. Under the influence of an applied magnetic field or a strong spontaneous field, the spectrum of surface states acquires a Doppler shift with energy given by $\mathbf{v}_f \cdot \mathbf{p}_s$, where the \mathbf{v}_f is the Fermi velocity, and \mathbf{p}_s is the momentum of the bound states which depends on the local magnetic field. This leads to a splitting of the ZBCP into two states above and below the Fermi level [56, 57, 58]. In this way, the quasiparticle contribution to the free energy can be lowered, with the appearance of TRSB spontaneous currents near the surface. The splitting of the zero-energy level leads to an imbalance in the occupation between electrons states with momentum components parallel and antiparallel to $(1, \bar{1}, 0)$. Thus, there is a finite current along the surface whose direction depends on which of the two degenerate time-reversal symmetry states is realized.

Fogelström, Rainer, and Sauls extended Hu's work and showed that a large ZBCP is possible for all orientations if the interface is microscopically rough [55]. The authors found that surface states are induced in (100) as a result of Andreev scattering by the rough surface. Their calculations for a

(110) surface showed the current density approaches the London limit (see Eq. (1.13)) for $\xi \ll x \ll \lambda$. At $x \leq \xi$, a current is carried by the ZES and counter-flows relative to the Meissner currents. This ZES current scales linearly with the applied field and leads to the splitting of the ZBCP. The ZES lead to pair breaking and the electrons may be paired by a sub-dominant pairing channel, resulting in a spontaneous current which splits the ZBCP even in zero external field below a transition temperature T_s . This spontaneous current is confined within few coherence lengths of the surface. The ZES splitting varies non-linearly with increasing field, and saturates at fields of the order of 3 T. The authors also indicated that surface roughness suppresses T_s , and also decreases the intensity of the ZBCP above T_s . The same conclusion was reached by Asano and Tanaka in Ref. [59], when considering the interface between a normal metal and a d -wave superconductor.

Near the surface, one may also consider the role of Abrikosov vortices which generate an essentially inhomogeneous superfluid velocity field, which leads to a nontrivial electronic structure of the surface-bound state [60, 61].

TRSB States Induced by Impurities

Local spontaneous currents can be also induced by magnetic and non-magnetic impurities. Asano *et al.* found that the scattering by impurities near the interface of a normal metal and a (110) d -wave superconductor splits the ZBCP in the same way that a d -is order parameter does [59, 62]. The splitting disappears at sufficiently high temperature and increases with external applied fields. In the bulk, Balatsky suggested that a TRSB complex order parameter is “generated around a magnetic impurity in the presence of coupling between the orbital moment of the condensate and impurity spin S_z ” [63]. He argues that a sub-dominant order d_{xy} develops simultaneously with the impurity spins. He also noted that a magnetic field applied parallel to the layers $H \gg B_{c1,ab} \sim 1$ G suppresses the d_{xy} order as the coupling between the impurities and d_{xy} vanishes.

Okuno has studied the effect of impurities in a TRSB superconductor, and found that a spontaneous current can be induced near the impurities

with patterns that reflect the nature of the pairing channels and vanishes a few lattice constants from the impurity [42]. Choi and Muzikar have also drawn a similar conclusion where the magnetic impurities strongly perturb the order parameter on a length scale of ξ , but that leads to zero net magnetization [64].

1.4.3 Experiments

μ SR

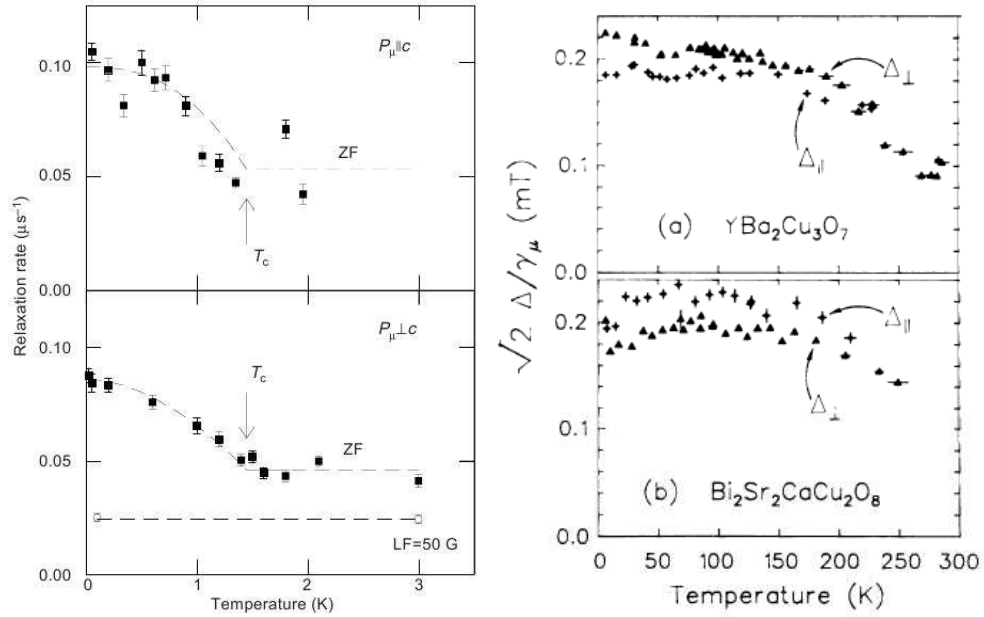


Figure 1.11: Left: the μ SR relaxation rate in Sr_2RuO_4 showing the appearance of spontaneous magnetic fields below T_c [3]. Right: absence of spontaneous magnetic fields in YBCO ($T_c=90$ K) and BSCCO ($T_c=85$ K) systems [65]. In μ SR, the relaxation rate is a measure of the spread of the internal fields.

The most direct consequence of TRSB would be the appearance of spontaneous magnetic fields, which can be resolved by a sensitive local magnetic probe such as μ SR. TRSB violated throughout the whole material is clearly observed in some unconventional superconductors such as heavy Fermion

superconductors $U_{1-x}Th_xBe_{13}$ [2], and Ru-based superconductors Sr_2RuO_4 [3], and $PrOs_4RuSb_{12}$ [4]. However, bulk studies of HTSC showed little evidence of spontaneous magnetic fields. Kiefl *et al.* studied YBCO powders and $Bi_2Sr_2Cu_2O_{8+\delta}$ (BSCCO) thick films using μ SR and observed internal magnetic fields consistent with the nuclear dipolar fields with no signs of TRSB fields below T_c [65]. The authors concluded that the spontaneous fields due to TRSB, if existent, are less than 0.8 G.

Contrary to Kiefl's finding, Sonier *et al.* measured weak magnetism in YBCO single crystals using zero field μ SR, with the onset being well below T_c for optimally doped and above T_c for underdoped samples [66]. This effect may be due to TRSB above T_c as proposed by Varma [67], or the Cu-O chains in YBCO [68, 69]. Recent similar studies of single crystals $La_{2-x}Sr_xCuO_{4-\delta}$ of different doping using zero-field μ SR have concluded the absence of measurable strong TRSB fields above T_c in both the underdoped and overdoped regimes in contradiction to Varma's predictions [70].

Tunneling Spectroscopy

Spontaneous splitting of the ZBCP, in zero magnetic field, was seen by Covington *et al.* below 7 K in ab-oriented YBCO optimally doped thin films by planar tunneling spectroscopy as shown in Fig. 1.12 [56]. External applied magnetic fields parallel to the surface induces the ZBCP to split more beyond its zero field value, varying non-linearly with increasing field. This splitting of ZBCP was attributed to a transition to a state of broken time-reversal symmetry with a $d+is$ order parameter. Deutscher and collaborators have shown that such splitting takes place at 4.2 K only beyond some critical doping level, close to optimal, and increases with strong magnetic field (1-5 T) applied parallel to the surface of the (110)-oriented films [71, 72]. The same effect was also observed by Sharoni *et al.* [73] below a critical temperature ≈ 10 K in optimally doped and overdoped thin (110) YBCO films and absent in underdoped films. Deutscher and collaborators measured the Andreev reflections between Au STM (scanning tunneling microscopy) tip and Ca doped YBCO thin films, and found a conductance spectra in (100)

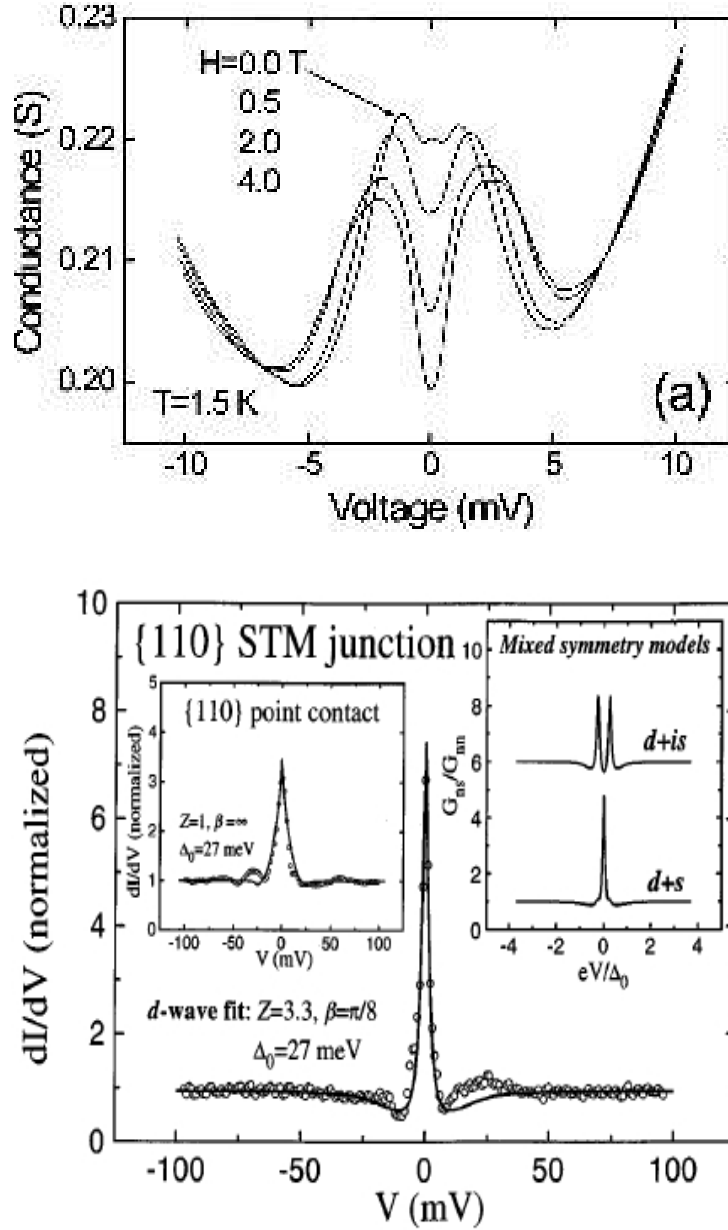


Figure 1.12: Top: conductance in YBCO/Cu tunnel junction showing splitting of the ZBCP as a function of external field [56]. Bottom: absence of the splitting of the ZBCP in the normalized conductance spectra taken on the (110) surface of YBCO with a Pt-Ir tip at 4.2 K for an STM tunnel junction (main panel) and for a point contact (left inset). Right inset shows the expected curves from $d+s$ and $d+is$ symmetries. [54].

best fitted with $d+is$ complex order parameter, with a ratio of the energy gaps $\Delta_d/\Delta_s \sim 0.1 - 0.8$ [74].

Other tunneling studies have led to different conclusions. In tunneling experiments on Ag/YBCO junctions, a strong ZBCP was observed in (110) junctions with no splitting of the ZBCP in external fields up to 5 T [76]. Similarly, directional tunneling and point contact spectroscopy on (001), (100), and (110) faces of YBCO single crystal done by Wei *et al.* showed a no splitting of the ZBCP in (110) and (100) as shown in Fig. 1.12. Quantitative spectral analysis done by the authors suggested a dominant d -wave symmetry with less than 5% s -wave in mixed $d+s$ or $d+is$ [54]. Yeh *et al.* scanning tunneling measurements of a YBCO single crystal showed signs of ZBCP splitting only in Ca, Zn, Mg doped samples while absent in under and optimally doped samples along the (110) and (100) directions [77].

SQUID Microscopy

Macroscopic magnetometry is not expected to yield a signal from TRSB and will be dominated by the Meissner signal of the bulk. In certain geometries, sensitive SQUID magnetometers can be used to seek fields near surfaces. Carmi *et al.* have measured a spontaneous weak magnetic field ($\approx 30 \times 10^{-6}$ G) picked up by a SQUID near c -axis oriented YBCO epitaxial thin films [78]. By cooling the films in zero field, a small magnetic flux appears abruptly at T_c with weak temperature dependence below as shown in Fig. 1.13-(a). This signal was found to be thickness and orientation independent, and did not change appreciably if measured at the edges of the sample.

Tafari and co-workers have also detected spontaneous magnetization using scanning SQUID microscopy near c -axis films [80]. Using a square pick up coil a few microns across, images of flux were taken near (001)/(103) grain boundaries junctions. A broader flux distribution was imaged in (001) but absent in (103) as seen in Fig. 1.13-(b). The total flux appears to be a fraction of the superconducting flux quanta. Spontaneous magnetic flux was also measured near asymmetric 45° grain boundary of c -axis YBCO films in zero field by Mannhart *et al.* [79]. The authors attributed the result to

1.4. Time-Reversal Symmetry Breaking in HTSC

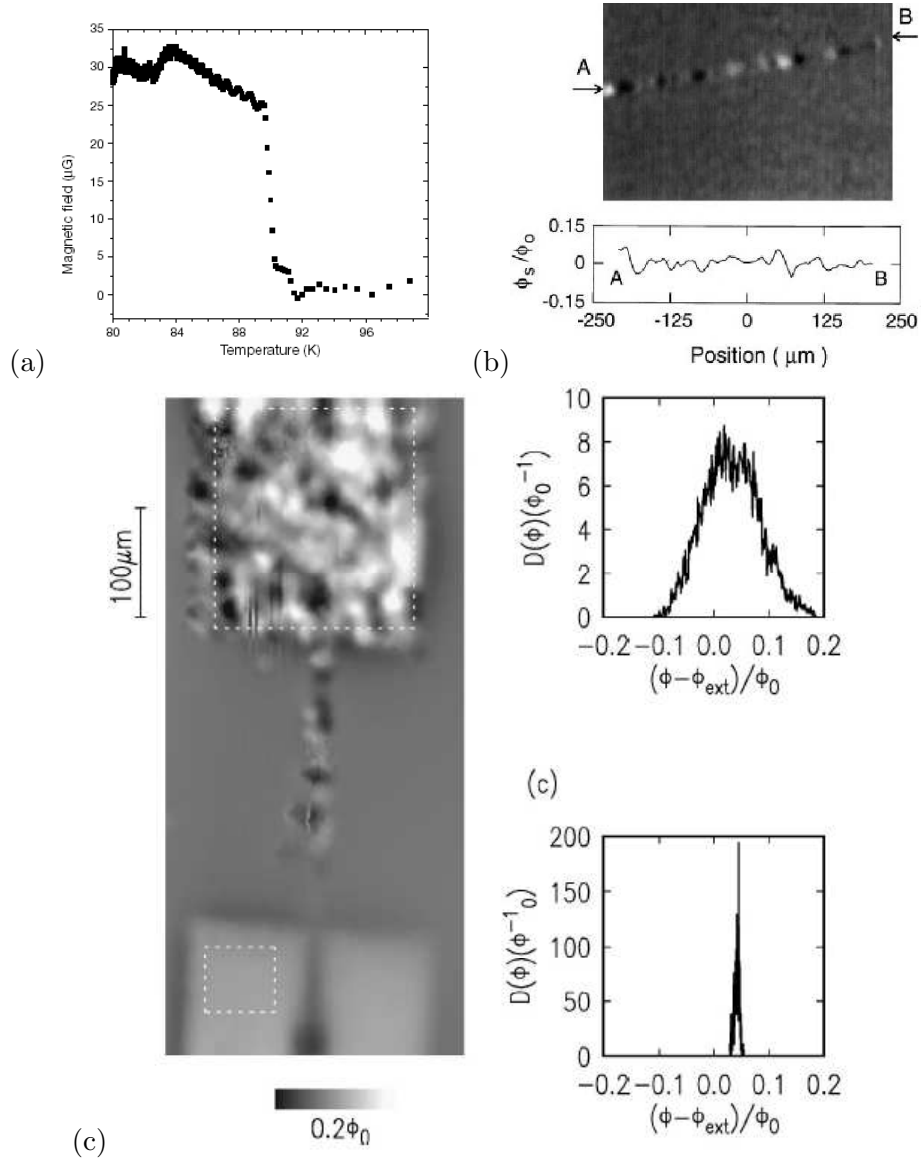


Figure 1.13: (a) Spontaneous magnetic field generated by a thin YBCO film plotted versus temperature, as measured by Carmi *et al.* [78]. (b) Scanning SQUID microscope image of an area with a 45° asymmetric c -axis YBCO bicrystal grain boundary of 180 nm thickness. The flux through the grain boundary is shown [79]. (c) Scanning SQUID images of (100)/(103) YBCO cooled in 3mG. The corresponding flux distribution is shown. A broader field distribution is observed in (001), although it has the same average flux as in (103) [80].

fluctuations of the d -wave order parameter through the faceting of the grain boundaries, over a length scale of few microns.

The TRSB superconducting state may also exist in the vortex phase. However, the magnetic field inhomogeneities in this phase will be dominant at high fields. Next, we discuss the response of the cuprates to high applied magnetic fields above B_{c1} .

1.5 Vortex Lattice in HTSC

Increasing the external field beyond B_{c1} , the formation of vortices becomes energetically favorable and we enter the vortex state. Four energies compete in this state and determine the arrangement of the vortices [81]. (i) The repulsive interaction between the vortices leads to a three-dimensional (3D) lattice where the vortices are straight lines arranged in a triangular lattice. (ii) Vortex pinning by defects may lead to a random amorphous glass state. (iii) The CuO_2 planes decoupling modifies the 3D lattice to 2D or pancake vortices. (iv) The thermal fluctuations compete with the tendency to form the lattice and cause thermally activated depinning of the vortices and melting the VL to a liquid phase. The energies from (i) to (iv) are controlled by external magnetic field, defects, anisotropy, and temperature, respectively. The competition between these energies gives rise to a VL structure with features that could be identified by several techniques. The features of the field distribution due to a regular VL, the effect of energies (i) to (iv), and examples of some measurements will be covered in this section.

1.5.1 Regular VL Characteristics

Provided that the repulsive interaction is dominant, the magnetic vortices form a regular vortex lattice with a lattice constant a . Numerous theories and experiments have confirmed that the vortices are typically arranged into a triangular VL [82]. The area occupied by each vortex in a triangular unit cell is $A = \frac{\sqrt{3}}{2}a^2$, and for an average field $B_0 = \frac{\Phi_0}{A}$, the vortex spacing is

thus,

$$a = \sqrt{\frac{2 \Phi_0}{\sqrt{3} B_0}} = \frac{1546 \text{ nm}}{\sqrt{B_0 \text{ (mT)}}}. \quad (1.38)$$

The magnetic field profile of the VL can be found using different methods: GL theory, Bogoliubov-deGennes theory,...etc. Unfortunately most theories are only applicable at certain temperatures/fields, and have too many unknown parameters to be used to fit the experimental data [82]. Because of its simplicity, the London model provides the most convenient way of calculating the magnetic fields inside a HTSC. The model is only applicable for extreme type II superconductors with $\lambda \gg \xi$, and is valid at all temperatures below T_c , and fields $B_0 \ll B_{C2}$. All these conditions are satisfied in β -NMR and μ SR experiments.

For magnetic fields applied along the z -direction parallel to the crystallographic c -axis of the superconductor, the spatial dependence of the magnetic field inside the superconductor ($z \geq 0$), can be found by modifying the London equation (Eq. (1.10)) to account for vortices,

$$\mathbf{B}(\mathbf{r}) - \lambda^2 \nabla^2 \mathbf{B}(\mathbf{r}) = \hat{\mathbf{z}} \Phi_0 \sum_{\mathbf{R}} \delta(\mathbf{r}_{\perp} - \mathbf{R}). \quad (1.39)$$

Here $\lambda = \lambda_{ab} = \sqrt{\lambda_a \lambda_b}$, $\delta(\mathbf{r}_{\perp})$ is a 2D delta function, $\mathbf{r}_{\perp} = x\hat{\mathbf{x}} + y\hat{\mathbf{y}}$ is a 2D vector in the xy plane, $\mathbf{r} = \mathbf{r}_{\perp} + z\hat{\mathbf{z}}$, and $\mathbf{R} = a[(m + \frac{n}{2})\hat{\mathbf{x}} + n\frac{\sqrt{3}}{2}\hat{\mathbf{y}}]$ are the vortex positions. Outside the superconductor ($z \leq 0$), the magnetic field follows the equation

$$-\nabla^2 \mathbf{B}(\mathbf{r}) = 0. \quad (1.40)$$

Throughout this work we are only working with the z -component of the magnetic field $B_z = \hat{\mathbf{z}} \cdot \mathbf{B}$, and refer to it for simplicity as B . The transverse field B_{\perp} can be neglected as it contributes a second order correction to the spin Hamiltonian, while the longitudinal field results in a first order correction. The longitudinal component can be found by solving Eqs. (1.39) and (1.40) using the Fourier transform,

$$B(\mathbf{r}) = B_0 \sum_{\mathbf{k}} F(\mathbf{k}) e^{i\mathbf{k} \cdot \mathbf{r}}, \quad (1.41)$$

$$F(\mathbf{k}) = \frac{1}{\Phi_0} \int_{\text{cell}} d\mathbf{r}_\perp B(\mathbf{r}) e^{-i\mathbf{k}\cdot\mathbf{r}}. \quad (1.42)$$

The Fourier components $F(\mathbf{k})$ take on the form

$$F(\mathbf{k}) = \frac{1}{\lambda^2} \left[\frac{\Theta(-z)e^{kz}}{\Lambda(\Lambda+k)} + \frac{\Theta(z)}{\Lambda^2} \left(1 - \frac{k}{\Lambda+k} e^{-\Lambda z}\right) \right]. \quad (1.43)$$

Here $\Lambda^2 = k^2 + \frac{1}{\lambda^2}$, and $\mathbf{k} = \frac{2\pi}{a} [n\mathbf{x} + \frac{2m-n}{\sqrt{3}}\mathbf{y}]$ are the 2D reciprocal lattice vectors of the triangular VL, and $\Theta(z) = 1$ for $z \geq 0$ and zero otherwise. In the bulk ($z \gg a, \lambda$), the magnetic field simplifies to

$$B(\mathbf{r}) = B_0 \sum_{\mathbf{k}} \frac{e^{i\mathbf{k}\cdot\mathbf{r}}}{1 + k^2\lambda^2}. \quad (1.44)$$

This result diverges on the axis of the vortex line at \mathbf{R} . To account for the finite size of the vortex core, and correct the unphysical divergence of B at the vortex cores, the Fourier components are multiplied by a cutoff function $C(k)$ which is approximated by a simple Gaussian $C(k) \approx e^{-\frac{\xi^2 k^2}{2(1-b)}}$, or Lorentzian $C(k) \approx e^{-\frac{\xi k}{2(1-b)}}$, where $b = B_0/B_{c2}$ [83, 84]. This function serves as a cutoff for the reciprocal lattice vectors at $k \approx 2\pi/\xi$ which yields a finite value for the magnetic field at the vortex cores. The term $(1-b)$ reflects the field dependence of the superconducting order parameter, which for constants B_0 and λ causes a reduction in the broadening of the field distribution with decreasing B_{c2} [85]. For our range of applied fields (0 to 6.5 T), the $(1-b)$ term is negligible in YBCO where $B_{c2} \sim 100$ T, and can be significant in PCCO where $B_{c2} \sim 9$ T [86, 87]. The magnetic field both inside and outside the superconductor is given by

$$B(\mathbf{r}) = B_0 \sum_{\mathbf{k}} F(\mathbf{k}) C(k) \cos(\mathbf{k} \cdot \mathbf{r}). \quad (1.45)$$

The magnetic field distribution, $p(B) = \langle \delta[B(\mathbf{r}) - B] \rangle$ ($\langle \dots \rangle$ denotes spatial averaging over \mathbf{r}) strongly depends on the depth z , penetration depth λ , magnetic field, and to a lesser extent on the coherence length of the

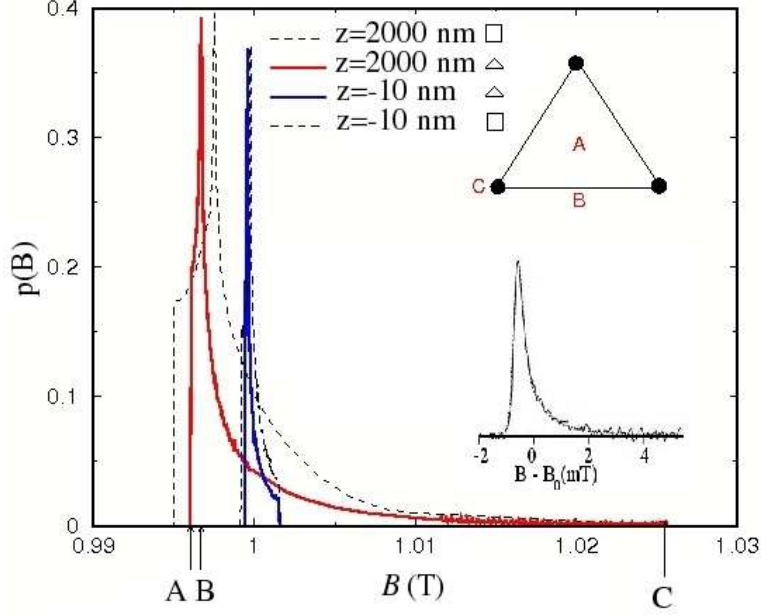


Figure 1.14: (a) Simulated field distribution using Eq. (1.45) at depths $z = 2000$ nm and $z = -10$ nm, and $B_0 = 1$ T. Parameters relevant to YBCO at $T \ll T_c$ have been used: $\lambda_{ab} = 150$ nm, $\xi = 2$ nm. A Gaussian cutoff is used where $b = 0$. Solid (dotted) lines are lineshapes of triangular (square) lattice. Top inset shows the positions of the low-field cutoff (A), most probable field (B) and high-field cutoff (C) in a triangular lattice. Bottom inset: field distribution measured in a YBCO crystal by μ SR at 0.5 T fitted by the London model convoluted with a Gaussian distribution [88].

superconductor, ξ . An example of the magnetic field distribution, $p(B)$, calculated using Eq. (1.45) is plotted in Fig. 1.14 for a triangular and square lattice with $z = 2000$ nm, and $B_0 = 1$ T, and using parameters relevant to YBCO: $\lambda = 150$ nm $\xi = 2$ nm. $p(B)$ shows four characteristics: (i) a low-field cutoff due to the minimum field at the center of a triangular formed by three vortices, (ii) a cusp corresponding to the most probable field B_{sad} between two nearest-neighbor vortices, (iii) a tail towards high field arising from regions close to the vortex cores, and (iv) a high field cutoff for the maximum field at the core of a vortex. These features are shared by the triangular and square lattices. However the lineshape in the latter is

broader due to a smaller low field cutoff, as the distance between the centre of a square lattice from each vortex is smaller than in the triangular lattice [89]. For clarity, we will limit our discussion to the triangular lattice which is more common in HTSC superconductors. An example, of a measured lineshape is shown in the inset of Fig. 1.14, which is well fitted by the London model in a triangular VL. To fit the experimental data, the theoretical $p(B)$ was smeared out by a Gaussian distribution which accounts for disorder of the VL [88].

Near the surface, $p(B)$ is strongly depth-dependent, where the broadening is drastically reduced as plotted in Fig. 1.14 at a depth $z = -10$ nm outside the superconductor. This is because the Fourier components in Eq. (1.43) outside the superconductor vary as $\exp(kz)$, where k has values always equal to or larger than $2\pi/a$. At high field, the vortex spacing in Eq. (1.38) is very small, thus the Fourier components decay on a length scale of $\frac{1}{k} \approx \frac{a}{2\pi}$. For example, at $B_0 = 1$ T, $a \approx 50$ nm, and $\frac{1}{k} \approx 7$ nm.

One can quantify the field and depth dependence of the field distribution by computing the second moment, $\sigma^2 = \langle B^2 \rangle - \langle B \rangle^2$, which takes on the form

$$\sigma^2 = B_0^2 \sum_{\mathbf{k} \neq 0} F^2(\mathbf{k}) C^2(\mathbf{k}). \quad (1.46)$$

The second moment versus z is plotted in Fig. 1.15 for various fields. The broadening outside the superconductors decays faster at high fields than low fields as the vortices are closely spaced, and the field inhomogeneity outside the superconductor is thus smaller than at low fields. Inside the superconductor, the variance recovers to the bulk limit as $\exp(\Lambda z)$, where $\Lambda^2 = k^2 + 1/\lambda^2$.

For implantation depths inside the superconductor, comparable or larger than $2\pi/k$, the field distribution is nearly field independent for $2B_{c1} \leq B_0 \leq B_{c2}$ (for $a \ll \lambda$), and the second moment of $p(B)$ follows the formula [90],

$$\sigma \approx \frac{0.0609\Phi_0}{\lambda^2(T)}, \quad (1.47)$$

neglecting the cutoff field. This can be seen in Fig. 1.16-(a), where the

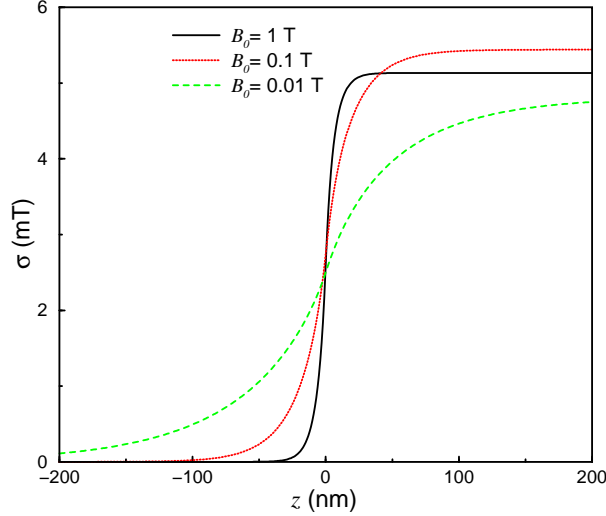


Figure 1.15: Variance of the field distribution as a function of depth, with $z > 0$ ($z < 0$) corresponding to inside (outside) the superconductor. The parameters $\lambda_{ab} = 150$ nm, $\xi = 2$ nm, and a Gaussian cutoff ($b = 0$) have been used.

variance σ is field independent for $\xi = 0$ at high fields. Using the latter makes σ field-dependent, and the correction is significant inside the superconductor. The correction, however, is smaller outside the superconductor; where the second moment is strongly field-dependent and vanishes at ~ 0.5 T for $z = -50$ nm. At this field, the field inhomogeneity goes to zero over the short distance $a/2\pi \sim 20$ nm. Thus, the field recovers to uniformity at distances higher than 20 nm away from the superconductor.

1.5.2 Disorder

Defects can pin the vortices at energetically favorable locations in the sample, where the order parameter is already suppressed. Having a vortex centered on the defect is favorable since it saves the core energy. In HTSC, the vortices are susceptible to pinning because of their short coherence lengths, and weak coupling between CuO_2 layers. Vortex pinning leads to a vortex density gradient which modifies the current density in the material. Vortex

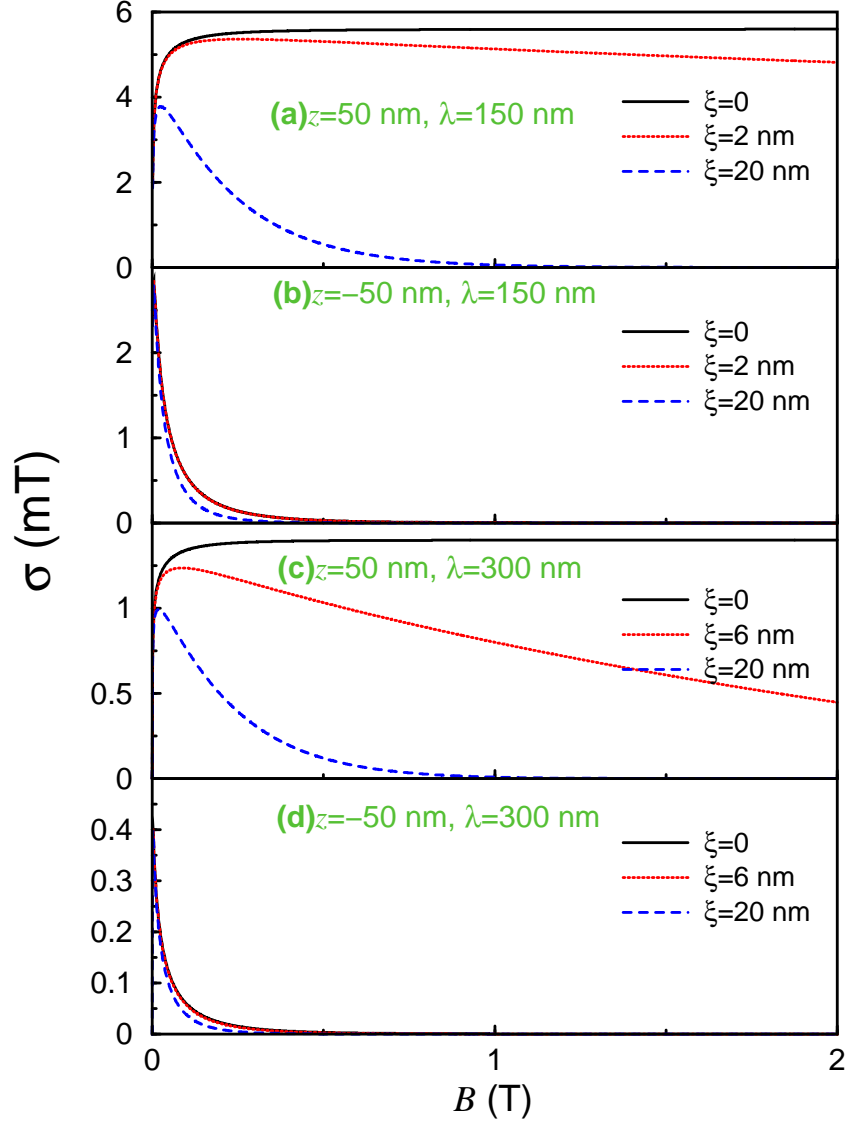


Figure 1.16: Variance of the field distribution inside the superconductor at $z = 50$ nm for (a) and (c), and outside at $z = -50$ nm for (b) and (d). Parameters relevant to YBCO (PCCO) have been used where $\lambda_{ab} = 150$ (300) nm and $\xi = 2$ (6) nm. Also, plotted is the variance for $\xi = 0, 20$ nm. A Gaussian cutoff is used in all, where $b = 0$ is taken for YBCO, and $b = B/B_{c2}$ ($B_{c2}=9$ T) is used for PCCO.

pinning also causes distortions of the regular VL and has direct implications on potential applications.

The disorder can be classified into three categories based on (i) strength: either weak and strong disorder, (ii) nature: uncorrelated point-like defects such as impurities and correlated disorder from naturally occurring grain boundaries or artificially induced columnar defects by irradiation with heavy ions. (iii) geometry: bulk disorder or surface disorder such as energy barriers and surface roughness. In cuprates, oxygen deficiencies and twin boundaries are the two leading sources of pinning. The strong pinning situation naturally appears due to the layered structure. The strength of the pinning can be easily revealed in μ SR by slightly changing the applied field and measuring the resulting change in the field distribution, especially the cusp frequency [82]. If that produces no change, then the vortices are highly pinned. This has been observed by μ SR in highly twinned YBCO samples [82]. In contrast, in conventional NbSe₂, the pinning is weak as the cusp field easily responds to a small change in the applied field [91].

The correlated disorder is dominant in orthorhombic systems such as YBCO due to the existence of twin and grain boundaries. Point-like defects from oxygen deficiencies and impurities are weak pinning centers, and may also perturb the VL. These random point-like pinning centers are more significant at low fields where the interaction energy between the vortices is weak [92]. At high magnetic fields, the vortex-vortex energy overcomes the weak random pinning centers, and only strong pinning sites will keep the vortices localized [82]. Rough surfaces can be significant in thin films or powdered samples, and can dominate the vortex structure of the bulk. Under zero field conditions, vortices cannot form spontaneously within the bulk sample but have to penetrate from the sample edge. This edge produces a barrier against vortex entry, which vanishes for fields above B_{c1} for an ideal surface. The surface barrier vanishes at the first penetration field $B_p \approx \Phi_0/4\pi\xi\lambda$. At this field, the order parameter is strongly suppressed at the surface, allowing the vortices to penetrate. Real samples, however, usually have inhomogeneities at the surface producing local field enhancements and reducing the first penetration field to a value below B_p [19].

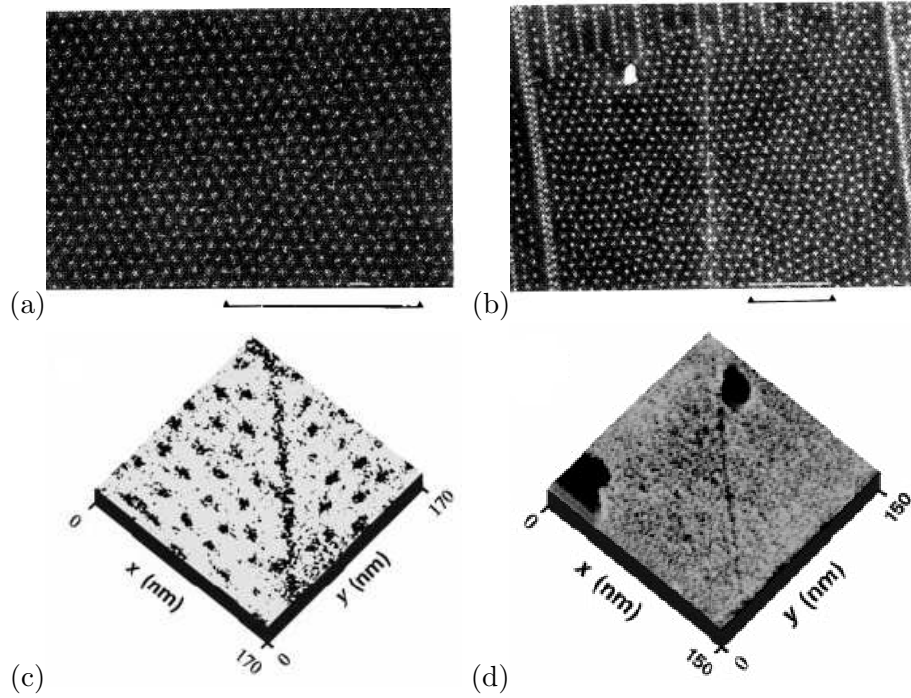


Figure 1.17: Top panel: the vortex configuration in YBCO crystals obtained using Bitter decoration technique [93]: images of (a) a twinned and (b) a twin-free area are taken after cooling in 20 G. The marker is 10 μm . Bottom panel: STM images of twinned YBCO single crystals at 4 K, with the magnetic field applied parallel to the c -axis, and perpendicular to the surface [94]. (c) Image taken after field cooling in 3 T. (d) Topographic images of the YBCO surface showing the twin boundary.

The attraction of vortices to twinning planes leads to an enhanced vortex density along the twin boundaries, as clearly observed by Bitter decoration [93] and STM [94] (see Fig. 1.17). This leads to a locally distorted VL, a large scale distorted VL, or a completely random vortex structure. The disorder of the VL due to twin boundaries and other defects strongly modifies the ideal magnetic field distribution of the VL. The latter is smeared out by the distortions and becomes more symmetric and broader [95]. For example, the second moment of randomly positioned stiff parallel vortices is proportional to the applied field [96]

$$\sigma_{\text{rand}}^2 = \frac{B_0 \Phi_0}{4\pi \lambda^2}. \quad (1.48)$$

The ratio, $\sigma_{\text{rand}}^2/\sigma^2 \approx 0.6 \ln(\kappa) B_0/B_{c1}$, is typically $\ll 1$, therefore the second moment of randomly positioned vortex lines is always larger than that of the perfect VL. This disorder in the VL is often accounted for by convoluting the ideal VL lineshape by a Gaussian of width σ_D , which is thus a quantitative measure of the disorder. Such disorder smears out the Van Hove singularities of $p(B)$ and renders the lineshape symmetric when $\sigma_D \geq \sigma$. So, the width of the field distribution increases from the theoretical second moment σ to a width dominated by σ_D [97].

1.5.3 Anisotropy and Thermal Fluctuations

All cuprate superconductors consist of superconducting CuO_2 planes of spacing d which interact with each other by weak Josephson coupling. The layered structure causes two novel phenomena: pancake and Josephson vortices. When the magnetic field is applied along the c -axis, 2D point vortices; which have a zero order parameter only in one layer, are established inside the material. Point vortices in the same layer repel each other, and those in different layers attract each other to form pancake vortices, with the lowest energy achieved when straight line vortices are formed. The field of a single point vortex with centre at $\mathbf{r}_i = 0$ is confined to a layer of thickness $2\lambda_{ab}$,

1.5. Vortex Lattice in HTSC

where the z and in-plane components take on the form [98]

$$B_z(\mathbf{r}) = (s\Phi_0/4\pi\lambda_{ab}^2 r)e^{-r/\lambda_{ab}} \quad (1.49)$$

$$B_\perp(\mathbf{r}) = (s\Phi_0 z/4\pi\lambda_{ab}^2 r_\perp)[e^{-|z|/\lambda_{ab}}/|z| - e^{-r/\lambda_{ab}}/r], \quad (1.50)$$

where s is the CuO_2 layer spacing. For a straight vortex line, the in-plane component of the point-vortex fields (if $s \ll \lambda$) cancel; and only the z -component survives. The flux of a point-vortex in the plane $z = z_n$ is $\phi(z_n) = (s\Phi_0/2\lambda_{ab}) \exp(-|z_n|/\lambda_{ab}) \ll \Phi_0$, with the sum of the flux at all points along a stack yields Φ_0 . When the applied field is along the ab -plane, the vortex core prefers to run between the CuO_2 layers, and these vortices are called Josephson vortices. The width of Josephson core is $\lambda_J = \gamma s$ and its thickness is s .

HTSC are characterized by two magnetic penetration depths for currents in the ab -plane λ_{ab} ,² and along the c -axis λ_c , and by two coherence lengths ξ_{ab} and ξ_c . The anisotropy ratio $\gamma = \lambda_c/\lambda_{ab} = \xi_{ab}/\xi_c$, is $\gamma \approx 5$ in YBCO, $\gamma \approx 25$ in PCCO, and $\gamma > 125$ in BSSCO [99]. For fields applied parallel to the c -axis, the Josephson length $\lambda_J = \gamma s$ determines how effective is the tunneling of currents between the superconducting planes in connecting the point-vortex flux. The ratio λ_J/λ_{ab} determines the dimensionality of the vortex configuration. In optimally doped YBCO, $\lambda_J/\lambda_{ab} \ll 1$, thus the vortices are straight lines, and have a 3D vortex configuration over most of the field-temperature phase diagram; similar to isotropic superconductors. This justifies the use of the London model to study the magnetic field of the vortex state. In contrast, for optimally doped BSSCO and underdoped YBCO, $\lambda_J/\lambda_{ab} \geq 1$, and the coupling between point-vortices in adjacent CuO_2 planes is very weak [98]. As a result, the flux structure may consist of pancake vortices which may couple at low fields via Josephson and magnetic interactions to form straight vortices.

The field distribution of a 2D VL structure has different features than the 3D structure discussed earlier. For a 2D VL, the field variance σ given

²A small anisotropy exists between the a and b direction in YBCO, where $\lambda_a \approx 1.19\lambda_b$.

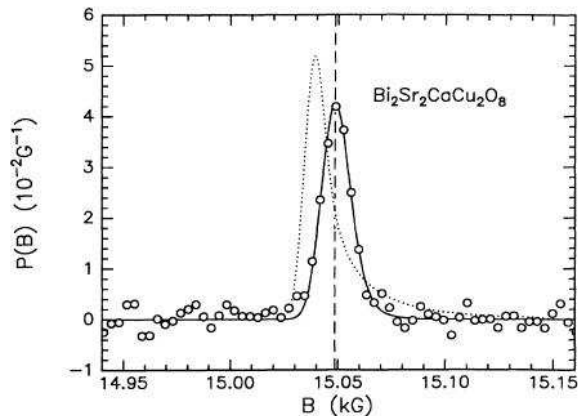


Figure 1.18: The field distribution in BSSCO crystals measured by μ SR in an external field of 1.5049 T applied along the c -axis. The measured lineshape is not well fitted by a 3D model (dashed line), and well fitted by a 2D model [13].

in Eq. (1.46) reduces to a much smaller value [90]

$$\sigma_{2D} = 1.4(s/a)^{1/2}\sigma \ll \sigma. \quad (1.51)$$

The field distribution of a 2D VL is nearly symmetric, and the cusp field is equal to the applied field [100, 101]. An example is shown in Fig. 1.18. Monte Carlo simulations have shown that $p(B)$ of a 2D structure has a low field tail rather than a high field tail in a 3D VL [100]. This was observed in μ SR measurements (Fig. 1.19-(a)) [13, 101]. In highly anisotropic BSSCO systems, μ SR studies have found evidence of a crossover from a 3D VL (positively skewed) to a 2D VL (nearly symmetric or negatively skewed) as a function of the field. When the magnetic field is increased, the interaction between point vortices within a layer will eventually exceed the interlayer electromagnetic coupling, and random pinning sites will lead to a misalignment of the pancake vortices from 3D to 2D structure. In BSSCO, where $s \sim 1.5$ nm and $\gamma \sim 150$, the crossover field is $B_{2D} \sim \Phi_0/(\gamma s)^2 \sim 40$ mT. In Ref. [101], B_{2D} was found to be ≈ 50 mT. Similar effects have been observed in a more isotropic system, LSCO [102]. The origin is, however,

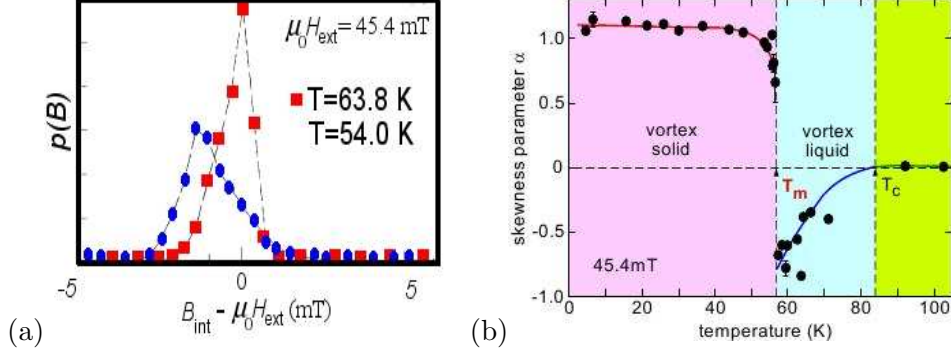


Figure 1.19: (a) The μ SR field distribution measured in low and high applied fields. The low field lineshape is that of a regular VL, but the high field is due to a melted lattice. (b) The skewness parameter $\alpha = \langle \Delta B^3 \rangle^{1/3} / \langle \Delta B^2 \rangle^{1/2}$ of the field distribution is shown [101].

due to a phase transition from a Bragg glass where the vortices have a long range order (with weak disorder), to a more disordered vortex glass of short range order.

At low temperatures, the vortices are frozen into a vortex structure. As the temperature increases, thermal fluctuations of the vortices become significant. These are more important in HTSC due to the higher values of T_c and the layered structure of these systems. Strong thermal fluctuations overcome the pinning potential and greatly reduce the effect of pinning. If the fluctuations are large, and the coupling is very weak, the VL may melt into a vortex liquid. A melting of the vortex structure was detected by μ SR in BSSCO where the field distribution changes asymmetry above $T_m \sim 58$ K, as seen in Fig. 1.19-(a) at 45.4 mT. The liquid phase above T_m resembles a 2D structure, and has a noticeable low field tail where the skewness parameter, $\alpha = \langle \Delta B^3 \rangle^{1/3} / \langle \Delta B^2 \rangle^{1/2}$ is negative (Fig. 1.19-(b)), where $\langle \Delta B^n \rangle = \int_{-\infty}^{\infty} dB (B - \langle B \rangle)^n p(B)$, is the n-th central moment of $p(B)$, and $\langle B \rangle$ is the first moment of $p(B)$.

A very useful phenomenological theory of layered superconductors is the Lawrence-Doniach (LD) theory [103], where the superconducting layers are separated by an insulating layer of thickness d . The LD model approaches

1.5. Vortex Lattice in HTSC

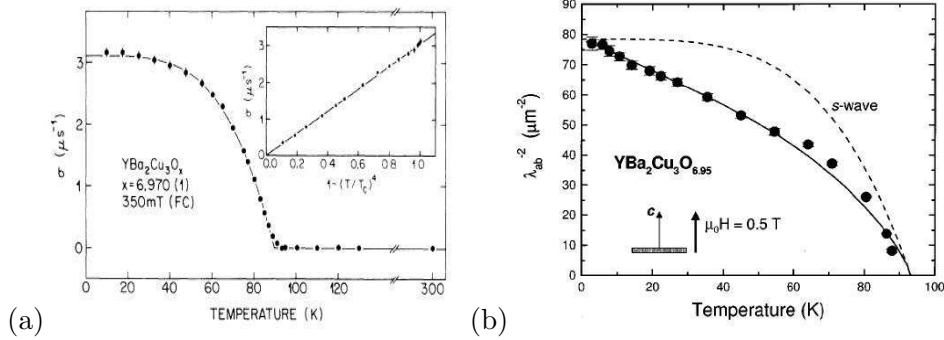


Figure 1.20: (a) T -dependence of the second moment $\sigma \propto 1/\lambda^2$ in a sintered YBCO sample measured in a field of 350 mT. The data is well fitted by the two-fluid model suggesting an s -wave pairing symmetry [104]. (b) T -dependence of $1/\lambda^2$ in a high quality YBCO single crystal in 5 kG external field. The data is well fitted by the d -wave order parameter, and strongly deviates from s -wave [105].

the anisotropic GL and London results when the c -axis coherence length $\xi_c(T)$ exceeds the layer spacing d . In this case, there is no phase difference in the order parameter between adjacent CuO_2 layers, and the VL assumes the 3D structure in the absence of pinning. When $\xi/d < \sqrt{2}$, there is a phase difference and a 2D VL takes place.

1.5.4 Temperature Dependence of λ

The temperature dependence of λ is routinely used to determine the nature of the pairing of the superconducting condensate. Experimentally, the penetration depth can be directly extracted from the second moment of the field distribution (see Eq. (1.46)). In many experiments on the VL structure in HTSC it has been difficult to determine how much of the observed structure is directly attributed to the symmetry of the pairing state and how much is due to disorder of the VL caused by extrinsic effects. Only a few experiments such as μSR , SANS, and NMR can quantitatively extract λ and ξ . Here I will only discuss the temperature dependence of the length scales from μSR , which is the most direct experiment to extract λ , and its temperature dependence [82].

The first μ SR experiments conducted on powdered and less homogeneous HTSC samples, such as YBCO, mistakenly concluded that the order parameter is of an s -wave nature (see Fig. 1.20-(a)). The second moment extracted from Gaussian fits of the field distribution showed a weak temperature dependence at low temperature consistent with BCS theory and an s -wave superconducting gap. This could be due to: (i) random orientation of the c -axis and strong pinning in the powdered and less homogeneous HTSC samples modifying the temperature dependence of the broadening from that of the penetration depth; (ii) extracting the second moment from Gaussian fits rather than fitting the data to a more realistic model (where $1/\lambda^2$ is a free parameter) that takes the features of the field distribution of the VL into account. Later, once high quality single crystals were available, it was found that the temperature dependence of the broadening resembles that of the d -wave [38]. Similar μ SR experiments on PCCO single crystals have been unable to determine the nature of pairing symmetry [106]; identified by other techniques as d -wave [107].

1.5.5 Proximal Detection of the VL

As we discussed earlier, features of the VL can be also studied outside the material. The imaging techniques such as Lorentz force, Bitter decoration, scanning tunneling microscopy, magnetic-force microscopy, are widely used to image the VL structure at the surface [108]. These techniques allowed visualization of both the VL and its distortions [108]. The imaging techniques are, however, unable to quantify the field distribution and extract λ . Contrary to this, LE- μ SR has been able to study the field distribution in a depth-resolved manner both inside and outside the superconductor [14]. Niedermayer *et al.*, measured $p(B)$ in an Ag layer of 70 nm deposited on YBCO films, and estimated a value of $\lambda = 155$ nm at 10.4 mT [109]. The measured field distribution showed features that are consistent with a regular VL inside YBCO [109].

NMR or Electron-Spin Resonance (ESR) are suitable for the determination of the flux distribution in the bulk of the sample, but no intrinsic

resonance can be measured in a HTSC sample. This is overcome by depositing spin labels onto HTSC's surface. Due to narrow intrinsic lines of usual spin labels, these methods could be useful in determining the field distribution outside the sample and therefore λ near T_c [110]. Bontemps *et al.* [111] proposed a method for determination of the spatial length scale of the field distribution to distinguish the intrinsic and extrinsic effects on the field distribution. The method is based on varying the distance of the spin labels from the superconducting surface by a suitable insulating layer. This method measured field inhomogeneities with a linewidth 30 ± 10 G, characterized by a long length scale of $7 \pm 0.1 \mu\text{m}$ in a YBCO superconducting sintered ceramic [111]. This long scale is not due to a regular VL, and the linewidth is rather attributed to the disorder of the VL inside the YBCO ceramic. Similar measurements on YBCO powders have led to a temperature dependence of λ more consistent with the two-fluid model than the d -wave symmetry [112, 113]. The above methods are, however, limited to low fields, and cannot be used at high field where the broadening of $p(B)$ outside the sample is sensitive to the disorder of the VL (see Fig. 1.16).

1.6 Thesis Outline

This thesis presents β -NMR studies of two families of superconductors, the hole-doped cuprate YBCO and electron-doped cuprate PCCO, and is organized as follows. In Chapter 2, I report the results of a new method to seek evidence of TRSB order near the surface of YBCO films. Several theories have suggested that YBCO may develop a TRSB order parameter near the surface of (110)-oriented films. The β -NMR technique is an ideal tool to test this scenario, as magnetic fields as small as 0.1 G could be detected a few nm from the surface. The field distribution is measured by implanting $^8\text{Li}^+$ ions into a silver layer (15-120 nm thick) deposited onto YBCO. The silver layer is used to stop the $^8\text{Li}^+$ ions and vary the average distance between the probe and the YBCO. In principle, one can use other metals or insulators, however, silver is preferred as it has a narrow $^8\text{Li}^+$ spin resonance which is temperature independent below 100 K at low fields, and for other

reasons as discussed in Appendix B. I will present measurements of the field distribution above and below T_c for films of (110) and (001) orientations, with the probe ions are stopping at an average distance of 8 to 40 nm from the Ag/YBCO interface with the superconductor in the Meissner state and the applied magnetic field is parallel to the surface. I will quantitatively compare these resonances and identify any changes upon cooling below T_c which could signal the existence or absence of TRSB spontaneous fields.

In Chapter 3, I will present measurements of the field distribution outside YBCO (in the vortex state) with the applied field perpendicular to the surface in an Ag overlayer evaporated onto the superconductor. This allows one to isolate the contribution from long length scale disorder of the VL, since the VL disorder that occurs on such scales cannot be probed inside the superconductor where the features of the short range ordered lattice are dominant. β -NMR studies were done on three different near-optimally doped YBCO samples: a twinned single crystal, a partially detwinned single crystal, and a 600 nm thick film. I will show measurements carried out in applied fields from 150 G to 3.33 T as a function of temperature. I will compare the field distribution in the three samples, and discuss the source of the field distribution and nature of the VL disorder.

In Chapter 4, I will present measurements of the field distribution outside PCCO in a similar fashion as done on YBCO. The studied film was highly anisotropic with 5 nm thick insulating layers of CeO₂ separating the superconducting layers. I will discuss how that affects the field distribution. I will also address the interplay between magnetism and superconductivity and compare our results to similar experiments done on PCCO using μ SR. In Chapter 5, I will draw conclusions about this work. The results in Chapters 3 and 4 have been published, and those in Chapter 2 will be submitted for publication.

Bibliography

- [1] M. Sigrist, *Prog. of Theo. Phys.* **99**, 899 (1998).
- [2] R. H. Heffner, J. O. Willis, and J. L. Smith, P. Birrer, C. Baines, F. N. Gygax, B. Hitti, E. Lippelt, H. R. Ott, A. Schenck, and D. E. MacLaughlin, *Phys. Rev. B* **40**, 806 (1989).
- [3] G. M. Luke, Y. Fudamoto, K. M. Kojima, M. I. Larkin, J. Merrin, B. Nachumi, Y. J. Uemura, Y. Maeno, Z. Q. Mao, Y. Mori, H. Nakamura, and M. Sigrist, *Nature* **394**, 558 (1998).
- [4] Y. Aoki, A. Tsuchiya, T. Kanayama, S. R. Saha, H. Sugawara, H. Sato, W. Higemoto, A. Koda, K. Ohishi, K. Nishiyama, and R. Kadono, *Phys. Rev. Lett.* **91**, 067003 (2003).
- [5] D. Conner, *Phys. Rev. Lett.* **3**, 429 (1959).
- [6] H. Ackermann, P. Heitjans, and H.-J. Stöckmann, *Top. Curr. Phys.* **31**, 291 (1983).
- [7] See the review of K. Asahi and K. Matsuta, *Nuclear Physics A* **693**, 63 (2001).
- [8] R. F. Kiefl, W. A. MacFarlane, G. D. Morris, P. Amaudruz, D. Arseneau, H. Azumi, R. Baartman, T. R. Beals, J. Behr, C. Bommas, J. H. Brewer, K. H. Chow, E. Dumont, S. R. Dunsiger, S. Daviel, L. Greene, A. Hatakeyama, R. H. Heffner, Y. Hirayama, B. Hitti, S. R. Kreitzman, C. D. P. Levy, R. I. Miller, M. Olivo, and R. Poutissou, *Physica C* **326**, 189 (2003).
- [9] J. F. Ziegler; <http://www.srim.org/>

- [10] W. Eckstein, *Computer Simulation of Ion-Solid Interactions* (Springer, Berlin, 1991).
- [11] T. J. Jackson, T. M. Riseman, E. M. Forgan, H. Glückler, T. Prokscha, E. Morenzoni, M. Pleines, Ch. Niedermayer, G. Schatz, H. Luetkens, and J. Litterst, *Phys. Rev. Lett.* **84**, 4958 (2000).
- [12] W. F. Hornyak and T. Lauritsen, *Phys. Rev.* **77**, 160 (1950).
- [13] Y.-Q. Song, W. P. Halperin, L. Tonge, T. J. Marks, M. Ledvij, V. G. Kogan, L. N. Bulaevskii, *Phys. Rev. Lett.* **70**, 3127 (1993).
- [14] E. Morenzoni, Physics and applications of low energy muons, in *Muon Science*, S. Lee *et al.* Eds., IOP Publishing (1999).
- [15] J. G. Bednorz and K. A. Müller, *Z. Phys. B* **64**, 189 (1986).
- [16] M. R. Norman and C. Pépin, *Rep. Prog. Phys.* **66**, 1574 (2003), and references there-in.
- [17] M. K. Wu, J. R. Ashburn, C. J. Torng, P. H. Hor, R. L. Meng, L. Goa, Z. J. Huang, Y. Q. Wang, and C. W. Chu, *Phys. Rev. Lett.* **58**, 908 (1987).
- [18] H. Takahashi, K. Igawa, K. Arii, Y. Kamihara, M. Hirano, H. Hosono, *Nature* **453**, 376 (2008).
- [19] K. H. Bennemann, J. B. Ketterson (*Editors*), *Superconductivity*, Springer (2008).
- [20] E. Dagotto, *Rev. Mod. Phys.* **66**, 763 (1994).
- [21] J. W. Lynn (Editor), *High Temperature superconductivity*, Springer-Verlag (1990).
- [22] G. Burns, *High Temperature superconductivity*, Academic Press Inc. (1992).

- [23] A. R. West, *Basic Solid State Chemistry*, John Wiley & Sons, 2nd edition (1999).
- [24] D. M. Ginsberg (Editor), *Physical properties of high temperature superconductors III*, World Scientific (1993).
- [25] T. Timusk and B. W. Statt, *Rep. Prog. Phys.* **62**, 61 (1999).
- [26] C. M. Varma, P. B. Littlewood, S. Schmitt-Rink, E. Abrahams, and A. E. Ruckenstein, *Phys. Rev. Lett.* **63**, 1996 (1989).
- [27] Y. Dagan, M. M. Qazilbash, and R. L. Greene, *Phys. Rev. Lett.* **94**, 187003 (2005).
- [28] J. Bardeen, L. N. Cooper, and J. R. Schrieffer, *Phys. Rev.* **108**, 1175 (1957).
- [29] F. and H. London, *Proc. Roy. Soc. A* **149**, 71 (1935).
- [30] V. L. Ginzburg and L. D. Landau, *Zh. Eksp. Teor. Fiz.* **20**, 1064 (1950).
- [31] R. F. Gasparovic and W. L. McLean, *Phys. Rev. B* **2**, 2519 (1970).
- [32] L. P. Gor'kov, *Zh. Eksp. Teor. Fiz.* **34**, 734 (1958).
- [33] M. Sgrist and K. Ueda, *Rev. Mod. Phys.* **63**, 239 (1991).
- [34] W. N. Hardy, D. A. Bonn, D. C. Morgan, R. Liang, and K. Zhang, *Phys. Rev. Lett.* **70**, 3999 (1993).
- [35] Z.-X. Shen, D. S. Dessau, B. O. Wells, D. M. King, W. E. Spicer, A. J. Arko, D. Marshall, L. W. Lombardo, A. Kapitulnik, P. Dickinson, S. Doniach, J. DiCarlo, T. Loeser, and C. H. Park, *Phys. Rev. Lett.* **70**, 1553 (1993).
- [36] J. A. Martindale, S. E. Barrett, K. E. OHara, C. P. Slichter, W. C. Lee, and D. M. Ginsberg, *Phys. Rev. B* **47**, 9155 (1993).

- [37] T. P. Devereaux, D. Einzel, B. Stadlober, R. Hackl, D. H. Leach, and J. J. Neumeier, *Phys. Rev. Lett.* **72**, 396 (1994).
- [38] J. E. Sonier, R. F. Kiefl, J. H. Brewer, D. A. Bonn, J. F. Carolan, K. H. Chow, P. Dosanjh, W. N. Hardy, Ruixing Liang, W. A. MacFarlane, P. Mendels, G. D. Morris, T. M. Riseman, and J. W. Schneider, *Rev. Mod. Phys.* **72**, 744 (1994).
- [39] T. E. Mason, G. Aeppli, S. M. Hayden, A. P. Ramirez, and H. A. Mook, *Phys. Rev. Lett.* **71**, 919 (1993).
- [40] D. A. Wollman, D. J. Van Harlingen, W. C. Lee, D. M. Ginsberg, and A. J. Leggett, *Phys. Rev. Lett.* **71**, 2134 (1993).
- [41] M. Sigrist, *Physica B* **280**, 154 (2000).
- [42] Y. Okuno, *J. Phys. Soc. Jap.* **69**, 858 (2000).
- [43] M. Sigrist, T. M. Rice, and K. Ueda, *Phys. Rev. Lett.* **63**, 1727 (1989).
- [44] M. Sigrist, D. B. Bailey, and R. B. Laughlin, *Phys. Rev. Lett.* **74**, 3249 (1995).
- [45] D. B. Bailey, M. Sigrist, and R. B. Laughlin, *Phys. Rev. B* **55**, 15239 (1997).
- [46] M. H. S. Amin, S. N. Rashkeev, M. Coury, A. N. Omelyanchouk, and A. M. Zagoskin, *Phys. Rev. B* **66**, 174515 (2002).
- [47] D. L. Feder, A. Beardsall, A. J. Berlinsky, and C. Kallin, *Phys. Rev. B* **56**, R5751 (1997).
- [48] M. Sigrist, K. Kuboki, P. A. Lee, A. J. Millis, and T. M. Rice, *Phys. Rev. B* **53**, 2835 (1996).
- [49] W. Belzig, C. Bruder, and M. Sigrist, *Phys. Rev. Lett.* **80**, 4285 (1998).
- [50] M. E. Zhitomirsky and M. B. Walker, *Phys. Rev. Lett.* **79**, 1734 (1997).
- [51] A. B. Kulkov, *Phys. Rev. B* **52**, R7002 (1995).

- [52] J. Yang and C. R. Hu, Phys. Rev. B **50**, 16766 (1994).
- [53] C. R. Hu, Phys. Rev. Lett. **72**, 1526 (1994).
- [54] J. Y. T. Wei, N. C. Yeh, D. F. Garrigus, and M. Strasik, Phys. Rev. Lett. **81**, 2542 (1998).
- [55] M. Fogelström, D. Rainer, and J. A. Sauls, Phys. Rev. Lett. **79**, 281 (1997).
- [56] M. Covington, M. Aprili, E. Paraoanu, L. H. Greene, F. Xu, J. Zhu, and C. A. Mirkin, Phys. Rev. Lett. **79**, 277 (1997).
- [57] Y. Dagan and G. Deutscher, Phys. Rev. Lett. **87**, 177004 (2001).
- [58] M. Aprili, E. Badica, and L. H. Greene, Phys. Rev. Lett. **83**, 4630 (1999).
- [59] Y. Asano and Y. Tanaka, Phys. Rev. B **65**, 64522 (2002).
- [60] S. Graser, C. Iniotakis, T. Dahm, and N. Schopohl, Phys. Rev. Lett. **93**, 247001 (2004).
- [61] C. Iniotakis, S. Graser, T. Dahm, and N. Schopohl, Phys. Rev. B **71**, 214508 (2005).
- [62] Y. Asano, Y. Tanaka, and S. Kashiwaya, Phys. Rev. B **69**, 214509 (2004).
- [63] A. V. Balatsky, Phys. Rev. Lett. **80**, 1972 (1998).
- [64] C. H. Choi and P. Muzikar, Phys. Rev. B **41**, 1812 (1990).
- [65] R. F. Kiefl, J. H. Brewer, I. Affleck, J. F. Carolan, P. Dosanjh, W. N. Hardy, T. Hsu, R. Kadono, J. R. Kempton, S. R. Kretzmann, Q. Li, A. H. O'Reilly, T. M. Riseman, P. Schleger, P. C. E. Stamp, H. Zhou, L. P. Le, G. M. Luke, B. Sternlieb, Y. J. Uemura, H. R. Hart and K. W. Lay, Phys. Rev. Lett. **64**, 2082 (1990).

- [66] J. E. Sonier, J. H. Brewer, R. F. Kiefl, R. I. Miller, G. D. Morris, C. E. Stronach, J. S. Gardner, S. R. Dunsiger, D. A. Bonn, W. N. Hardy, R. Liang, R. H. Heffner, *Science* **292**, 1692 (2001).
- [67] C. M. Varma, *Phys. Rev. Lett.* **83**, 3538 (1999).
- [68] Z. Yamani, B. W. Statt, W. A. MacFarlane, R. Liang, D. A. Bonn, and W. N. Hardy, *Phys. Rev. B* **73**, 212506 (2006).
- [69] S. Krämer and M. Mehring, *Phys. Rev. Lett.* **83**, 396 (1999).
- [70] G. J. MacDougall, A. A. Aczel, J. P. Carlo, T. Ito, J. Rodriguez, P. L. Russo, Y. J. Uemura, S. Wakimoto, and G. M. Luke, *Phys. Rev. Lett.* **101**, 017001 (2008).
- [71] Y. Dagan and G. Deutscher, *Phys. Rev. Lett.* **87**, 177004 (2001).
- [72] R. Krupke and G. Deutscher, *Phys. Rev. Lett.* **83**, 4634 (1999).
- [73] A. Sharoni, O. Mill, A. Kohen, Y. Dagan, R. Beck, and G. Deutscher, *Phys. Rev. Lett.* **65**, 134526 (2002), and references there-in.
- [74] A. Kohen, G. Leibovitch, and G. Deutscher, *Phys. Rev. Lett.* **90**, 207005 (2003).
- [75] B. Grévin, Y. Berthier, G. Collin, and P. Mendels, *Phys. Rev. Lett.* **80**, 2405 (1998).
- [76] W. Wang, M. Yamazaki, K. Lee, and I. Iguchi, *Phys. Rev. B* **60**, 4272 (1999).
- [77] N.-C. Yeh, C.-T. Chen, G. Hammerl, J. Mannhart, A. Schmehl, C. W. Schneider, R. R. Schulz, S. Tajima, K. Yoshida, D. Garrigus, and M. Strasik, *Phys. Rev. Lett.* **87**, 087003 (2001).
- [78] R. Carmi, E. Polturak, G. Koren, and A. Auerbach, *Nature* **404**, 853 (2000).

- [79] J. Mannhart, H. Hilgenkamp, B. Mayer, Ch. Gerber, J. R. Kirtley K. A. Moler, and M. Sigrist, *Phys. Rev. Lett.* **77**, 2782 (1996).
- [80] F. Tafuri and J. R. Kirtley, *Phys. Rev. B* **62**, 13934 (2000)
- [81] G. Blatter, M. V. Feigel'man, V. B. Geshkenbein, A. I. Larkin and V. M. Vinokur, *Rev. Mod. Phys.* **66**, 1125 (1994).
- [82] J. E. Sonier, J. H. Brewer, and R. F. Kiefl, *Rev. Mod. Phys.* **72**, 769 (2000).
- [83] T. M. Riseman, J. H. Brewer, K. H. Chow, W. N. Hardy, R. F. Kiefl, S. R. Kreitzman, R. Liang, W. A. MacFarlane, P. Mendels, G. D. Morris, J. Rammer, J. W. Schneider, C. Niedermayer, and S. L. Lee, *Phys. Rev. B* **52**, 10569 (1995).
- [84] Z. Salman, D. Wang, K. H. Chow, M. D. Hossain, S. Kreitzman, T. A. Keeler, C. D. P. Levy, W. A. MacFarlane, R. I. Miller, G. D. Morris, T. J. Parolin, H. Saadaoui, M. Smadella, and R. F. Kiefl, *Phys. Rev. Lett.* **98**, 167001 (2007).
- [85] A. Sidorenko, V. Smilga, and V. Fesenko, *Hyperfine Interact.* **63**, 49 (1990).
- [86] J. A. Skinta, M.-S. Kim, T. R. Lemberger, T. Greibe, and M. Naito, *Phys. Rev. Lett.* **88**, 207005 (2002).
- [87] A. F. Th. Hoekstra, R. Griessen, A. M. Testa, J. el Fattahi, M. Brinkmann, K. Westerholt, W. K. Kwok, and G. W. Crabtree, *Phys. Rev. Lett.* **80**, 4293 (1998).
- [88] J. E. Sonier, R. F. Kiefl, J. H. Brewer, D. A. Bonn, S. R. Dunsiger, W. N. Hardy, Ruixing Liang, W. A. MacFarlane, T. M. Riseman, D. R. Noakes and C. E. Stronach, *Phys. Rev. B* **55**, 11789 (1997).
- [89] E. H. Brandt, *J. Low Temp. Phys.* **73**, 355 (1988).
- [90] E. H. Brandt, *Phys. Rev. B* **37**, 2349 (1988).

- [91] J. E. Sonier, R. F. Kiefl, J. H. Brewer, J. Chakhalian, S. R. Dunsiger, W. A. MacFarlane, R. I. Miller, A. Wong, G. M. Luke, and J. W. Brill, Phys. Rev. Lett. **79**, 1742 (1997).
- [92] E. H. Brandt, J. Low Temp. Phys. **139**, 21 (2005).
- [93] G. J. Dolan, G. V. Chandrashekhar, T. R. Dinger, C. Feild, and F. Holtzberg, Phys. Rev. Lett. **62**, 827 (1989).
- [94] I. Maggio-April, C. Renner, A. Erb, E. Walker, and Ø. Fisher, Phys. Rev. B **390**, 487 (1997).
- [95] Y. M. Belousov and V. P. Smilga, Spectroscopy of High- T_c Superconductors: A Theoretical View By N. M. Plakida, page 236-292, CRC Press (2003).
- [96] E. H. Brandt, Phys. Rev. Lett. **66**, 3213 (1991).
- [97] D. R. Harshman, E. H. Brandt, A. T. Fiory, M. Inui, D. B. Mitzi, L. F. Schneemeyer and J. V. Waszczak, Phys. Rev. B **47**, 2905 (1993).
- [98] E.H. Brandt, Rep. Prog. Phys. **58**, 1465 (1995).
- [99] C. P. Poole Jr., H. A. Farach, and R. J. Creswick, *Superconductivity* 2nd edition, Academic Press (1995).
- [100] J. W. Schneider, S. Schafroth, and P. F. Meier, Phys. Rev. B **52**, 3790 (1995).
- [101] S. L. Lee, P. Zimmermann, H. Keller, M. Warden, I. M. Savi, R. Schauwecker, D. Zech, R. Cubitt, E. M. Forgan, P. H. Kes, T. W. Li, A. A. Menovsky, and Z. Tarnawski, Phys. Rev. Lett. **71**, 3862 (1993).
- [102] U. Divakar, A. J. Drew, S. L. Lee, R. Gilardi, J. Mesot, F. Y. Ogrin, D. Charalambous, E. M. Forgan, G. I. Menon, N. Momono, M. Oda, C. D. Dewhurst, and C. Baines, Phys. Rev. Lett. **92**, 237004 (2004).

- [103] W. E. Lawrence and S. Doniach, *Proc. 12th Intl. Conf. of Low Temperature Physics LT12* ed E Kanda, p. 361, Kyoto: Academic Press of Japan (1971).
- [104] B. Pümpin, H. Keller, W. Kündig, W. Odermatt, I. M. Savić, J. W. Schneider, H. Simmler, and P. Zimmermann, E. Kaldis and S. Rusiecki, Y. Maeno and C. Rossel, *Phys. Rev. B* **42**, 8019 (1990).
- [105] J. E. Sonier, J. H. Brewer, R. F. Kiefl, G. D. Morris, R. I. Miller, D. A. Bonn, J. Chakhalian, R. H. Heffner, W. N. Hardy, and R. Liang, *Phys. Rev. Lett.* **83**, 4156 (1999).
- [106] J. E. Sonier, K. F. Poon, G. M. Luke, P. Kyriakou, R. I. Miller, R. Liang, C. R. Wiebe, P. Fournier and R. L. Greene, *Phys. Rev. Lett.* **91**, 147002 (2003).
- [107] C. C. Tsuei and J. R. Kirtley, *Phys. Rev. Lett.* **86**, 1126 (2001).
- [108] S. J. Bending, *Advances in Physics* **48**, 449 (1999).
- [109] Ch. Niedermayer, E. M. Forgan, H. Glückler, A. Hofer, E. Morenzoni, M. Pleines, T. Prokscha, T. M. Riseman, M. Birke, T. J. Jackson, J. Litterst, M. W. Long, H. Luetkens, A. Schatz, and G. Schatz, *Phys. Rev. Lett.* **83**, 3932 (1999).
- [110] M. Požek, H. U. Habermeier, A. Maier, and M. Mehring, *Physica C* **269**, 61 (1996).
- [111] N. Bontemps, D. Davidov, P. Monod, and R. Even, *Phys. Rev. B* **43**, 11512 (1991).
- [112] A. Steegmans, R. Provoost, R. E. Silverans, and V. V. Moshchalkov, *Physica C* **302**, 159 (1998).
- [113] A. Steegmans, R. Provoost, V. V. Moshchalkov, H. Frank, G. Güntherodt, and R. E. Silverans, *Physica C* **259**, 245 (1996).

Chapter 2

Search for Broken Time-Reversal Symmetry Near the Surface of (110) and (001) $\text{YBa}_2\text{Cu}_3\text{O}_{7-\delta}$ Films

2.1 Introduction

In addition to the broken electromagnetic gauge symmetry common to all superconductors (SC), the SC order may break other symmetries [1]. A particularly interesting case occurs when the order parameter (OP) is complex, breaking time-reversal symmetry (TRS),¹ e.g. analogous to the order of superfluid $^3\text{He-A}$ [2]. A characteristic feature of TRS-breaking (TRSB) superconductors is spontaneous magnetization; however, Meissner screening cancels this in the bulk, limiting the associated fields to within the magnetic penetration depth from defects and interfaces [3]. The magnetic signatures of TRSB superconductivity are thus very subtle, and few techniques are sufficiently sensitive to detect them. To observe the magnetic fields directly, one requires a sensitive local magnetic probe, such as the positive muon in μSR ,

¹A version of this chapter will be submitted for publication. H. Saadaoui, G.D. Morris, K.H. Chow, M.D. Hossain, C.D.P. Levy, T.J. Parolin, M.R. Pearson, Z. Salman, M. Smadella, Q. Song, D. Wang, P.J. Hentges, L.H. Greene, R.F. Kiefl, and W.A. MacFarlane. Search for broken time-reversal symmetry near the surface of $\text{YBa}_2\text{Cu}_3\text{O}$ films using β -detected NMR.

2.1. Introduction

which has found evidence of TRSB superconductivity in several systems, notably Sr_2RuO_4 [5]. In this chapter we use a novel technique based on beta-detected nuclear magnetic resonance (β -NMR) to seek evidence for TRSB order near the surface of the high- T_c cuprate superconductor $\text{YBa}_2\text{Cu}_3\text{O}_{7-\delta}$ (YBCO).

In the high- T_c cuprates in general, and YBCO in particular, there is no evidence for TRSB in the bulk [6, 7] and OP-phase-sensitive measurements have established spin-singlet $d_{x^2-y^2}$ -wave order [8], but there are also indications of weak magnetism [9, 10], some of it related to the CuO chains in YBCO [11], or to vortex cores above the lower critical field [12]. Such results have motivated new theories, e.g. for a TRSB pseudogap state above the superconducting T_c [13].

Interface scattering of the d -wave Cooper pairs may also stabilize TRSB superconductivity [3]. Scattering from most interfaces perpendicular to the CuO_2 planes frustrates $d_{x^2-y^2}$ -wave order within a few coherence lengths of the interface, leaving a high density of mobile holes (as evidenced by the zero bias conductance peak (ZBCP) found in many tunneling measurements) that may condense into a superfluid of different symmetry than the bulk [14], e.g. s -wave, or TRSB states such as $d_{x^2-y^2}+is$ and $d_{x^2-y^2}+id_{xy}$ [15]. Experiments to detect TRSB near surfaces have yielded controversial results. Carmi *et al.* measured a weak spontaneous magnetic field using SQUID magnetometry near the edges of epitaxial c -oriented YBCO thin films below T_c [16], while Tafuri and co-workers detected fractional vortices in c -axis films using scanning SQUID microscopy [17]. Spontaneous magnetic flux was also measured near asymmetric 45° grain boundaries in c -axis YBCO films in zero field by Mannhart *et al.* [18]. Magnetism is also apparent in some tunneling measurements, as a spontaneous Zeeman-like splitting of the ZBCP. Some tunneling experiments have found such a splitting [19], and others did not [20], while phase sensitive measurements showed no evidence for such a TRSB state [21]. This diversity of results calls for more studies of interface magnetism in cuprates using a sensitive local magnetic probe that can locate the origin and distribution of such fields on the atomic scale.

In this chapter, we present measurements of the magnetic field near

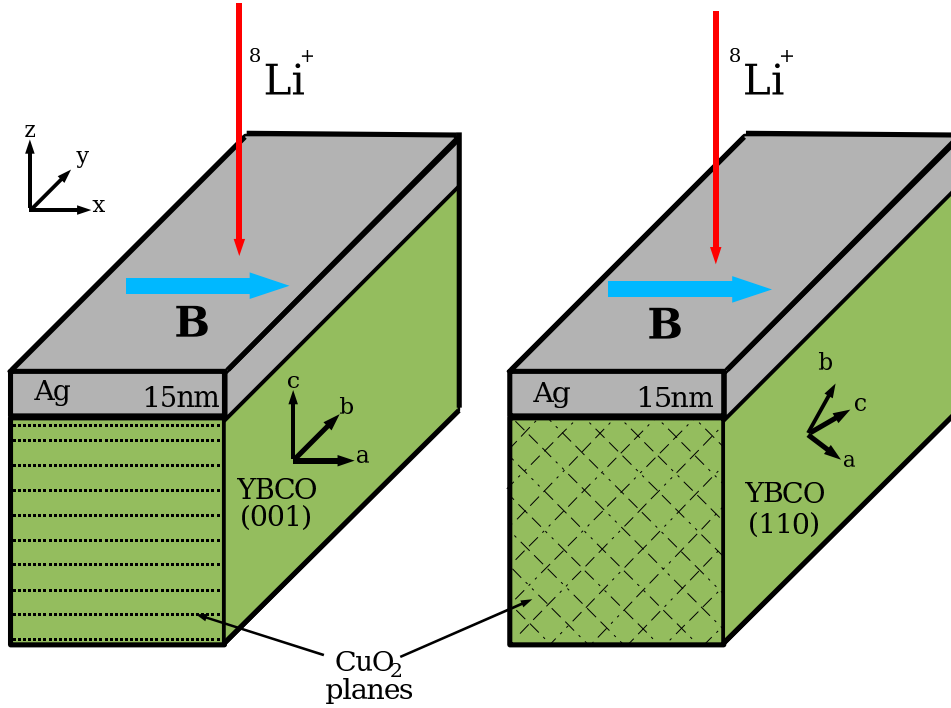


Figure 2.1: Geometry of the experiment where the field is applied along the surface. The orientation of the YBCO films is shown: Ag/YBCO(110) on the right and Ag/YBCO(001) on the left.

the interface of silver and (110)- and (001)-oriented YBCO films using β -NMR. We measure the field distribution using a highly spin polarized ${}^8\text{Li}^+$ beam implanted into a thin silver overlayer deposited on the YBCO. We find an inhomogeneous broadening of the field distribution below T_c for both orientations, with the probe ions stopping at an average distance of 8 nm from the Ag/YBCO interface. However, the magnitude of these fields is small (~ 0.2 G), and seems to originate from inhomogeneous flux penetration near the interface rather than TRSB order.

2.2 Experimental Details

The experiment was performed using β -NMR of highly-spin-polarized ${}^8\text{Li}^+$ at the ISAC facility at TRIUMF in Vancouver, Canada. For details, see Section 1.1 and Refs. [23, 24, 25]. Similar to NMR, to measure the spin resonance signal, we apply a field along the spin polarization (here in the plane of the films, see Fig. 2.1)) $\mathbf{B}_0 = B_0 \hat{y}$ (with $5 \leq B_0 \leq 150$ G), and follow the polarization of ${}^8\text{Li}^+$ as a function of the frequency ω of a small transverse radio-frequency (RF) field of amplitude $B_1 \sim 1$ G, applied along the \hat{x} -axis. The resonance condition is $\omega = \gamma B_0$, where for ${}^8\text{Li}^+$ $\gamma = 0.63015$ kHz/G. At this ω , the polarization, initially parallel to the \hat{y} -axis, is averaged by precession in the oscillating field. The resulting resonance lineshape is generally broadened by any inhomogeneity in the local magnetic field. In the absence of other effects, the lineshape thus offers a detailed measurement of the distribution of local magnetic fields in the sampled volume determined by the beam-spot (~ 2 mm in diameter) and the implantation profile (see below).

A novel pulsed RF mode was used in this study. The RF field is applied in 90° pulses randomized in frequency order, instead of the continuous wave (cw) mode commonly used [24]. In pulsed RF, the polarization at each frequency is measured three times: before, during, and after the RF pulse, and the signal is the step in polarization caused by the short RF pulse. In this way, one obtains a high signal to noise with minimal contribution from both variations in the incoming ${}^8\text{Li}^+$ rate and cw power broadening. Because of the limited B_1 in the broadband tank circuit, this pulsed mode is suitable for narrow lines up to a few kHz in width. Fig. 2.2 shows the resonance spectrum at 100 K exhibiting a linewidth, i.e. half width at half maximum (HWHM), of approximately 140 Hz ~ 0.2 G. Similar cw spectra can be at least twice as broad [23], making it difficult to resolve the small additional broadening we find at low temperature. The pulsed mode also eliminates history effects of the slowly recovering off-resonance polarization. See Appendix A for more details about this mode.

Major advantages of β -NMR in detecting TRSB are the abilities (i) to

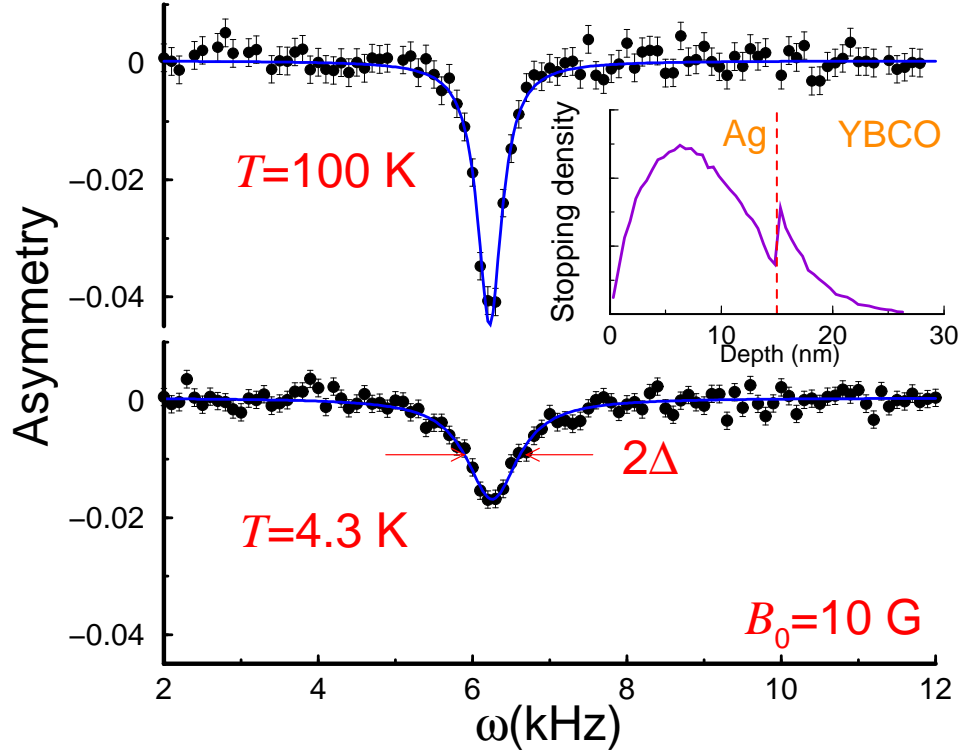


Figure 2.2: Typical β -NMR spectra in Ag taken above and below T_c at 2 keV, about 8 nm from the (110)-oriented YBCO interface, in an external field of $B_0 = 10$ G (FC) applied along the surface of the film. Solid lines are fits to a Lorentzian of amplitude A , HWHM Δ and resonance frequency ω_L , i.e. $\mathcal{L}(\omega) = \frac{A}{4(\omega - \omega_L)^2 + \Delta^2}$. Inset: simulated implantation profile for the ${}^8\text{Li}^+$ in a 15 nm Ag layer on YBCO from TRIM.SP [28]. The ${}^8\text{Li}^+$ stops at an average depth of 8 nm away from the Ag/YBCO interface.

2.2. Experimental Details

implant the probe ${}^8\text{Li}^+$ at low energy into thin layered structures and (ii) to control this implantation depth on the nanometer scale. In this study, ${}^8\text{Li}^+$ is preferentially implanted into the thin silver overlayer evaporated onto YBCO, instead of the superconductor itself. Stopping the probes in the overlayer eliminates the possibility that the probe perturbs the superconductivity. Also, the ${}^8\text{Li}^+$ nucleus carries an electric quadrupole moment, so the spectrum in non-cubic YBCO is complicated by quadrupole splittings [23]. In contrast, ${}^8\text{Li}^+$ in Ag, below 1 Tesla, exhibits a single narrow resonance with T -independent linewidth [24]. From basic magnetostatics, any inhomogeneous fields in the YBCO layer will decay exponentially outside the superconductor as $\exp(-\frac{2\pi}{a}z)$ where a is the length scale of the inhomogeneity in YBCO [26, 27]. Thus we can only detect such fields provided our probe-YBCO stopping distance z is $\leq \frac{a}{2\pi}$. Any magnetic field inhomogeneities arising in this way will broaden the intrinsic resonance of the Ag layer.

The measurements presented here were carried out on (110) and (001)-oriented YBCO films capped with 15 to 50 nm of Ag. The (110) film of $T_c = 86.7$ K was grown by RF magnetron sputtering on a (110) SrTiO_3 (STO) substrate measuring 8×6 mm. Three (001) films were also studied, (i) $T_c = 88.7$ K grown on a (001) STO substrate under similar conditions as the (110), (ii) the others are grown by thermal co-evaporation on 8×10 mm LaAlO_3 and have $T_c \sim 88.0$ K. The Ag (99.99% purity) was deposited ex-situ on the films at room temperature by DC sputtering in an Ar pressure of 30 mtorr at a rate of $0.5 \text{ \AA}/\text{s}$ while rotating the sample to ensure uniformity. The ${}^8\text{Li}^+$ implantation energy was varied so that the probe ions are implanted at average depths ranging from 8 to 43 nm. The inset of Fig. 2.2, shows the stopping profile of 2 keV ${}^8\text{Li}^+$ ions in 15 nm of Ag calculated using TRIM.SP [28]. Here the average probe-YBCO distance is ~ 8 nm. At 2 keV, about 20% of ${}^8\text{Li}^+$ ions stop in the YBCO, yielding no associated NMR signal due to fast spin lattice relaxation at low magnetic fields. The measurements were taken in the Meissner state by field-cooling in a small magnetic field B_0 (FC) or in zero field (ZFC). Residual magnetic fields were reduced to less than 30 mG normal to the surface (FC) or in all directions (ZFC) (see

Appendix C). To measure the resonance in Ag, an applied field (above ~ 5 G) is required, which was applied at 10 K ($\ll T_c$) in the ZFC case (see Appendix B).

2.3 Results

Fig. 2.2 shows two resonances at 100 K and 4.3 K in the Ag on the c-axis YBCO film. Above T_c , the resonances are all identical and show negligible differences in amplitude and linewidth, and are indistinguishable from those intrinsic to Ag. Below T_c , the resonance broadens, therefore reducing the amplitude. The HWHM, Δ , of a single Lorentzian fit to the data in both (110) and (001) samples is plotted in Fig. 2.3. It is nearly T -independent above T_c , consistent with the nuclear dipolar broadening in Ag, and it is the same in both samples and comparable to a control sample of an Ag grown on an insulating STO substrate under similar conditions (open circles, Fig. 2.3). Below T_c , the resonance broadens, signaling the appearance of disordered static magnetic fields from the underlying YBCO. Δ in Ag on the (110) film below T_c is larger and reaches 0.4 kHz (0.6 G) at 5 K, while the maximum width in the (001) is approximately 0.3 kHz (0.45 G). The excess broadening at low temperatures for the (110) film is about 0.25 kHz and 0.15 kHz in the (001) film.

The additional broadening below T_c is not accompanied by a resonance shift, as seen in Fig. 2.2. The resonance frequency is constant from 300 K to 5 K in all films, independent of FC or ZFC cooling. This rules out a superconducting proximity effect in the Ag layer where an induced Meissner shielding of the applied field leads to a diamagnetic resonance shift, e.g. as seen recently in Ag/Nb heterostructures [29]. Δ versus B_0 is displayed in Fig. 2.4. At 100 K, Δ is constant from 100 G to 5 G as expected. At 10 K (ZFC), Δ increases linearly with the applied field with no sign of saturation. The broadening at 10 K extrapolates to $\Delta(B = 0) \approx 0.2$ kHz in the (001) and ≈ 0.33 kHz in the (110), which are comparable to the normal state broadening $\Delta_{\text{ns}}(B = 0) \approx 0.18$ kHz. Thus, the net internal field in the superconducting state extrapolated to zero applied field is less

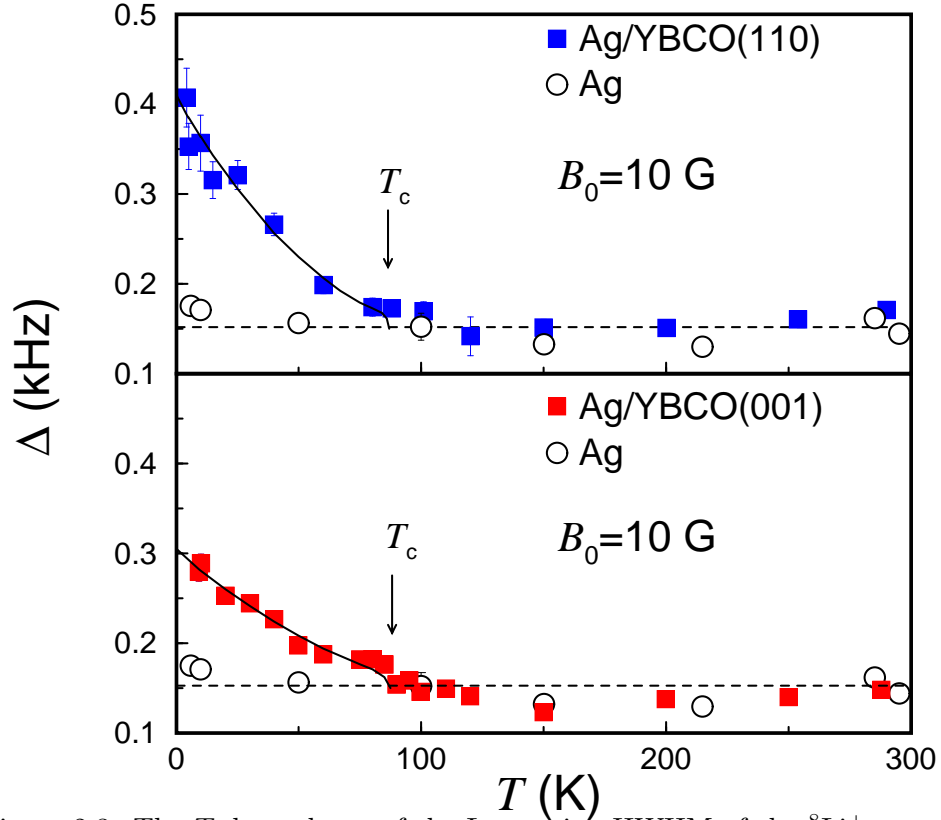


Figure 2.3: The T -dependence of the Lorentzian HWHM of the ${}^8\text{Li}^+$ resonance at 2 keV, i.e. 8 nm from the Ag/YBCO(110), Ag/YBCO(001), and Ag/STO (open circles) interface. The data on the Ag/YBCO(110) and Ag film was taken while cooling in $B_0 = 10$ G. The data on Ag/YBCO(001) was collected in $B_0 = 10$ after ZFC to 5 K. The widths were independent of field-cooling conditions. The dashed lines represent the average Ag width, the arrows point to the T_c of the YBCO films, and the solid lines are guide to the eye.

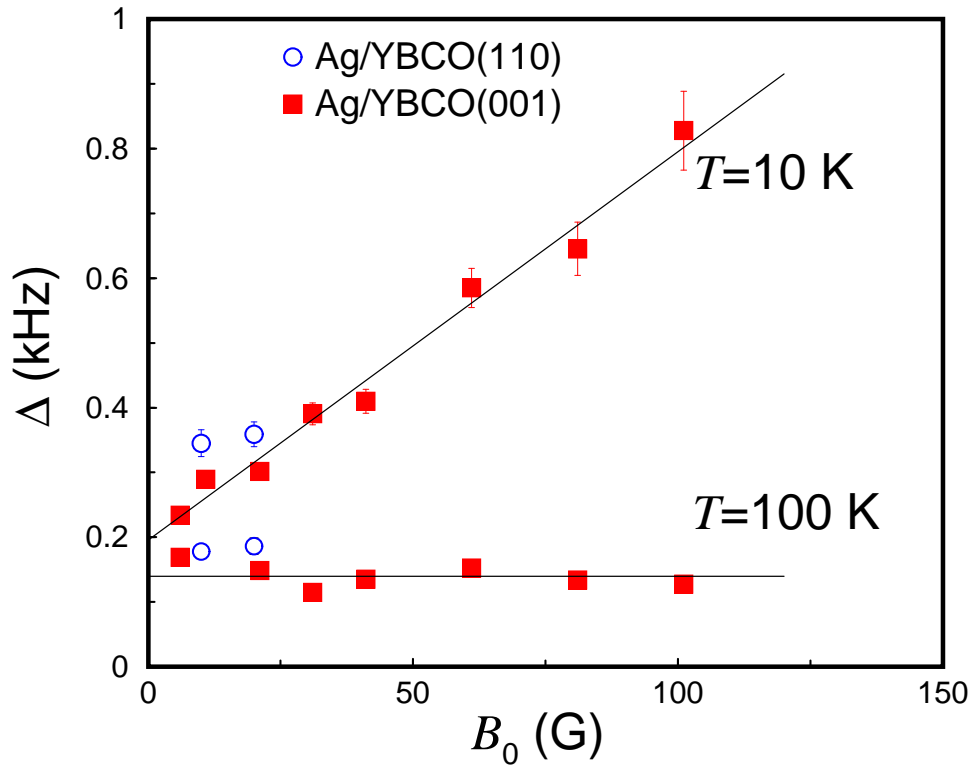


Figure 2.4: The 10 K linewidth (HWHM) of the NMR resonance versus the applied field B_0 taken in Ag on (110)- and (001)-oriented YBCO films. The data were taken after ZFC and gradually increasing the field, except in the (110) films which was FC. The solid lines are fits to the linewidth in the Ag on YBCO(001) at 10 and 100 K.

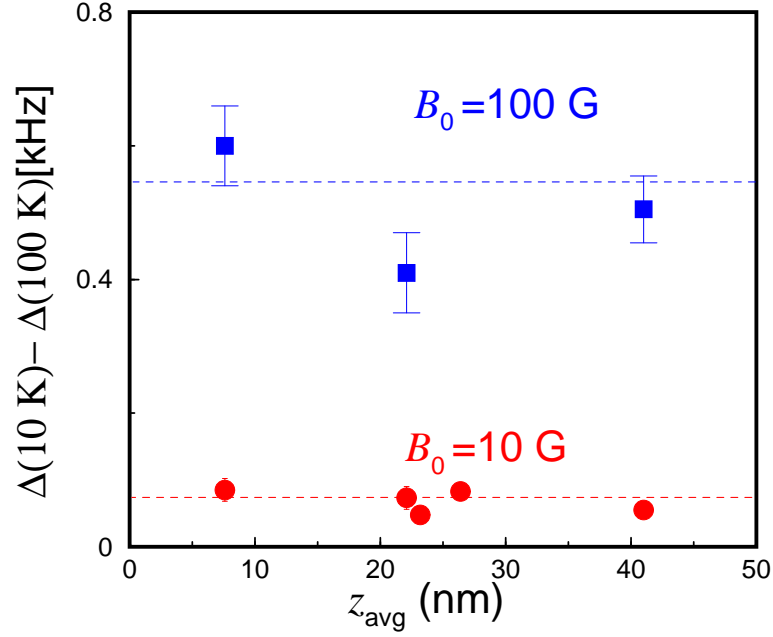


Figure 2.5: Extra broadening, $\Delta(10 \text{ K}) - \Delta(100 \text{ K})$, versus the average depth of $^8\text{Li}^+$ into a 50 nm thick Ag on (001) YBCO film, ZFC in 10 G and 100 G.

than 0.15 kHz \approx 0.2 G in both orientations. This value is partially due to the slight broadening of the Ag resonance upon cooling from 100 K to 5 K, as seen in Fig. 2.3. In addition, the broadening in Ag on the c-axis film is found to be independent of the average probe-interface distance from 8 to 43 nm as shown in Fig. 2.5, indicating that the field inhomogeneity must occur on a length scale longer than 43 nm.

2.4 Discussion and Conclusions

We turn now to discuss possible origins of the line broadening, which is clearly caused by the superconducting YBCO, since it is absent above T_c and in the Ag film (Fig. 2.3). First, it may be due to a TRSB superconducting order at the (110) interface [14]. Spontaneous fields could also arise in the c-axis films due to twin and grain boundaries [30]. The broadening we

observe here has an onset close to T_c , in contrast to tunneling measurements where the ZBCP splitting was observed only below 7 K [19]. In theory, it is also expected that TRSB order condenses at a second transition temperature $T_{c2} \ll T_c$ [3, 14, 15]. The amplitude of the inhomogeneous magnetic fields detected outside YBCO at low temperature is very small (≤ 0.2 G), and is comparable in both orientations even though the studied YBCO films have different thicknesses and surface morphology. Moreover, this internal magnetic is depth independent from 5 - 50 nm, so we expect it to have a similar magnitude at the Ag/YBCO interface. The extrapolated broadening at zero field is an estimate of the spontaneous magnetic field at the Ag/YBCO interface, and has an upper limit of 0.2 G. This is inconsistent with tunneling experiments where the spontaneous fields must be of a fraction of a Tesla [19]. The magnetic field inhomogeneity is enhanced by the applied field as reflected in the linear increase of the linewidth Δ in Fig. 2.4. The long length scale of the broadening rules out the role of impurities which could frustrate the order parameter; inducing spontaneous fields on smaller length scales of the order of few coherence lengths [31]. Because of the onset temperature at T_c , the linear-field dependence, the small magnitude of the extrapolated broadening at zero field, and long length scale of the signal, TRSB spontaneous fields are unlikely to be the origin of these internal fields.

An alternative explanation is that the broadening is due to inhomogeneous penetration of the external magnetic field in the form of flux vortices. Penetration of vortices should not occur at the fields employed here that are well-below the lower critical field H_{c1} [32], especially since the demagnetization factor for the field parallel to the thin film is very small. Moreover, surface barrier effects may even enhance the field required for vortex penetration under ZFC conditions [33]. However, at the interface the flux may penetrate more easily due to suppression of the d -wave order. Twin or grain boundaries, where the OP is already suppressed, may favor vortex nucleation [34]. Interfacial vortices have been observed in YBCO crystals in fields as small as 4 G applied parallel to the surface [35]. At such low fields, the vortex spacing, D , is of the order of few microns [36]. Outside the superconductor, the resulting field inhomogeneity leads to a broaden-

ing which would appear depth independent, since $z \ll D$, consistent with our results. This is also consistent with the T -independence of the average field (resonance frequency). The T -dependence of the linewidth in Fig. 2.3 maybe arising from an effective penetration depth λ_{eff} due to vortices inside the samples, where $\lambda_{eff}(T)$ is modified from the characteristic temperature dependence due to a d -wave order parameter by the crystal orientation and polycrystallinity of the films [37]. It is possible that such vortices could also contribute to apparent dead layer seen in HTSC and other superconductors using low-energy μ SR [38].

In summary, we have conducted a depth resolved β -NMR study of the field distribution near the interface of Ag with YBCO(001), and YBCO(110) films, where the $^8\text{Li}^+$ probes stop in the Ag. In both orientations we find additional broadening of the NMR below T_c , signaling the appearance of disordered internal static fields in YBCO. These fields are likely due to vortices penetrating at the interface *below the bulk* H_{c1} . Attributing the linear-with-field term in the line broadening to vortex penetration, we establish an upper limit on TRSB fields, from the extrapolation to zero field, of 0.2 G.

Bibliography

- [1] For reviews see L. P. Gor'kov, *Sov. Sci. Rev. A Phys.* **9**, 1 (1987); M. Sigrist and K. Ueda, *Rev. Mod. Phys.* **63**, 239(1991);
- [2] A. J. Leggett, *Rev. Mod. Phys.* **47**, 331 (1975).
- [3] M. Sigrist, *Pro. The. Phys.* **99**, 899 (1998).
- [4] J. R. Kirtley and C. C. Tsuei, *Rev. Mod. Phys.* **72**, 969 (2000); D. J. Van Harlingen, *Rev. Mod. Phys.* **67**, 515(1995).
- [5] G. M. Luke, Y. Fudamoto, K. M. Kojima, M. L. Larkin, J. Merrin, B. Nachumi, Y. J. Uemura, Y. Maeno, Z. Q. Mao, Y. Mori, H. Nakamura, and M. Sigrist, *Nature* **394**, 558 (1998);
G. M. Luke, A. Keren, L. P. Le, W. D. Wu, Y. J. Uemura, D. A. Bonn, L. Taillefer, and J. D. Garrett, *Phys. Rev. Lett.* **71**, 1466 (1993).
- [6] R. F. Kiefl, J. H. Brewer, I. Affleck, J. F. Carolan, P. Dosanjh, W. N. Hardy, T. Hsu, R. Kadono, J. R. Kempton, S. R. Kreitzman, Q. Li, A. H. O'Reilly, T. M. Riseman, P. Schleger, P. C. E. Stamp, H. Zhou, L. P. Le, G. M. Luke, B. Sternlieb, Y. J. Uemura, H. R. Hart, and K. W. Lay, *Phys. Rev. Lett.* **64**, 2082 (1990).
- [7] G. J. MacDougall, A. A. Aczel, J. P. Carlo, T. Ito, J. Rodriguez, P. L. Russo, Y. J. Uemura, S. Wakimoto, and G. M. Luke, *Phys. Rev. Lett.* **101**, 017001 (2008).
- [8] D. J. Van Harlingen, *Rev. Mod. Phys.* **67**, 515 (1995).
- [9] Jing Xia, Elizabeth Schemm, G. Deutscher, S. A. Kivelson, D. A. Bonn,

- W. N. Hardy, R. Liang, W. Siemons, G. Koster, M. M. Fejer, and A. Kapitulinik, *Phys. Rev. Lett.* **100**, 127002 (2008).
- [10] J. E. Sonier, J. H. Brewer, R. F. Kiefl, R. I. Miller, G. D. Morris, C. E. Stronach, J. S. Gardner, S. R. Dunsiger, D. A. Bonn, W. N. Hardy, R. Liang, R. H. Heffner, *Science* **292**, 1692 (2001).
- [11] Z. Yamani, B. W. Statt, W. A. MacFarlane, R. Liang, D. A. Bonn, and W. N. Hardy, *Phys. Rev. B* **73**, 212506 (2006).
- [12] J. E. Sonier, *Rep. Progr. Phys.* **70**, 1717 (2007).
- [13] C. M. Varma, *Phys. Rev. Lett.* **83**, 3538 (1999).
- [14] C. R. Hu, *Phys. Rev. Lett.* **72**, 1526 (1994);
- [15] M. Fogelström, D. Rainer, and J. A. Sauls, *Phys. Rev. Lett.* **79**, 281 (1997).
- [16] R. Carmi, E. Polturak, G. Koren, and A. Auerbach, *Nature* **404**, 853 (2000).
- [17] F. Tafuri, J. R. Kirtley, *Phys. Rev. B* **62**, 13934 (2000).
- [18] J. Mannhart, H. Hilgenkamp, B. Mayer, C. Gerber, J. R. Kirtley, K. A. Moler, and M. Sigrist, *Phys. Rev. Lett.* **77**, 2782 (1996).
- [19] M. Covington, M. Aprili, E. Paraoanu, L. H. Greene, F. Xu, J. Zhu, and C. A. Mirkin, *Phys. Rev. Lett.* **79**, 277 (1997);
- [20] For a review see G. Deutcher, *Rev. Mod. Phys.* **77**, 109 (2005).
- [21] W. K. Neils and D. J. van Harlingen, *Phys. Rev. Lett.* **88**, 047001 (2002).
- [22] Y. Okuno, *J. Phys. Soc. Jap.* **69**, 858 (2000).
- [23] R. F. Kiefl, W. A. MacFarlane, G. D. Morris, P. Amaudruz, D. Arsenneau, H. Azumi, R. Baartman, T. R. Beals, J. Behr, C. Bommas, J. H.

- Brewer, K. H. Chow, E. Dumont, S. R. Dunsiger, S. Daviel, L. Greene, A. Hatakeyama, R. H. Heffner, Y. Hirayama, B. Hitti, S. R. Kreitzman, C. D. P. Levy, R. I. Miller, M. Olivo, and R. Poutissou, *Physica C* **326**, 189 (2003).
- [24] G. D. Morris, W. A. MacFarlane, K. H. Chow, Z. Salman, D. J. Arseneau, S. Daviel, A. Hatakeyama, S. R. Kreitzman, C. D. P. Levy, R. Poutissou, R. H. Heffner, J. E. Elenewski, L. H. Greene, and R. F. Kiefl, *Phys. Rev. Lett.* **93**, 157601 (2004);
- [25] Z. Salman, E. P. Reynard, W. A. MacFarlane, K. H. Chow, J. Chakhalian, S. R. Kreitzman, S. Daviel, C. D. P. Levy, R. Poutissou, and R. F. Kiefl, *Phys. Rev. B* **70**, 104404 (2004).
- [26] M. Xu, M. D. Hossain, H. Saadaoui, T. J. Parolin, K. H. Chow, T. A. Keeler, R. F. Kiefl, G. D. Morris, Z. Salman, Q. Song, D. Wang, and W. A. MacFarlane, *J. Mag. Res.* **191**, 47 (2008).
- [27] V. G. Kogan, A. Yu. Simonov, and M. Ledvij, *Phys. Rev. B* **48**, 392 (1993); H. Bluhm, *ibid.* **76**, 144507 (2007).
- [28] W. Eckstein, *Computer Simulation of Ion-Solid Interactions* (Springer, Berlin, 1991);
- [29] E. Morenzoni *et al.*, unpublished.
- [30] W. Belzig, C. Bruder, and M. Sigrist², *Phys. Rev. Lett.* **80**, 4285 (1998); M. Sigrist, K. Kuboki, P. A. Lee, A. J. Millis, and T. M. Rice, *Phys. Rev. B* **53**, 2835 (1996);
- [31] C. H. Choi and P. Muzikar, *Phys. Rev. B* **41**, 1812 (1990); M. I. Salkola and J. R. Schrieffer, *ibid.* **58**, R5952 (1998); Y. Okuno, *J. Phys. Soc. Jap.* **69**, 858 (2000).
- [32] R. Liang, P. Dosanjh, D. A. Bonn, and W. N. Hardy, and A. J. Berlinsky, *Phys. Rev. B* **50**, 4212 (1994).

Chapter 2. Bibliography

- [33] M. Konczykowski, L. I. Burlachkov, Y. Yeshurun, and F. Holtzberg, Phys. Rev. B **43**, 13707 (1991); S. Salem-Sugui Jr., A. D. Alvarenga, O. F. Schilling, Supercons. Sci. Technol **10** 284 (1997).
- [34] R. P. Huebener, *Magnetic flux structures in superconductors*, p. 86, Springer (2001).
- [35] G. J. Dolan, Phys. Rev. Lett. **62**, 2184 (1989).
- [36] For a review see S. J Bending and M. J. W. Dodgson, Condens. Matter **17**, R955 (2005).
- [37] C. Panagopoulos, J. L. Tallon, and T. Xiang, Phys. Rev. B **59**, R6635 (1999).
- [38] A. Suter, E. Morenzoni, N. Garifianov, R. Khasanov, E. Kirk, H. Luetkens, T. Prokscha, and M. Horisberger, Phys. Rev. B **72**, 024506 (2005).

Chapter 3

Vortex Lattice Disorder in $\text{YBa}_2\text{Cu}_3\text{O}_{7-\delta}$ Probed Using β -NMR

3.1 Introduction

The vortex state of cuprate superconductors is of central importance in understanding high- T_c superconductivity (HTSC)¹. One of the most well studied quantities is the internal magnetic field distribution $p(B)$ associated with the vortex lattice (VL) [1, 2, 3, 4]. As discussed below, several methods can be used to measure $p(B)$, which depends on the London penetration depth λ , the coherence length ξ [5, 6], and, to a lesser extent, the internal structure of the vortices [7], and non-linear and non-local effects [4, 8, 9]. The form of $p(B)$ has a distinctive asymmetric shape due to the spatial magnetic inhomogeneity characteristic of an ordered two-dimensional (2D) lattice of vortices. One basic feature in $p(B)$ is a prominent high field tail associated with the vortex cores, which depends on the magnitude of ξ . There is also a saddle point in the local field profile located between two vortices. This gives rise to a Van Hove singularity or sharp peak in $p(B)$ below the average field. The overall width or second moment of $p(B)$ depends primarily on the London penetration depth λ , the lengthscale over which the magnetic field is screened. Anisotropy of the Fermi surface or the superconducting order

¹A version of this chapter has been published. H. Saadaoui, W. A. MacFarlane, Z. Salman, G. D. Morris, Q. Song, K. H. Chow, M. D. Hossain, C. D. P. Levy, A. I. Mansour, T. J. Parolin, M. R. Pearson, M. Smadella, Q. Song, D. Wang, and R. F. Kiefl, Phys. Rev. B **80**, 224503 (2009). Vortex lattice disorder in $\text{YBa}_2\text{Cu}_3\text{O}_{7-\delta}$ probed using β -NMR.

3.1. Introduction

parameter can result in a different VL but the main features are similar for any ordered lattice [10, 11].

Another general feature associated with any real VL is disorder arising from vortex pinning at structural defects and impurities [12, 13]. Structural defects are present in all superconductors to some degree, but may be more prevalent in structurally complex compounds such as YBCO. For example, YBCO's slightly orthorhombic structure facilitates crystal twinning, i.e. in a single crystal, there are generally domains with the nearly equal a and b directions interchanged. Separating such twin domains are well defined 45° grain boundaries or twin boundaries which have been shown to be effective extended vortex pinning sites [14, 15, 16, 17]. Scanning tunneling microscopy (STM) imaging of a twinned YBCO crystal show that the areal vortex density is strongly modified by the twin boundaries [18]. Small-angle neutron scattering (SANS) studies of YBCO confirm that the twin boundaries strongly deform the VL [15, 19]. Understanding the influence of such structural defects on the VL has been the subject of intense theoretical work [20, 21, 22], and is important for two main reasons. Firstly, it affects $p(B)$ and thus adds uncertainty to measurements of fundamental quantities like λ and ξ , since it can be difficult to isolate such extrinsic effects from changes in fundamental quantities of interest. Secondly, the degree of pinning of vortices determines the critical current density which is important for many applications [23].

Measurements of the vortex state field distribution $p(B)$ are most often done using SANS [15, 19], nuclear magnetic resonance (NMR) [24], and conventional muon-spin rotation (μ SR) [25]. All these methods probe the VL in the bulk and can be applied over a wide range of magnetic fields. It is also possible to probe the magnetic field distribution $p(B)$ near the surface of the sample using low energy- μ SR (LE- μ SR) in low magnetic fields [26]. Recently we have demonstrated that similar information on $p(B)$ near a surface can be obtained using β -NMR [2]. This has the advantage that it can be applied over a wide range of magnetic fields.

In this chapter, we report measurements of the VL above the surface of the cuprate superconductor $\text{YBa}_2\text{Cu}_3\text{O}_{7-\delta}$ using β -NMR [27, 28, 29, 30, 31,

32]. The $^8\text{Li}^+$ beam was implanted into a thin silver overlayer evaporated onto several YBCO samples. Measuring in the Ag allows one to isolate the contribution to $p(B)$ from *long wavelength disorder*, i.e. disorder that occurs on length scales much longer than the vortex spacing and λ , and is due to structural defects such as twin and grain boundaries. This is possible because the field distribution broadening just outside the superconductor due to the VL inside has a very distinctive field dependence. In particular it vanishes in high magnetic fields where the VL spacing becomes less than the characteristic distance of the probe from the superconductor. On the other hand, long wavelength disorder has a much weaker dependence on magnetic field and dominates the observed $p(B)$ in the high field limit. Our results show evidence for significant broadening of $p(B)$ from such long wavelength disorder on the scale of $D \approx 1 \mu\text{m}$, which is attributed to pinning at twin or other grain boundaries. The magnitude of the broadening is similar to that observed in bulk μSR measurements, suggesting that the same broadening contributes to $p(B)$ in bulk μSR measurements. There is a crossover such that near T_c , where $\lambda \gg D$, the broadening scales with the superfluid density, whereas at lower temperatures, where $\lambda \ll D$, the broadening does not track the superfluid density. We discuss the consequences of this for the inference of $\lambda(T)$ from measurements of $p(B)$ in polycrystalline superconductors.

The chapter is organized as follows: section II reviews the theory for the field distribution, and its second moment near the surface of a superconductor. Section III contains all the experimental details. In Section IV, we present the results. Finally in section V we discuss the results and draw conclusions.

3.2 The Magnetic Field Distribution $p(B)$ in the Vortex State

In a type II superconductor, above the lower critical field B_{c1} , the magnetic field penetrates the sample *inhomogeneously* forming a lattice of magnetic

3.2. The Magnetic Field Distribution $p(B)$ in the Vortex State

vortices, each carrying a flux quantum, $\Phi_0 = h/2e$. In a perfect crystal, intervortex interactions lead to a long-range ordered 2D lattice of vortices, usually of triangular (hexadic) symmetry [1]. At the core of each vortex (a cylinder of radius approximately the superconductor's coherence length ξ), the local magnetic field is maximal. Outside the core, concentric circulating supercurrents partially screen the field which thus falls exponentially with a lengthscale λ . The average magnetic field in the VL is the applied field B_0 for flat samples, where demagnetization effects are negligible [33, 34, 35]. At a given field, the average vortex spacing, i.e. the lattice constant of the VL, a is fixed. For the triangular lattice this is

$$a = \sqrt{\frac{2\Phi_0}{\sqrt{3}B_0}} \approx \frac{1546 \text{ nm}}{\sqrt{B_0(\text{mT})}}. \quad (3.1)$$

If one considers the profile of the magnetic field along a line in the lattice (perpendicular to the direction of the applied field), it is thus *corrugated* with a period determined by a . This inhomogeneity in the magnetic field causes a characteristic broadening in local magnetic resonance probes such as the muons in μSR or the host nuclei in NMR. Since the muon (or host nuclear spin) is at a well-defined lattice site(s), it samples the VL with a grid spacing given by the lattice constant of the crystal. Since this is much smaller than the VL constant, the resulting field distribution $p(B)$ provides a random sampling of the spatially inhomogeneous field $B(r)$ over the VL unit cell:

$$p(B) = \frac{1}{A} \int_A \delta[B - B(r)] dr, \quad (3.2)$$

where the integral is over a unit cell of the VL of area A . In this chapter we are concerned with the z -component of the magnetic field B_z (parallel to the c -axis of YBCO samples), and refer to it simply as B .

For an ideal triangular VL, the spatial dependence of the z -component of the magnetic field in or outside a type II superconductor follows the modified

3.2. The Magnetic Field Distribution $p(B)$ in the Vortex State

London equation,

$$-\nabla^2 B - \frac{\partial^2 B}{\partial z^2} + \frac{B}{\lambda^2} \Theta(z) = \frac{\Phi_0}{\lambda^2} \Theta(z) \sum_{\mathbf{R}} \delta(\mathbf{r} - \mathbf{R}). \quad (3.3)$$

Here $\lambda = \lambda_{ab}$ when the applied field is along the c -axis and the screening supercurrents flow in the ab plane, ∇^2 is the 2D Laplacian, $\Theta(z) = 1$ for $z > 0$ and zero otherwise, \mathbf{r} is a 2D vector in the xy plane, \mathbf{R} are the Bravais lattice vectors for the VL. We define the z axis as the normal to the surface of a superconducting slab with negative z outside the superconductor. The solution of Eq. (3.3) is easily obtained using the Fourier transform, $B(\mathbf{r}, z) = B_0 \sum_{\mathbf{k}} e^{i\mathbf{k}\cdot\mathbf{r}} F(\mathbf{k}, z)$, where the dimensionless Fourier components, $F(\mathbf{k}, z)$, are given by [36],

$$F(\mathbf{k}, z) = \frac{1}{\lambda^2} \left[\frac{\Theta(-z)e^{kz}}{\Lambda(\Lambda + k)} + \frac{\Theta(z)}{\Lambda^2} \left(1 - \frac{k}{\Lambda + k} e^{-\Lambda z} \right) \right]. \quad (3.4)$$

Here $\Lambda^2 = k^2 + \frac{1}{\lambda^2}$, and $\mathbf{k} = \frac{2\pi}{a} [n\mathbf{x} + \frac{2m-n}{\sqrt{3}}\mathbf{y}]$ are the reciprocal lattice vectors of the triangular VL, where $m, n = 0, \pm 1, \pm 2, \dots$. A cutoff function $C(k)$, approximated by a simple Gaussian $C(k) \approx e^{-\frac{\xi^2 k^2}{2}}$, can be used to account for the finite size of the vortex core, where $F(\mathbf{k}, z)$ is replaced by $F(\mathbf{k}, z)C(k)$ [2, 4]. However, the corrections due to $C(k)$ are very small in our case, so it will be omitted. An approximate solution for the magnetic field along z (both inside and outside the superconductor) is given by

$$B(\mathbf{r}, z) = B_0 \sum_{\mathbf{k}} F(\mathbf{k}, z) \cos(\mathbf{k} \cdot \mathbf{r}). \quad (3.5)$$

The second moment of $p(B)$ at a depth z , $\sigma^2 = \langle B^2 \rangle - \langle B \rangle^2$, where $\langle \dots \rangle$ is the spatial average, is given by

$$\sigma^2 = B_0^2 \sum_{\mathbf{k} \neq 0} F^2(\mathbf{k}, z). \quad (3.6)$$

The field distribution for a perfectly ordered triangular VL calculated from Eqs. (3.2) and (3.5), at $B_0 = 52$ mT and outside the superconductor

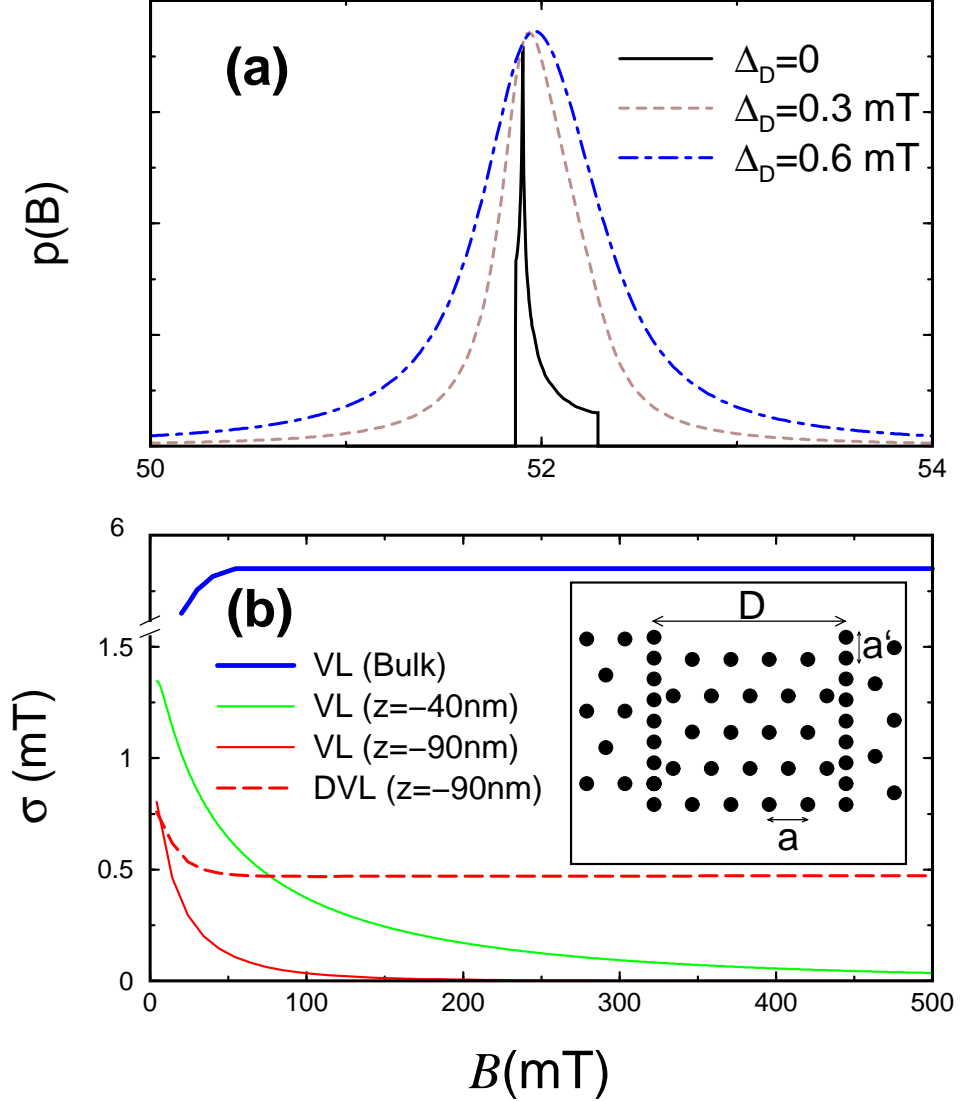


Figure 3.1: (a) Simulation of $p(B)$ in an applied field of 52 mT at a distance 90 nm from the superconductor using Eq. (3.5) convoluted with a Lorentzian of width Δ_D . (b) The broadening of $p(B)$ versus the applied field. Solid lines represent σ from Eq. (3.6) in the bulk, and 40 and 90 nm away from the superconductor. Long dashed line shows σ at 90 nm from Eq. (3.9) for $D = 4 \mu\text{m}$ and $f = 0.1$. Inset: sketch of a possible vortex arrangement including vortex trapping at twin boundaries spaced by D and a regular triangular vortex lattice elsewhere. In all figures $\lambda(0) = 150$ nm.

3.2. The Magnetic Field Distribution $p(B)$ in the Vortex State

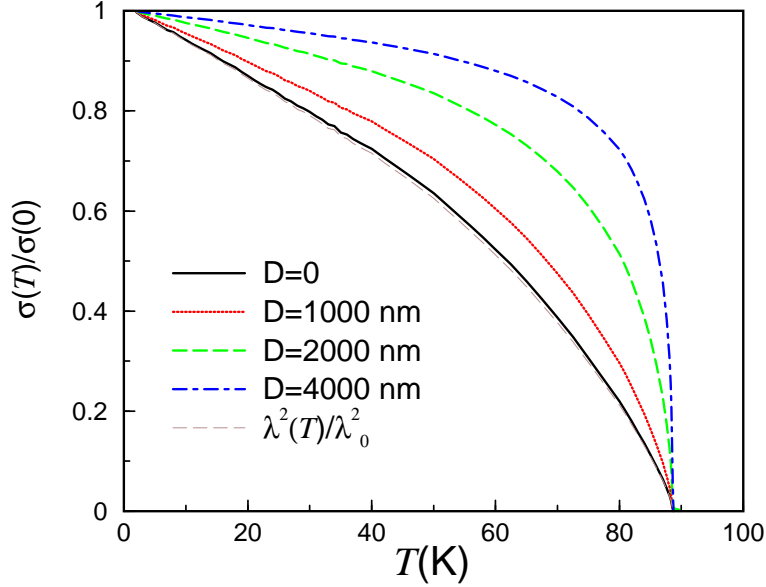


Figure 3.2: $\sigma(T)$ (normalized at $T = 0$), from Eq. (3.9) for $B_0 = 52$ mT, $z = -90$ nm, and $f = 0.1$, is plotted against T/T_c for different values of D . A d -wave temperature dependence of $\lambda(T)$ is used [37], where $\lambda(0) = 150$ nm.

at $z = -90$ nm and $\lambda = 150$ nm (relevant to YBCO at $T \ll T_c$), is presented in Fig. 3.1(a) ($\Delta_D = 0$, defined below). It shows the characteristic high field skewness with a cutoff corresponding to the field at the core of the vortices. The sharp peak corresponds to the most probable field B_{sad} at saddle points in $B(r)$ midway between adjacent vortices. The low field cutoff occurs at the center of an elementary triangle of vortices. As we move farther from the superconductor, B_{sad} moves towards the applied field as the field approaches uniformity for $z \rightarrow -\infty$, *i.e.*, $p(B) \rightarrow \delta(B - B_0)$. This crossover occurs as $\exp(\frac{2\pi}{a}z)$, as the z variation of the Fourier components $F(\mathbf{k}, z)$ in Eq. (3.4) is controlled by k which takes values equal to or larger than $2\pi/a$. However, if instead we consider a simple non-superconducting overlayer instead of free space, then the limiting $p(B)$ will be the intrinsic lineshape in the overlayer material.

As mentioned above, $p(B)$ is also affected by disorder in the VL due to

3.2. The Magnetic Field Distribution $p(B)$ in the Vortex State

pinning at structural defects in the crystal, where the superconducting order parameter is suppressed. Such disorder causes broadening of the magnetic resonance, obscuring the features expected from an ideal VL [25], adding uncertainty to parameters of interest such as λ and ξ . Relatively little is known about the detailed characteristics of this disorder. Accounting for the disorder of the VL is most often done by smearing the ideal lineshape with a Gaussian or Lorentzian distribution of width Δ_D , where the latter is a phenomenological measure of the degree of disorder [5, 38]. Calculated distributions for an applied field $B_0 = 52$ mT are shown in Fig. 3.1(a) for $\Delta_D = 0.3$ and 0.6 mT, together with the ideally ordered VL ($\Delta_D = 0$). Such disorder is more pronounced outside the superconductor and renders the lineshape symmetric when the depth dependent intrinsic VL broadening is smaller than Δ_D .

One major difference between conventional μ SR and β -NMR or LE- μ SR is the stopping range of the probe. In conventional μ SR the μ^+ stopping range is ≈ 120 mg/cm², yielding a fraction of a mm in YBCO. In contrast, in β -NMR or LE- μ SR, the mean depth of the probe can be controlled on a nm lengthscale from the surface. For implantation depths inside the superconductor, comparable or larger than λ , the μ SR lineshape (proportional to $p(B)$) is nearly field independent for $2B_{c1} \leq B_0 \leq B_{c2}$ (for $a \ll \lambda$), and the second moment of $p(B)$ follows the formula [39],

$$\sigma \approx \frac{0.00609\Phi_0}{\lambda^2(T)}, \quad (3.7)$$

neglecting the cutoff field. Using the latter makes σ slightly field-dependent, but the corrections are small for fields $B_0 \ll B_{c2}$. Outside the superconductor, the magnetic field inhomogeneity of the VL vanishes over a lengthscale that depends on the spacing between vortices, a . In particular, the recovery to a uniform field occurs on a lengthscale of $\frac{a}{2\pi}$ [31]. The field distribution is thus strongly field dependent when $a(B_0)$ is of the order of $|z|$. This is shown in Fig. 3.1(b), where σ due to the VL given in Eq. (3.6) is plotted against the applied field at a distance of 90 nm and 40 nm above the surface. In low magnetic fields, the magnetic resonance lineshape outside the

3.2. The Magnetic Field Distribution $p(B)$ in the Vortex State

superconductor is sensitive to both the intrinsic inhomogeneity of the VL as well as any additional broadening from disorder. However, in high magnetic fields the linewidth is dominated by VL disorder.

Taking the view that the dominant source of disorder is due to twin or grain boundaries [40], one can model the effect of disorder on the regular VL in different ways. The simplest is to assume that, in addition to the regular triangular lattice, a fraction of vortices is trapped along the structural defects such as twin or grain boundaries as shown in the inset of Fig. 3.1(b). The local field in real space will be the superposition of both contributions

$$\begin{aligned} B(\mathbf{r}, z) &= B^{\text{vl}}(\mathbf{r}, z) + B^{\text{dis}}(\mathbf{r}, z), \\ &= B_0^{\text{vl}} \sum_{\mathbf{k}} F(\mathbf{k}, z) e^{i\mathbf{k}\cdot\mathbf{r}} + B_0^{\text{dis}} \sum_{\mathbf{g}} F(\mathbf{g}, z) e^{i\mathbf{g}\cdot\mathbf{r}}, \end{aligned} \quad (3.8)$$

where $B^{\text{vl}}(\mathbf{r}, z)$ is the field due to the regular VL, $B^{\text{dis}}(\mathbf{r}, z)$ the field due to the vortices pinned by disorder and \mathbf{g} is some generally incommensurate wave vector related to the pinning, which for simplicity we take to be of the form $\mathbf{g} = \frac{2\pi}{a}n\mathbf{x} + \frac{2\pi}{D}m\mathbf{y}$, where a' is the spacing between vortices in a boundary, and D is the separation between boundaries as drawn in the inset of Fig. 3.1(b). The average field is then $B_0 = \sqrt{(B_0^{\text{vl}})^2 + (B_0^{\text{dis}})^2}$, where $B_0^{\text{dis}} = fB_0$ and f is the fraction of pinned vortices ($0 \leq f < 1$). The second moment of $B(\mathbf{r}, z)$ from Eq. (3.8) can be then easily calculated:

$$\sigma^2 = B_0^2 \left[(1 - f^2) \sum_{\mathbf{k} \neq 0} F^2(\mathbf{k}, z) + f^2 \sum_{\mathbf{g} \neq 0} F^2(\mathbf{g}, z) \right]. \quad (3.9)$$

It is clear from Eqs. (3.4) and (3.9), that the broadening from the VL (first term) at a distance z outside the superconductor becomes small at high magnetic fields where $|z| \gg a$. However the broadening outside the superconductor due to disorder (second term) remains large provided $|z|$ is not much larger than $\frac{D}{2\pi}$. Since D and f depend on the arrangement of twin boundaries we expect them to be sample dependent. In addition, one may also anticipate that f will decrease at high magnetic fields where the increased repulsive interaction between vortices overcomes vortex-pinning.

3.2. The Magnetic Field Distribution $p(B)$ in the Vortex State

Therefore, we assume a simplified phenomenological parameterization $f = \delta B_0^{-\gamma}$, where δ is temperature and sample dependent and $\gamma \geq 1$.

The broadening of the field distribution due to a regular VL can be significantly larger when introducing the effect of disorder due to the twin and grain boundaries. When taking the disorder into account, σ of Eq. (3.9) is no longer zero at high magnetic fields as seen in Fig. 3.1(b). This is because the broadening has a disorder component which decays on a length scale of D rather than a , where $D \gg a$ (we also assume $D \gg a'$ and thus ignore the effect of the spacing within the twin boundaries). Consequently σ shows a strong deviation from the ideal VL result as seen in Fig. 3.2 as D increases. In this case the second moment from Eq. (3.9) no longer scales with $1/\lambda^2$ as predicted for an ideal VL (see Eq. (3.7)). In particular, at low T , the broadening is almost T -independent irrespective of the superconducting gap structure. It is interesting to note that the first μ SR studies on powder samples of cuprates showed a very flat variation in the linewidth [41, 42]. This was taken as evidence for s -wave superconductivity. Later measurements on high quality crystals of $\text{YBa}_2\text{Cu}_3\text{O}_{7-\delta}$ showed a much different low temperature behaviour [43], and, in particular, a linear variation in $1/\lambda^2(T)$ consistent with d -wave pairing [44]. Although the line-shapes in powders are expected to be more symmetric than in crystals due to the additional disorder and random orientation, the different temperature dependence is surprising since it was thought that the line broadening from disorder should also scale with $1/\lambda^2(T)$ [25]. The current work provides a clear explanation for the discrepancy between powders and crystals. In powders, the line broadening is dominated by long wavelength pinning of vortices at grain boundaries. Consequently the resulting broadening at low temperature reflects variations in the vortex density and is thus only weakly dependent on temperature. In later work on crystals, the contribution from such long wavelength pinning is much less important. This is evident from bulk μ SR in crystals where one observes the expected characteristic line-shape associated with a VL [25].

3.3 Experimental Details

The measurements were carried out on three different near-optimally doped YBCO samples, two flux-grown single crystals and a thin film. I) The twinned single crystal in the form of a platelet ~ 0.5 mm thick with an area $\sim 2 \times 3$ mm² had $T_c = 92.5$ K. It was mechanically polished with 0.05 μ m alumina, then chemically etched with a dilute (0.8%) Bromine solution followed by annealing at 200° C in dry N₂ to improve the surface quality. It was then sputter coated with a 120 nm thick Ag film (99.99 % purity) at room temperature in an Ar pressure of 30 mtorr. The deposition rate was 0.5 $\text{\AA}/\text{s}$, and to ensure Ag uniformity, the crystal was rotated. II) The optimally doped detwinned single crystal had $T_c = 92.5$ K, ~ 0.5 mm thickness, and area $\sim 3 \times 3$ mm². The crystal was cleaned, annealed, and mechanically detwinned. A 120 nm thick Ag, from the same source as above, was sputtered onto the prepared surface under similar conditions. III) The film of $T_c = 87.5$ K, critical current density $J_c = 2.10^6$ A/cm³ and 600 nm thickness, supplied by THEVA (Ismaning, Germany), was grown by thermal co-evaporation on a LaAlO₃ substrate of area 9×8 mm². The film was coated *in situ* with a 60 nm silver layer (99.99% purity).

The experiments were performed using the β -NMR spectrometer at the ISAC facility in TRIUMF, Canada, where a highly nuclear-spin-polarized beam (intensity $\sim 10^6$ ions/s) of $^8\text{Li}^+$ is produced using collinear optical pumping with circularly polarized laser light [27]. The beam is directed onto the sample which is mounted on the cold finger of a He flow cryostat and positioned in the centre of a high homogeneity superconducting solenoid. The beamline and entire spectrometer are maintained in ultrahigh vacuum (10^{-10} torr). In β -NMR measurements, the $^8\text{Li}^+$ nuclear spin polarization is monitored via its asymmetric radioactive beta decay (lifetime $\tau = 1.203$ s), where the high energy (several MeV) beta electron is emitted preferentially opposite to the nuclear spin direction. The experimental asymmetry, defined as the ratio $\frac{F-B}{F+B}$ of the count rates in two plastic scintillation detectors placed in front (F) and at the back (B) of the sample, is proportional to the probe's spin polarization [27, 28].

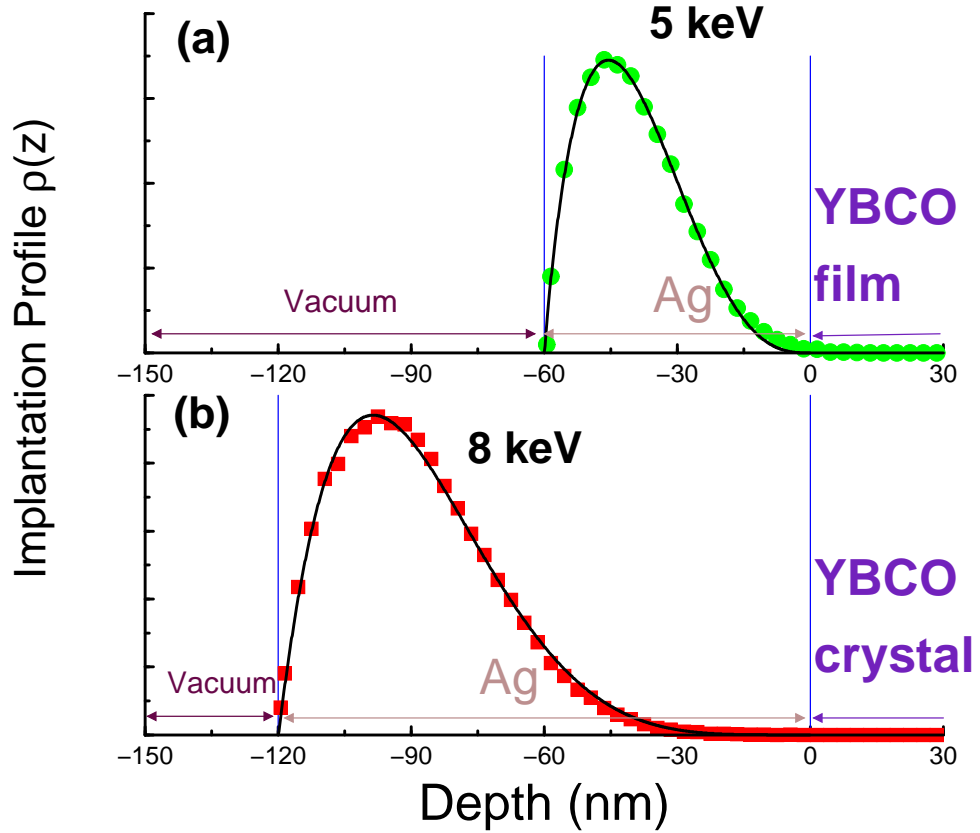


Figure 3.3: Implantation profiles of $^8\text{Li}^+$ at energies of (a) 5 keV into 60 nm of Ag with the mean at 40 nm away from YBCO film, and (b) 8 keV into 120 nm of Ag with the mean at 90 nm away from YBCO crystals, as calculated via TRIM.SP (Ref. [45]). Solid lines are phenomenological fits.

3.3. Experimental Details

The whole spectrometer can be biased at high voltage, allowing one to tune the implantation energy of ${}^8\text{Li}^+$ ions and their implantation depth between 5-200 nm. Therefore, the implanted ${}^8\text{Li}^+$ can monitor the depth dependence of the local magnetic field distribution in materials at nm scale by measuring the NMR lineshape in a manner analogous to conventional NMR [2, 28, 29]. In this work, the ${}^8\text{Li}^+$ ions are decelerated to stop in the Ag overlayer deposited on each of the three YBCO samples. Implantation profiles of ${}^8\text{Li}^+$ were calculated using the TRIM.SP code [45], examples of which are shown in Fig. 3.3. The implantation energies used in this study (8 keV in the crystal samples and 5 keV the film), were tuned to stop all the ${}^8\text{Li}^+$ within the Ag. The mean distances are 90 and 40 nm from the Ag/YBCO interface in the crystals and film, respectively.

The β -NMR measurement is carried out by monitoring the time averaged nuclear polarization through the beta decay asymmetry, as a function of the radio frequency (RF) ω of a small transverse oscillating magnetic field $\mathbf{B}_1 = B_1 \cos(\omega t)\hat{x}$, where $B_1 \sim 0.01$ mT. When ω matches the Larmor frequency $\omega_{\text{Li}} = \gamma_{\text{Li}}B_{\text{local}}$, where $\gamma_{\text{Li}} = 6.3015$ kHz/mT is the gyromagnetic ratio and B_{local} is the local field, the ${}^8\text{Li}^+$ spins precess about B_{local} , causing a loss of polarization. To establish the vortex state in the YBCO samples, they are cooled in a static magnetic field $B_0 \geq B_{c1}$ applied parallel to the c -axis of YBCO (normal to the film and platelet crystals). B_0 is also parallel to both the initial nuclear spin polarization and the beam direction. The local field sensed by the ${}^8\text{Li}^+$ is determined by the applied field and the internal magnetic field generated by the screening currents associated with the vortex lattice. Thus, B_{local} is distributed over a range of values, which can be calculated using

$$p(B) = \int_{-d}^0 dz \rho(z) \frac{1}{A} \int_A dr \delta[B - B(\mathbf{r}, z)]. \quad (3.10)$$

where $\rho(z)$ is the implantation profile calculated using TRIM.SP given in Fig. 3.3.

When ${}^8\text{Li}^+$ is implanted in Ag (with no superconducting substrate) at temperatures below 100 K, it exhibits a single narrow resonance at the Lar-

mor frequency [28]. The resonance should yield an approximately Gaussian distribution caused by nuclear dipolar moments [46]. However, continuous wave RF leads to a power-broadened Lorentzian lineshape, whose linewidth is small (~ 1 kHz ≈ 0.15 mT) and corresponds to the dipolar broadening due to the $^{107,109}\text{Ag}$ nuclear moments and RF power broadening [47]. In the presence of any additional magnetic inhomogeneity in the Ag, due for example to a VL associated with a superconducting substrate, the observed resonance lineshape will be a convolution of the narrow RF power broadened Lorentzian of Ag with the (depth dependent) field distribution due to the VL in the substrate. There are unique aspects of measuring the field distribution in the Ag overlayer compared to the superconductor itself. As mentioned above, in high magnetic fields it is possible to isolate and study the broadening due to VL disorder that occurs on a long length scale. Also in low magnetic fields, where the broadening is dominated by the VL, it should be possible to measure λ in magnetic superconductors since the field distribution above the sample is free of any internal hyperfine fields that make a bulk measurement impossible [32].

3.4 Results

The β -NMR resonances were measured as a function of temperature under field-cooled conditions at fields ranging from $B_0 = 20$ mT to 3.3 T in each one of the three samples. Fig. 3.4, shows typical resonance lineshapes at various temperatures in sample I with $B_0 = 51.7$ mT. Above T_c , the line broadening is small and temperature independent as expected from nuclear dipolar broadening. Below T_c , the field distribution in the Ag overlayer broadens dramatically from the VL in the underlying superconductor. Such broadening was observed in all samples and at all magnetic fields, although there are significant variations as a function of both magnetic field and sample as discussed below. The first thing to note is that the lineshape is very symmetric and fits well to a simple Lorentzian. This is much different from the asymmetric lineshape observed with conventional μSR in samples similar to I and II [25, 43]. The other significant difference between the

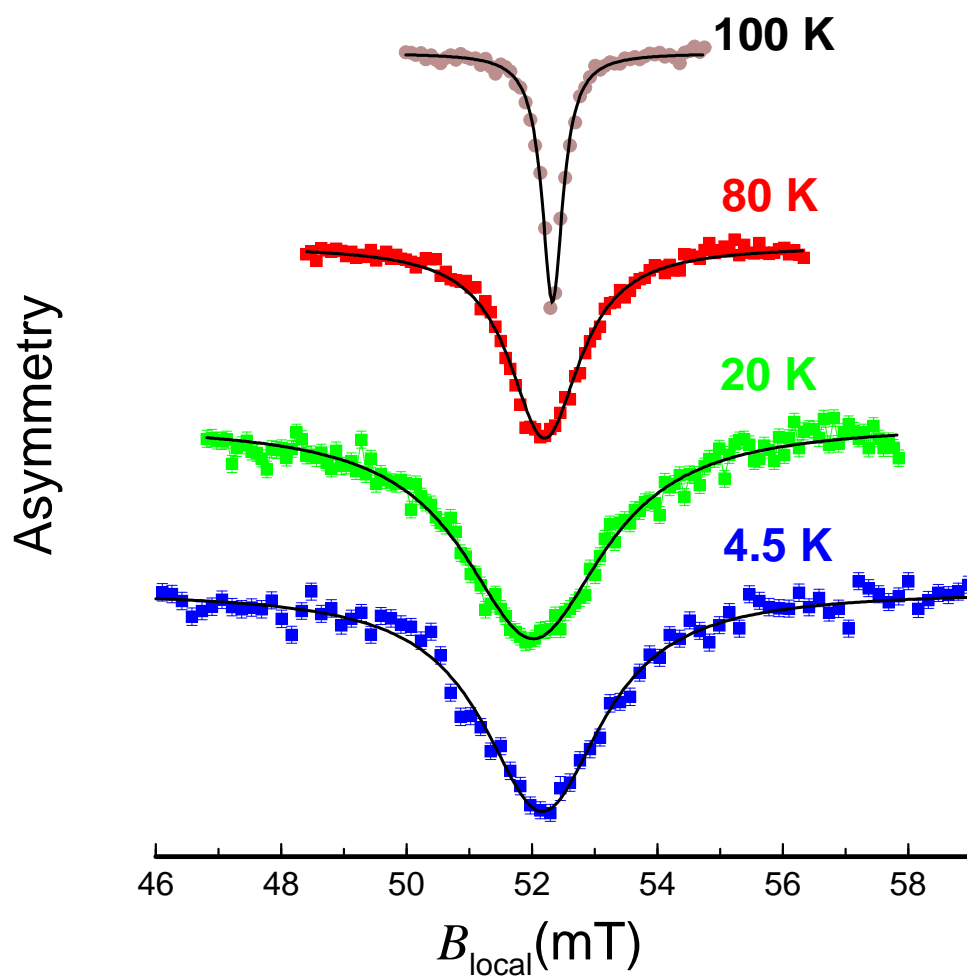


Figure 3.4: β NMR resonances in Ag/YBCO (crystal I) at temperatures 100 K, 80 K, 20 K, and 4.5 K measured in a magnetic field B_0 of 52.3 mT applied along YBCO c -axis. The solid lines are best fits using a Lorentzian.

3.4. Results

current results and previous bulk μ SR measurements [4, 9, 25, 43] on crystals is that the broadening at low temperatures is only weakly dependent on temperature, as may be seen by comparing the resonances at 20 K and 4.5 K. In contrast, the broadening from an ordered VL lattice scales with $1/\lambda^2$ and consequently in YBCO shows a strong linear T -dependence at low temperatures due to the d -wave superconducting order [43, 44].

The observed lineshape fits well to a single Lorentzian which is a convolution of two Lorentzians, one from vortices in the superconducting state with a full width at half maximum (FWHM) Δ_{sc} , and one from other sources determined from the normal state of FWHM Δ_{ns} . The width of a convolution of two Lorentzians is the sum of the individual widths: $\Delta(T) = \Delta_{\text{sc}}(T) + \Delta_{\text{ns}}$. Therefore, the contribution from vortices in the superconducting state can be obtained by simply subtracting the temperature independent normal state width. Fig. 3.5 shows the resulting $\Delta_{\text{sc}}(T)$ as one enters the superconducting state in samples I and II. At low field, the measured width (~ 2.2 mT) at low temperature is larger than expected from a regular VL and decreases significantly in the detwinned crystal to about ~ 0.6 mT. For comparison, simulations using Eq. (3.10) and the $^8\text{Li}^+$ stopping profile in Fig. 3.3(b); indicate that the broadening due to a regular VL is only $\Delta_{\text{VL}} \sim 0.3$ mT. At 3.33 T, the discrepancy between the observed width (see Fig. 3.5) and that expected from a regular VL is even more dramatic. At this high field the vortices are spaced so closely ($a \approx 27$ nm), that there should be no detectable broadening from a regular VL for our stopping depths. This can be seen clearly from the simulation in Fig. 3.1(b), where the VL broadening approaches zero at high fields. In contrast, the data at 3.33 T shows significant broadening below T_c which is therefore solely attributed to vortex disorder on a long length scale.

The temperature dependence of the broadening is also much weaker than expected from a regular VL in YBCO, where $1/\lambda^2$ has a strong linear term due to the d -wave order parameter [43, 44]. The observed temperature dependence fits well to our model of disorder, where $\Delta_{\text{sc}}(T)$ is compared to an estimate of the FWHM given by $\Delta_{\text{DVL}} \approx 2.355\sigma$, where σ is given in Eq. (3.9). This leads to an estimate of D of the order of a micron, consistent

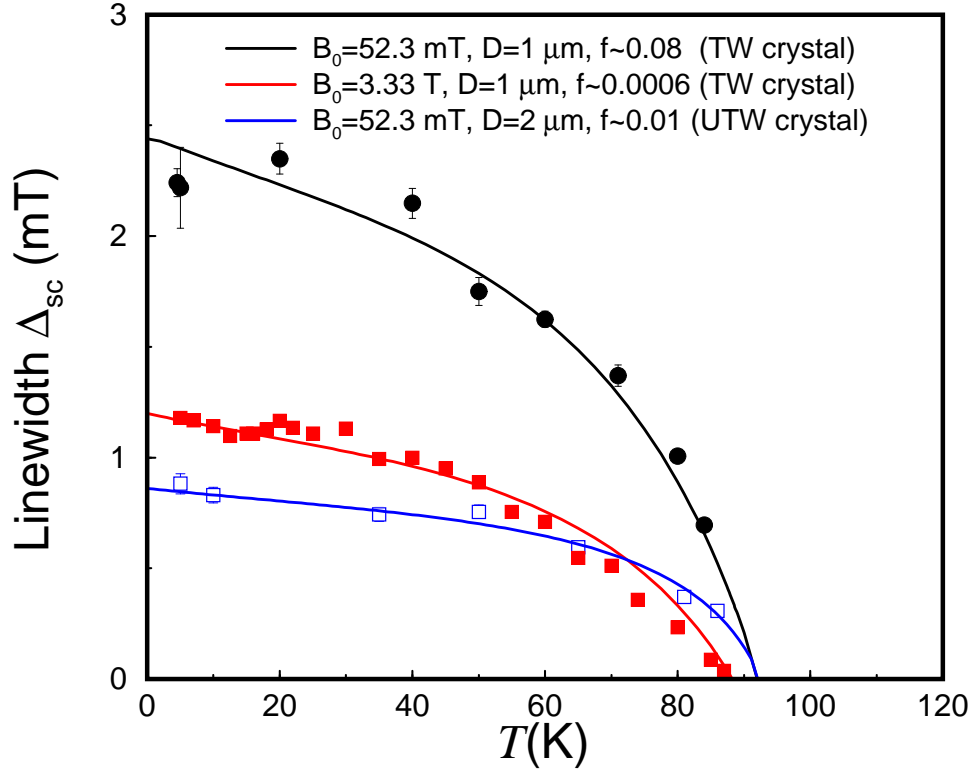


Figure 3.5: The vortex-related broadening below T_c , $\Delta_{sc}(T) = \Delta(T) - \Delta_{ns}$ of the twinned (full symbols) and detwinned (opaque squares) YBCO crystals in an applied field B_0 . $\Delta(T)$ is the linewidth at temperature T of the Lorentzian fits and Δ_{ns} is the constant linewidth in the normal state. Solid lines represent a fit using $\Delta_{DVL} = 2.355\sigma$ where σ is given in Eq. (3.9) and D and f are varied to fit the data. A d -wave temperature dependence of $\lambda(T)$ in YBCO is used, (Ref. [37]) where $\lambda(0) = 150$ nm.

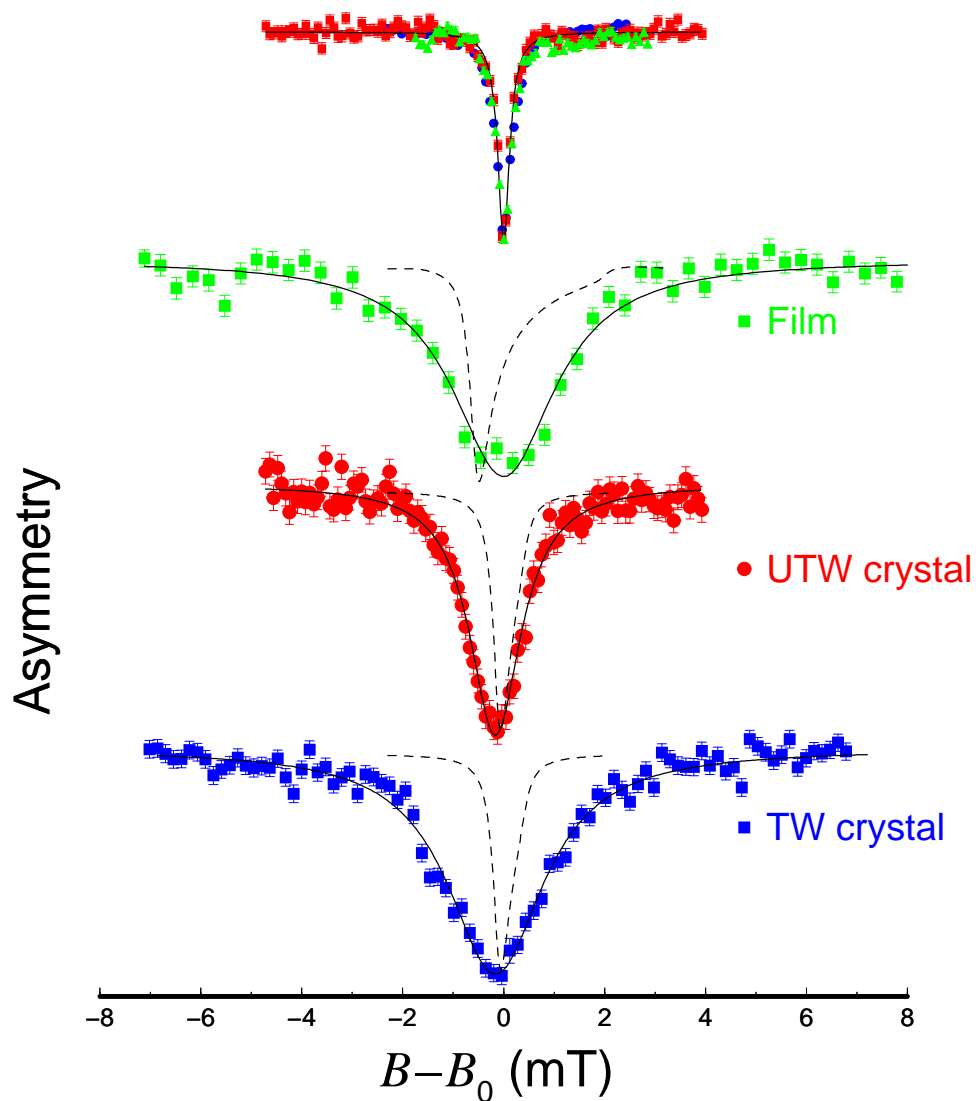


Figure 3.6: Comparison of the field distributions in the three samples taken at temperatures 100 K (top panel), 5 K (crystals) and 10 K (film). The x -axis is shifted by B_0 , the applied field which is 52.3 (51.7) mT for the crystals (film). Solid lines are Lorentzian fits and dashed lines are simulation described in the text.

3.4. Results

with the the separation between twin boundaries or grain boundaries [48]. In the detwinned crystal, D is found to be larger but not infinite since the detwinning is not complete. The fraction of vortices f pinned by structural defects in the twinned crystal is about ~ 0.1 at low field (52 mT) and decreases considerably at high field (3.33 T). Thus, the amplitude of the enhanced vortex density at the defects, fB_0 , varies between 2-4 mT at all fields. In the detwinned crystal, $f \sim 0.01$, is an order of magnitude smaller than in the twinned crystal at the same field, with small variation in the vortex density (0.5 mT) compared to the twinned crystal. These results are consistent with expectations from pinning at twin boundaries. In particular, one expects the fraction of vortices pinned will decrease in the partially detwinned crystals. Also, it is reasonable to expect that in high magnetic fields the fraction of vortices pinned will decrease due to the smaller separation between vortices, and the resulting increase in the repulsive interaction.

In Fig. 3.6, the spectra in all three samples above and below T_c are compared with the corresponding simulated field distributions. The observed lineshapes are all symmetric and significantly broader than expected, showing little or no sign of the characteristic VL field distribution. Simulation of the VL lineshape (dashed lines) was done using Eqs. (3.4), (3.5), and (3.10), for $\lambda = 150$ nm, and was convoluted with a Lorentzian representing the normal state spectra with $\Delta_{\text{ns}} = 0.3$ mT. The theoretical lineshape for the film is broader and asymmetric because it is weighted by the ${}^8\text{Li}^+$ stopping distribution which was on average closer to the superconductor. The lineshapes for the crystals are almost symmetric as the ideal VL lineshape at the depths of an average 90 nm away from the superconductor are narrower than the Lorentzian they are convoluted with. The magnetic field dependence of the superconducting linewidth $\Delta_{\text{sc}}(T)$ at low temperatures ~ 4.5 -10 K is plotted in Fig. 3.7. In all samples, we find that the broadening is largest at low field and decreases gradually with increasing field. Also, in all cases the broadening remains large and well above the prediction from a regular VL, approximated by $\Delta_{\text{VL}} \approx 2.355\sigma$, where σ of an ideal VL is given in Eq. (3.6) and weighted by the ${}^8\text{Li}^+$ profile given in Fig. 3.3. The

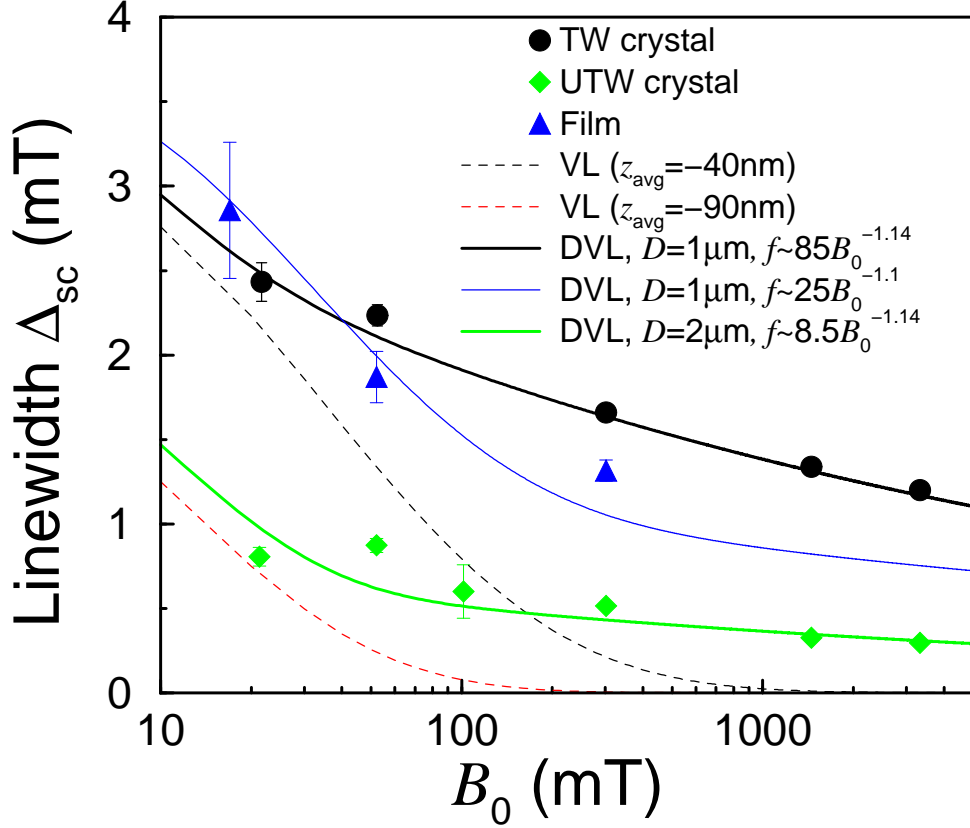


Figure 3.7: Superconducting broadening $\Delta_{sc}(T)$ of β -NMR resonance spectra at temperatures ~ 4.5 -10 K in the three samples. The experimental broadening is compared with the linewidth of an ideal VL Δ_{VL} (dashed lines), and Δ_{DVL} of a disordered VL (solid lines), which are both weighted by the ${}^8\text{Li}^+$ profile given in Fig. 3.3.

broadening is substantially smaller in the detwinned crystal compared to the other samples. One can account for all of the data using a linewidth due to a disordered VL, $\Delta_{\text{DVL}} \approx 2.355\sigma$, where σ is now given in Eq. (3.9)) and weighted by the $^8\text{Li}^+$ profile plotted in Fig. 3.3. The data is well fitted (see Fig. 3.7) by assuming that the twin/grain boundaries spacing D is sample dependent of the order of a few microns, and by assuming a phenomenological form for the fraction of pinned vortices $f = \delta B_0^{-\gamma}$ with $\gamma \sim 1.1$ and δ sample dependent.

3.5 Discussion and Conclusions

It is clear that the β -NMR lineshapes in the Ag overlayer differ substantially from that expected from a well-ordered VL field distribution. This has little to do with the method of observation. For example, in the conventional superconductor NbSe_2 , β -NMR shows the expected VL lineshape [2]. The lineshapes reported here in the YBCO film are also qualitatively different than that seen with LE- μ SR in a YBCO film coated with a 60 nm thick Ag layer [36]. In that experiment the authors found a more asymmetric lineshape in the Ag overlayer which was closer to that of a regular VL. Some of this difference may be due to the different pinning characteristics of the samples, although the YBCO film used by Niedermayer *et al.* was from the same source as sample III. Also, the LE- μ SR experiment was probing the VL closer to the interface and in a lower applied field where the disorder is less important compared to the contribution from the ordered VL. The symmetry and large broadening of the lineshape at low fields cannot be accounted for by VL melting (at a reentrant vortex liquid state near B_{c1}) which would instead yield a motional narrowing of the field distribution [49].

The observed resonances in the current experiment are dominated by long range variations of the vortex density across the face of the sample [18]. Such disorder in the VL can produce a symmetric lineshape [38, 50], and can broaden the field distribution significantly compared to that of the corresponding ordered state [51], Weak random pinning or point-like disorder due to oxygen deficiency may slightly distort the VL, and may also

broaden the lineshape [39]. However, the correlated disorder due to the twin and grain boundaries is dominant at long wavelengths [40, 52], and therefore we are mostly sensitive to the twin/grain boundaries. Indeed, the position of the probe outside the superconductor enhances its sensitivity to long wavelength disorder, as the proximal fields fall off with distance as $\exp(-2\pi|z|/D)$ where D is the wavelength of the inhomogeneity of the field [53]. The broadening is reduced in a detwinned crystal where the twin boundaries are more sparse as shown in Fig. 3.6, thus the vortex density variation across the face of the sample is smaller than in the twinned crystals as f is largely reduced.

The extrinsic broadening due to disorder at low temperature, $\Delta_D = \Delta_{sc} - \Delta_{VL}$, reported here is between 0.5 mT and 2.5 mT. This is remarkably close to the additional Gaussian broadening required to explain lineshapes in bulk μ SR measurements on crystals [25, 38, 54]. In the bulk, this extrinsic broadening is small compared to the intrinsic VL broadening, whereas outside the sample the reverse is true. It is important to note the T -dependence of the extrinsic broadening in Fig. 3.5 *does not follow the superfluid density* ($\propto 1/\lambda^2$) which varies linearly at low- T because of the d -wave order parameter [44, 55]. Instead, we observe a much weaker T -dependence. This is expected from our model of disorder which occurs on a long length scale D . For example, at low- T where λ is short compared to D , the flux density outside the sample is determined solely by inhomogeneities in the vortex density, and is independent of the superfluid density as the vortices are static and well-pinned in the twin boundaries. The current results may also explain early μ SR work on HTSC powders and sintered samples which mistakenly indicated an s -wave T -dependence of $1/\lambda^2$ [41, 42]. It is likely in these cases the linewidth was dominated by extrinsic VL disorder on a long length scale. This tends to flatten the T -dependence of the linewidth and the effective λ obtained from the analysis [41, 56]. Therefore we conclude that although the linewidth obtained from powders can be useful in making rough estimates of λ , one cannot extract accurate measurements of λ or its T -dependence without additional information about the source of broadening and in particular VL disorder.

3.5. Discussion and Conclusions

In conclusion, we have measured the magnetic field distributions due to the vortex state of YBCO using β -NMR. We find a significant inhomogeneous broadening of the NMR attributed to the underlying VL in YBCO. However, the observed resonances have several unexpected properties. In particular, they are broader and more symmetric than for an ideal VL. The anomalous broadening is most evident in high fields where there is no significant contribution from the regular VL. These effects are attributed to long wavelength disorder from pinning at twin or grain boundaries. The temperature dependence of the disorder-related broadening does not scale with $1/\lambda^2$, suggesting there is a contribution to the linewidth in the bulk of the vortex state that does not track the superfluid density. This is likely to have only a minor effect on the interpretation of data on crystals where the observed lineshape is close to that expected from a well ordered VL. However, it can be significant in powders or crystals where there is substantial disorder in the VL. In particular, when the broadening is dominated by VL disorder on a long length scale (i.e. much bigger than λ) the temperature dependence of the linewidth does not scale with $1/\lambda^2$ and therefore cannot be used to determine the symmetry of the superconducting gap.

Bibliography

- [1] E. H. Brandt, *J. Low Temp. Phys.* **139**, 21 (2005).
- [2] Z. Salman, D. Wang, K. H. Chow, M. D. Hossain, S. Kreitzman, T. A. Keeler, C. D. P. Levy, W. A. MacFarlane, R. I. Miller, G. D. Morris, T. J. Parolin, H. Saadaoui, M. Smadella, and R. F. Kiefl, *Phys. Rev. Lett.* **98**, 167001 (2007).
- [3] R. Khasanov, A. Shengelaya, A. Maisuradze, F. La Mattina, A. Bussmann-Holder, H. Keller, and K. A. Müller, *Phys. Rev. Lett.* **98**, 057007 (2007).
- [4] J. E. Sonier, S. A. Sabok-Sayr, F. D. Callaghan, C. V. Kaiser, V. Pacradouni, J. H. Brewer, S. L. Stubbs, W. N. Hardy, D. A. Bonn, Ruixing Liang, and W. A. Atkinson, *Phys. Rev. B* **76**, 134518 (2007).
- [5] E. H. Brandt, *J. Low Temp. Phys.* **73**, 355 (1988).
- [6] Y. M. Belousov and V. P. Smilga, *Spectroscopy of High-Tc Superconductors: A Theoretical View* By N. M. Plakida, page 236-292, CRC Press (2003).
- [7] R. I. Miller, R. F. Kiefl, J. H. Brewer, J. E. Sonier, J. Chakhalian, S. Dunsiger, G. D. Morris, A. N. Price, D. A. Bonn, W. H. Hardy, and Ruixing Liang, *Phys. Rev. Lett.* **88**, 137002 (2002).
- [8] M. H. S. Amin, I. Affleck, and M. Franz, *Phys. Rev. B* **58**, 5848 (1998).
- [9] J. E. Sonier, J. H. Brewer, R. F. Kiefl, G. D. Morris, R. I. Miller, D. A. Bonn, J. Chakhalian, R. H. Heffner, W. N. Hardy, and R. Liang, *Phys. Rev. Lett.* **83**, 4156 (1999).

- [10] M. Franz, C. Kallin, P. I. Soininen, A. J. Berlinsky, and A. L. Fetter, *Phys. Rev. B* **53**, 5795 (1996).
- [11] M. H. S. Amin, M. Franz, and I. Affleck, *Phys. Rev. Lett.* **84**, 5864 (2000).
- [12] H. Hilgenkamp, and J. Mannhart, *Rev. Mod. Phys.* **74**, 485 (2002).
- [13] G. Blatter, M. V. Feigel'man, V. B. Geshkenbein, A. I. Larkin and V. M. Vinokur, *Rev. Mod. Phys.* **66**, 1125 (1994).
- [14] D.J. Bishop, P. L. Gammel, D. A. Huse, and C. A. Murray, *Science* **255**, 165 (1992).
- [15] M. Yethiraj, H. A. Mook, G. D. Wignall, R. Cubitt, E. M. Forgan, D. M. Paul, and T. Armstrong, *Phys. Rev. Lett.* **70**, 857 (1993).
- [16] P. L. Gammel, D. J. Bishop, G. J. Dolan, J. R. Kwo, C. A. Murray, L. F. Schneemeyer, and J. V. Waszczak, *Phys. Rev. Lett.* **59**, 2592 (1987).
- [17] J. A. Herbsommer, G. Nieva, and J. Luzuriaga, *Phys. Rev. B* **61**, 11745 (2000).
- [18] I. Maggio-April, C. Renner, A. Erb, E. Walker, and Ø. Fisher, *Nature* **390**, 487 (1997).
- [19] Ch. Simon, A. Pautrat, G. Poullain, C. Goupil, C. Leblond-Harnois, X. Chaud, and A. Brulet, *Phys. Rev. B* **70**, 024502 (2004).
- [20] D. S. Fisher, M. P. A. Fisher, and D. A. Huse, *Phys. Rev. B* **43**, 130 (1991).
- [21] D. R. Nelson and V. M. Vinokur, *Phys. Rev. Lett.* **68**, 2398 (1992).
- [22] G. P. Mikitik, and E. H. Brandt, *Phys. Rev. B* **79**, 020506(R) (2009).
- [23] For example, see E. Bartolomé, B. Bozzo, X. Granados, F. Sandiunenge, T. Puig, and X. Obradors, *Supercond. Sci. Technol.* **21**, 125002 (2008), and references there in.

- [24] A. Rigamonti, F. Borsa, and P. Carretta, *Rep. Prog. Phys.* **61**, 1367 (1998), and references there in.
- [25] J. E. Sonier, J. H. Brewer, and R. F. Kiefl, *Rev. Mod. Phys.* **72**, 769 (2000), and references there in.
- [26] E. Morenzoni, *Physics and applications of low energy muons*, in *Muon Science*, S. Lee *et al.* Eds., IOP Publishing, Bristol (1999).
- [27] R. F. Kiefl, W. A. MacFarlane, G. D. Morris, P. Amaudruz, D. Arseneau, H. Azumi, R. Baartman, T. R. Beals, J. Behr, C. Bommas, J. H. Brewer, K. H. Chow, E. Dumont, S. R. Dunsiger, S. Daviel, L. Greene, A. Hatakeyama, R. H. Heffner, Y. Hirayama, B. Hitti, S. R. Kreitzman, C. D. P. Levy, R. I. Miller, M. Olivo, and R. Poutissou, *Physica B* **326**, 189 (2003).
- [28] G. D. Morris, W. A. MacFarlane, K. H. Chow, Z. Salman, D. J. Arseneau, S. Daviel, A. Hatakeyama, S. R. Kreitzman, C. D. P. Levy, R. Poutissou, R. H. Heffner, J. E. Elenewski, L. H. Greene, and R. F. Kiefl, *Phys. Rev. Lett.* **93**, 157601 (2004).
- [29] Z. Salman, E. P. Reynard, W. A. MacFarlane, K. H. Chow, J. Chakhalian, S. R. Kreitzman, S. Daviel, C. D. P. Levy, R. Poutissou, and R. F. Kiefl, *Phys. Rev. B* **70**, 104404 (2004).
- [30] Z. Salman, K. H. Chow, R. I. Miller, A. Morello, T. J. Parolin, M. D. Hossain, T. A. Keeler, C. D. P. Levy, W. A. MacFarlane, G. D. Morris, H. Saadaoui, D. Wang, R. Sessoli, G. G. Condorelli, and R. F. Kiefl, *Nano Lett.* **7**, 1551 (2007).
- [31] M. Xu, M. D. Hossain, H. Saadaoui, T. J. Parolin, K. H. Chow, T. A. Keeler, R. F. Kiefl, G. D. Morris, Z. Salman, Q. Song, D. Wang, and W. A. MacFarlane, *Journal of Magnetic Resonance* **191**, 47 (2008).
- [32] H. Saadaoui, W. A. MacFarlane, G. D. Morris, Z. Salman, K. H. Chow, I. Fan, M. D. Hossain, R. Liang, A. I. Mansour, T. J. Parolin,

- M. Smadella, Q. Song, D. Wang, and R. F. Kiefl *Physica B* **404**, 730 (2009).
- [33] C. P. Poole Jr., H. A. Farch, and R. J. Creswick, *Superconductivity*, Academic Press. *Inc.* (1995).
- [34] M. Požek, H. U. Habermeier, A. Maier, and M. Mehring, *Physica C* **269**, 61 (1996).
- [35] A. Steegmans, R. Provoost, R. E. Silverans, and V. V. Moshchalkov, *Physica C* **302**, 159 (1998).
- [36] Ch. Niedermayer, E. M. Forgan, H. Glückler, A. Hofer, E. Morenzoni, M. Pleines, T. Prokscha, T. M. Riseman, M. Birke, T. J. Jackson, J. Litterst, M. W. Long, H. Luetkens, A. Schatz, and G. Schatz, *Phys. Rev. Lett.* **83**, 3932 (1999).
- [37] Microwave data courtesy of D. A. Bonn.
- [38] D. R. Harshman, E. H. Brandt, A. T. Fiory, M. Inui, D. B. Mitzi, L. F. Schneemeyer and J. V. Waszczak, *Phys. Rev. B* **47**, 2905 (1993).
- [39] E. H. Brandt, *Phys. Rev. B* **37**, 2349 (1988), and E. H. Brandt, *Phys. Rev. Lett.* **66**, 3213 (1991).
- [40] D. R. Nelson and V. M. Vinokur, *Phys. Rev. B* **48**, 13060 (1993).
- [41] D. R. Harshman, G. Aeppli, E. J. Ansaldo, B. Batlogg, J. H. Brewer, J. F. Carolan, R. J. Cava, M. Celio, A. C. D. Chaklader, W. N. Hardy, S. R. Kreitzman, G. M. Luke, D. R. Noakes, and M. Senba, *Phys. Rev. B* **36**, 2386 (1987).
- [42] R. F. Kiefl, T. M. Riseman, G. Aeppli, E. J. Ansaldo, J. F. Carolan, R. J. Cava, W. N. Hardy, D. R. Harshman, N. Kaplan, J. R. Kempton, S. R. Kreitzman, G. M. Luke, B. X. Yang, and D. Ll. Williams, *Physica C* **153**, 757 (1988).

- [43] J. E. Sonier, R. F. Kiefl, J. H. Brewer, D. A. Bonn, J. F. Carolan, K. H. Chow, P. Dosanjh, W. N. Hardy, Ruixing Liang, W. A. MacFarlane, P. Mendels, G. D. Morris, T. M. Riseman, and J. W. Schneider, *Phys. Rev. Lett.* **72**, 744 (1994).
- [44] W. N. Hardy, D.A. Bonn, D. C. Morgan, R. Liang, and K. Zhang *Phys. Rev. Lett.* **70**, 3999 (1993).
- [45] W. Eckstein, *Computer Simulation of Ion-Solid Interactions* (Springer, Berlin, 1991).
- [46] A. Abragam, *Principles of Nuclear Magnetism* (Oxford University Press, Oxford, 1961).
- [47] T. J. Parolin, Z. Salman, K. H. Chow, Q. Song, J. Valiani, H. Saadaoui, A. OHalloran, M. D. Hossain, T. A. Keeler, R. F. Kiefl, S. R. Kretitzman, C. D. P. Levy, R. I. Miller, G. D. Morris, M. R. Pearson, M. Smadella, D. Wang, M. Xu, and W. A. MacFarlane *Phys. Rev. B* **77**, 214107 (2008).
- [48] G. J. Dolan, G. V. Chandrashekhar, T. R. Dinger, C. Feild, and F. Holtzberg *Phys. Rev. Lett.* **62**, 827 (1989);
- [49] S. L. Lee, P. Zimmermann, H. Keller, M. Warden, I. M. Savić, R. Schauwecker, D. Zech, R. Cubitt, E. M. Forgan, P. H. Kes, T. W. Li, A. A. Menovsky, and Z. Tarnawski, *Phys. Rev. Lett.* **71**, 3862 (1993).
- [50] U. Divakar, A. J. Drew, S. L. Lee, R. Gilardi, J. Mesot, F. Y. Ogrin, D. Charalambous, E. M. Forgan, G. I. Menon, N. Momono, M. Oda, C. D. Dewhurst, and C. Baines, *Phys. Rev. Lett.* **92**, 237004 (2004).
- [51] A. V. Minkin and S. L. Tsarevskii, *Phys. Sol. Sta.* **46**, 420 (2004).
- [52] E. Olive and E. H. Brandt, *Phys. Rev. B* **57**, 13861 (1998).
- [53] N. Bontemps, D. Davidov, P. Monod, and R. Even, *Phys. Rev. B* **43**, 11512 (1991).

- [54] T. M. Riseman, J. H. Brewer, K. H. Chow, W. N. Hardy, R. F. Kiefl, S. R. Kreitzman, R. Liang, W. A. MacFarlane, P. Mendels, G. D. Morris, J. Rammer, J. W. Schneider, C. Niedermayer, and S. L. Lee, *Phys. Rev. B* **52**, 10569 (1995).
- [55] Y. J. Uemura, G. M. Luke, B. J. Sternlieb, J. H. Brewer, J. F. Carolan, W. N. Hardy, R. Kadono, J. R. Kempton, R. F. Kiefl, S. R. Kreitzman, P. Mulhern, T. M. Riseman, D. L. Williams, B. X. Yang, S. Uchida, H. Takagi, J. Gopalakrishnan, A. W. Sleight, M. A. Subramanian, C. L. Chien, M. Z. Cieplak, G. Xiao, V. Y. Lee, B. W. Statt, C. E. Stronach, W. J. Kossler, and X. H. Yu, *Phys. Rev. Lett.* **62**, 2317 (1989).
- [56] B. Pümpin, H. Keller, W. Kündig, W. Odermatt, I. M. Savić, J. W. Schneider, H. Simmler, and P. Zimmermann, E. Kaldis and S. Rusiecki, Y. Maeno and C. Rossel, *Phys. Rev. B* **42**, 8019 (1990).

Chapter 4

Vortex Lattice Near the Surface of $\text{Pr}_{1.85}\text{Ce}_{0.15}\text{CuO}_{4-\delta}$

4.1 Introduction

In contrast to the *hole-doped* high- T_c cuprate superconductors, less is known about the corresponding electron-doped materials.¹ Some of these systems such as $\text{Pr}_{2-x}\text{Ce}_x\text{CuO}_{4-\delta}$ (PCCO) and $\text{Nd}_{2-x}\text{Ce}_x\text{CuO}_{4-\delta}$ have received special attention because of their similarities with the hole-doped $\text{La}_{2-x}\text{Sr}_x\text{CuO}_{4-\delta}$. One important issue is the correlation between magnetism and superconductivity in the vortex state [1, 2, 3]. In this state, the internal magnetic field distribution $p(B)$ associated with the vortex lattice holds important insights about the phase diagram. For example, $p(B)$ has special features that identify the nature of the vortex state. Only a few experiments can measure $p(B)$, such as μSR and small-angle neutron diffraction (SANS) [3, 4]. Such techniques are sensitive not only to field inhomogeneities of the vortex state, but also to magnetic fields of the rare earth moments and magnetic impurities. However, as bulk techniques, they cannot be used to study thin films, which for the electron-doped cuprates are often more homogeneous in oxygen content than single crystals. Until now, only Low-Energy μSR (LE- μSR) has had the capability to measure $p(B)$ in a depth-resolved manner both above and below the surface [5]. However, LE- μSR is currently limited to relatively low magnetic fields. In this

¹A version of this chapter has been published. H. Saadaoui, W.A. MacFarlane, Z. Salman, G.D. Morris, K.H. Chow, I. Fan, P. Fournier, M.D. Hossain, T.A. Keeler, S.R. Kreitzman, C.D.P. Levy, A.I. Mansour, R.I. Miller, T.J. Parolin, M.R. Pearson, Q. Song, D. Wang, and R.F. Kiefl, *Physica B* 404, 727 (2009). β -NMR investigation of the vortex lattice near the interface of silver and $\text{Pr}_{1.85}\text{Ce}_{0.15}\text{CuO}_{4-\delta}$ thin films.

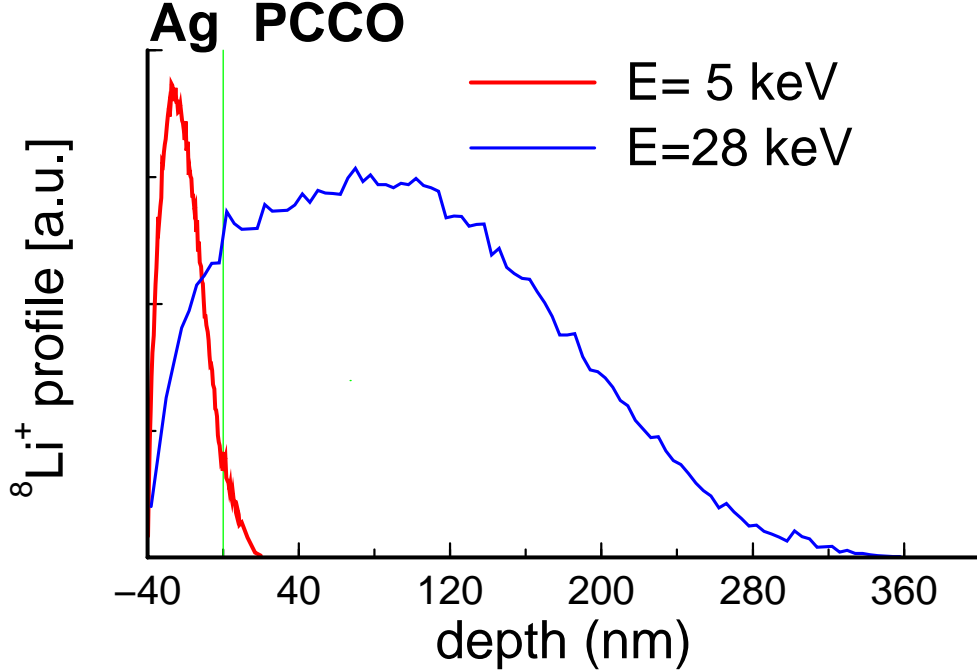


Figure 4.1: TRIM simulation of ${}^8\text{Li}^+$ stopping profile into 40 nm of Ag on 300 nm of PCCO, at energies of 5 keV and 28 keV.

chapter, we use the β -NMR technique, to measure $p(B)$ near the interface between a PCCO film and a thin silver overlayer by stopping the probe ions in the Ag.

4.2 Experimental Details

Our measurements were carried out on a 300 nm thick PCCO film grown by Pulsed Laser Deposition (PLD) at Sherbrooke on a 10×8 mm SrTiO_3 substrate. The PCCO film was near optimally doped ($x \sim 0.15$) with $T_c \sim 22$ K as found by SQUID measurements. X-ray diffraction of the PCCO film revealed the existence of inter-penetrating layers of the insulating impurity phase CeO_2 . This is also confirmed using high-resolution transmission electron microscopy (HRTEM) showing intergrowths with thicknesses ~ 5 nm,

sandwiched between much thicker (50 nm) superconducting PCCO layers [6]. In this case, a stack of correlated vortex states may occur between the disconnected PCCO layers. In order to measure $p(B)$ near the PCCO surface, a 40 nm thin film of Ag was thermally evaporated onto the PCCO. The ${}^8\text{Li}^+$ β -NMR resonance in Ag films below 100 K is known to be temperature independent and narrow [7].

The experiments were performed at TRIUMF's ISAC facility in Vancouver, Canada. In β -NMR, highly spin-polarized ${}^8\text{Li}$ is obtained in-flight via optical pumping with circularly polarized laser light [9]. The time and frequency evolution of the implanted ${}^8\text{Li}$ spin polarization can then be used to monitor magnetic fields near the surface of a material. The ${}^8\text{Li}^+$ nuclear magnetic moments precess in the local field $\mathbf{B}_{\text{local}}$, with a Larmor frequency $\omega_{\text{Li}} = \gamma_{\text{Li}} B_{\text{local}}$, where $\gamma_{\text{Li}} = 0.63015$ kHz/G.

A deceleration system is in place to control the kinetic energy of the implanted ${}^8\text{Li}^+$ beam, i.e. controlling the depth of the beam into the studied material. This is particularly powerful as it allows depth-resolved measurements of $p(B)$ in materials at nm depths [7, 10, 11]. This is an advantage over conventional μSR and other existing β -NMR spectrometers which are limited to bulk studies. In this study, the ${}^8\text{Li}^+$ ions are decelerated from an initial kinetic energy $E = 28$ to 5 keV and stop in the Ag layer, with an implantation profile (Fig. 4.1) peaked 28nm from Ag/PCCO interface according to TRIM simulations[12].

The vortex state is obtained by field-cooling (FC) in static magnetic fields $B_{\text{app}} > B_{c1}$ applied perpendicular to the film surface and parallel to the c -axis of the oriented PCCO film. Two types of measurements were done, (i) spin-polarization versus frequency to measure $p(B)$, where the polarization is subjected to a pulsed RF, and (ii) spin-polarization against time with no applied RF to yield the spin-lattice relaxation rate.

4.3 Results and Discussion

Typical spin relaxation curves are shown in Fig. 4.2. In this experiment, the beam is implanted into the sample for 4 s, and is off for 8 s. The

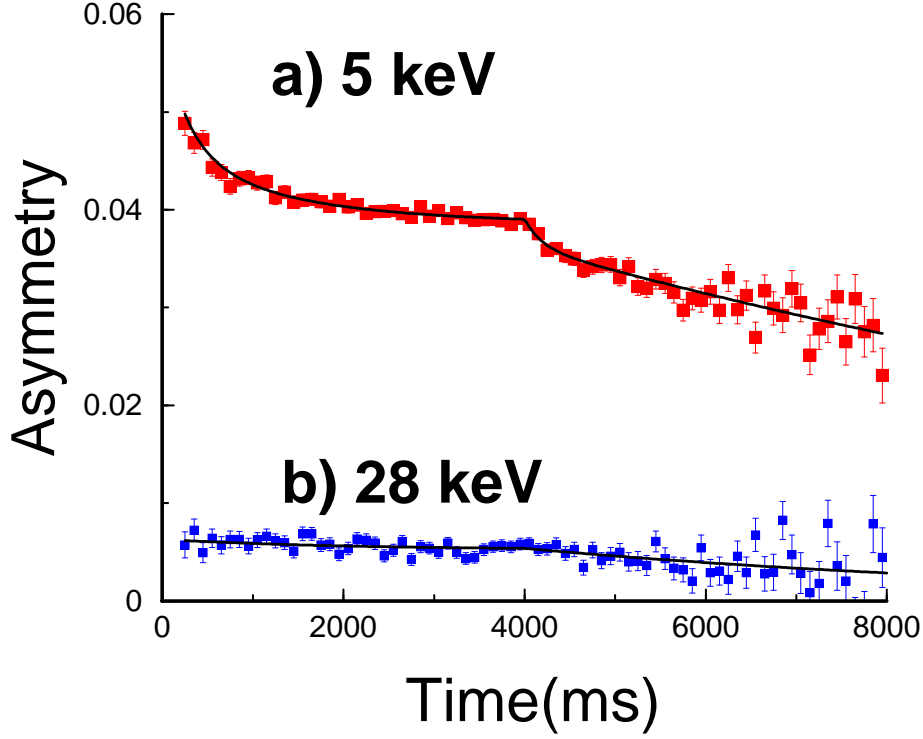


Figure 4.2: Spin relaxation spectra in Ag/PCCO at 5 K, taken in an applied static magnetic field $B_{\text{app}} = 200$ G, and ${}^8\text{Li}^+$ energies of 5 and 28 keV. The solid line is a fit using a phenomenological biexponential function for beam on (0 to 4 s) and beam off (4 s to 8 s) [8].

average nuclear spin polarization of ${}^8\text{Li}$ in the sample, measured in this way, approaches an equilibrium value, determined by a balance between the rate of incoming polarized ${}^8\text{Li}^+$ and the spin-lattice relaxation rate $1/T_1$. After the beam is turned off, the polarization relaxes towards zero. At an energy of 5 keV, about 90% of ${}^8\text{Li}^+$ stop in Ag, so the relaxation is expected to be dominated by the Korringa relaxation in Ag [7]. At 28 keV, most of the ions stop in PCCO, where at this low magnetic field, T_1 is much shorter than the ${}^8\text{Li}$ lifetime and almost no polarization is observed. Therefore, although some of the ${}^8\text{Li}^+$ does stop in the PCCO at 5 keV, the resonance signal is exclusively due to ${}^8\text{Li}^+$ in the Ag layer.

4.3. Results and Discussion

Resonance measurements in low applied fields of $B_{\text{app}} = 216$ G as a function of temperature show a dramatic broadening below T_c , while the line is narrow and temperature independent above T_c . The spectra shown in Fig. 4.3 are quite different than expected for the ideal vortex lattice. The high-field tail (corresponding to high magnetic fields at the vortex cores) is absent, and instead the line is nearly symmetric with a marginal low field tail, suggesting a departure of the vortex structure from a perfect 3-dimensional (3-D) lattice. Our data, from a wide range of applied fields: 100 G to 6.5 T, show a similar behavior of the lineshape. The low field tail may be associated with the tendency of vortices to re-arrange into a 2-dimensional (2-D) lattice in anisotropic materials [13]. A similar lineshape was observed by μSR in $\text{Bi}_2\text{Sr}_2\text{Cu}_2\text{O}_{8+\delta}$ samples and was attributed to a 2-D vortex structure [13]. Although PCCO is known to be quite anisotropic, a 2-D like response may also be due to the presence of CeO_2 intergrowths leading to very thin decoupled superconducting PCCO layers. A disordered lattice may also lead to a symmetric or negatively skewed $p(B)$ as shown by U. Divakar *et al.* [14]. Similar β -NMR experiments on $\text{YBa}_2\text{Cu}_3\text{O}_{7-\delta}$ single crystals and films have shown no evidence of the low field tail and rather exhibit a symmetric lineshape with broadening determined largely by vortex disorder [15].

Another striking feature in Fig. 4.3, is the small positive shift of the resonance frequency upon cooling below T_c . The resonance frequency is plotted in Fig.4.4(a). The net shift is of the order of 1 Gauss. SQUID measurements of the susceptibility on this sample in 1 G and 100 G fields applied parallel to c-axis, under both FC and zero-FC, have shown no paramagnetic Meissner effect [16]. Impurity phases such as $(\text{Pr,Ce,L a})_2\text{O}_3$ are ruled out by neutron scattering below 7 T [17], while pure CeO_2 is non-magnetic.

A similar paramagnetic shift was measured by μSR in bulk single-crystal PCCO samples by Sonier *et al.*, where the net shift at 5 K varied between 10 G at low applied fields (100 G) to 1 G at high field (2 kG) [3]. This was attributed to copper moments ($\sim 0.44 \mu_B$) induced by the external magnetic field. A similar study by Kadono *et al.* on $\text{Pr}_{0.89}\text{LaCe}_{0.11}\text{CuO}_4$ also found a paramagnetic shift in low fields of about 1-5 G associated with

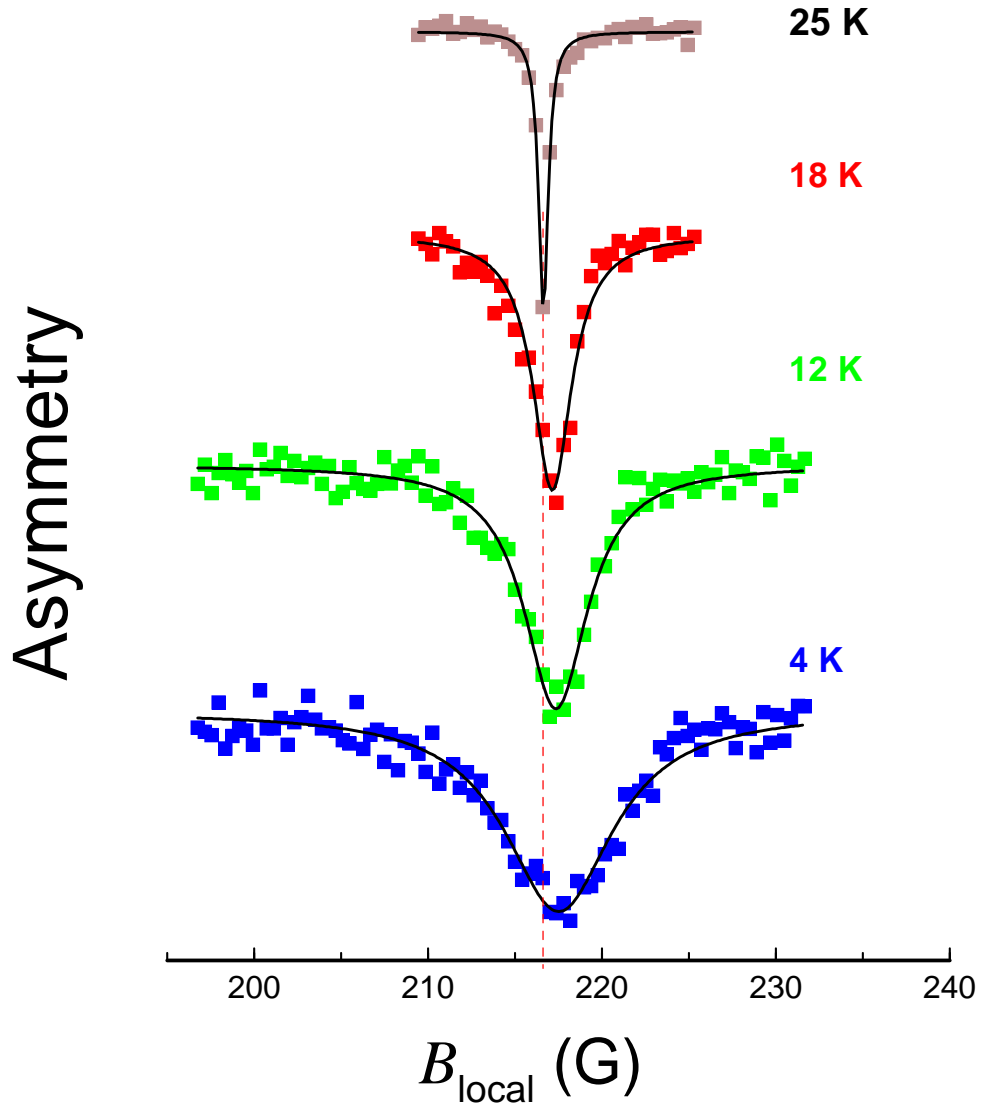


Figure 4.3: The β NMR asymmetry spectra of $^8\text{Li}^+$ implanted at 5 keV in the Ag/PCCO at different temperatures. The dashed line shows the Larmor frequency in the applied magnetic field of $B_{\text{app}} = 216$ G. The solid lines are Lorentzian fits.

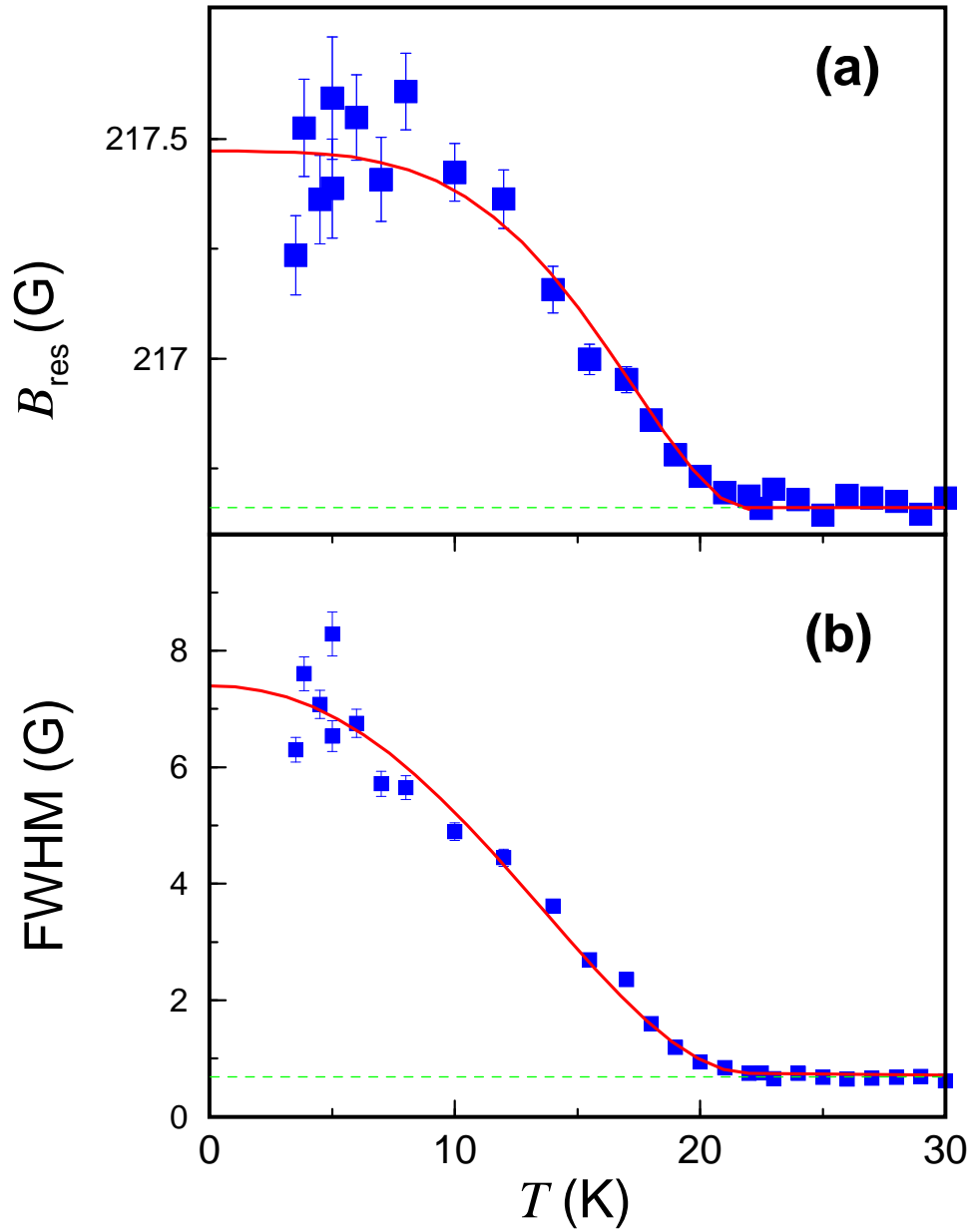


Figure 4.4: (a) The resonance frequency, B_{res} , versus T in an applied field $B_{\text{app}} = 216.62$ G (dashed line), fitted by $B_{\text{app}} + 0.8(1 - (T/22)^4)^2$ (solid line). (b) The linewidth (FWHM) versus T . The solid line represents $\text{FWHM}_{\text{NS}} + 4.2(1 - (T/22)^{2.2})^2$, where $\text{FWHM}_{\text{NS}} = 0.74$ G is the normal state broadening (dashed line). All data are extracted from Lorentzian fits of the resonances.

the weak (van Vleck) magnetization of the Pr ions, due to interaction with antiferromagnetic Cu moments [1]. However, with increasing field, the shift decreased and became negative above 1 kG. We have measured a similar effect in 4.1 T with a shift ~ -8 G, which is consistent with the work of Kadono *et al.*

The full width at half maximum (FWHM) of the Lorentzian fits is plotted in Fig. 4.4. It is temperature independent above T_c , where the width is due to nuclear dipolar broadening in Ag, and increases dramatically below T_c , due to the field inhomogeneity of the vortex state. In the bulk, and for an ideal 3-D arrangement of vortices, the second moment, *i.e.* FWHM/2.355, is proportional to λ^{-2} with the temperature dependence sensitive to the symmetry of the order parameter [3]. However, because of the large error bars on the measured FWHM at low temperatures, and absence of data below 3.5 K, it is hard to draw a conclusion about the nature of the order parameter in PCCO. The FWHM follows the phenomenological form $(1 - (T/T_c)^a)^2$, where $a \approx 2.2$. This unexpected temperature dependence of the FWHM, could be related to the fact that the $^8\text{Li}^+$ probes are outside the PCCO, where the intrinsic vortex lattice broadening is suppressed and $p(B)$ is more sensitive to long-range fluctuations of the vortex density [18].

In conclusion, we have made the first direct measurements of the magnetic field distribution near the surface of an electron-doped superconductor in the vortex state. We have observed an unusual asymmetry of $p(B)$, inconsistent with the ideal vortex lattice, and probably due to both the artificial and intrinsic anisotropy of the sample. We have also observed a paramagnetic shift of the resonance frequency in low fields.

Bibliography

- [1] R. Kadono, K. Ohishi, A. Koda, W. Higemoto, K. M. Kojima, M. Fujita, Shin-ichi Kuroshima and K. Yamada, *J. Phys. Soc. Jpn.* **73** 2944 (2004).
- [2] K. M. Kojima, K. Kawashima, M. Fujita, K. Yamada, M. Azuma, M. Takano, A. Koda, K. Ohishi, W. Higemoto, R. Kadono, and Y. J. Uemura, *Physica B* **374**, 207 (2006).
- [3] J. E. Sonier, K. F. Poon, G. M. Luke, P. Kyriakou, R. I. Miller, R. Liang, C. R. Wiebe, P. Fournier, and R. L. Greene, *Phys. Rev. Lett.* **91**, 147002 (2003).
- [4] R. Gilardi, J. Mesot, S. P. Brown, E. M. Forgan, A. Drew, S. L. Lee, R. Cubitt, C. D. Dewhurst, T. Uefuji, and K. Yamada, *Phys. Rev. Lett.* **93**, 217001 (2004).
- [5] Ch. Niedermayer, E. M. Forgan, H. Glückler, A. Hofer, E. Morenzoni, M. Pleines, T. Prokscha, T. M. Riseman, M. Birke, T. J. Jackson, J. Litterst, M. W. Long, H. Luetkens, A. Schatz, and G. Schatz, *Phys. Rev. Lett.* **83**, 3932 (1999).
- [6] G. Roberge, un-published.
- [7] G. D. Morris, W. A. MacFarlane, K. H. Chow, Z. Salman, D. J. Arsenneau, S. Daviel, A. Hatakeyama, S. R. Kreitzman, C. D. P. Levy, R. Poutissou, R. H. Heffner, J. E. Elenewski, L. H. Greene, and R. F. Kiefl, *Phys. Rev. Lett.* **93**, 157601 (2004).
- [8] Z. Salman, R. F. Kiefl, K. H. Chow, M. D. Hossain, T. A. Keeler, S. R. Kreitzman, C. D. P. Levy, R. I. Miller, T. J. Parolin, M. R.

- Pearson, H. Saadaoui, J. D. Schultz, M. Smadella, D. Wang, and W. A. MacFarlane, *Phys. Rev. Lett.* **96**, 147601 (2006).
- [9] R. F. Kiefl, W. A. MacFarlane, G. D. Morris, P. Amaudruz, D. Arseneau, H. Azumi, R. Baartman, T. R. Beals, J. Behr, C. Bommas, J. H. Brewer, K. H. Chow, E. Dumont, S. R. Dunsiger, S. Daviel, L. Greene, A. Hatakeyama, R. H. Heffner, Y. Hirayama, B. Hitti, S. R. Kreitzman, C. D. P. Levy, R. I. Miller, M. Olivo, and R. Poutissou, *Physica B* **326**, 185 (2003).
- [10] Z. Salman, E. P. Reynard, W. A. MacFarlane, K. H. Chow, J. Chakhalian, S. R. Kreitzman, S. Daviel, C. D. P. Levy, R. Poutissou, and R. F. Kiefl, *Phys. Rev. B* **70**, 104404 (2004).
- [11] Z. Salman, D. Wang, K. H. Chow, M. D. Hossain, S. R. Kreitzman, T. A. Keeler, C. D. P. Levy, W. A. MacFarlane, R. I. Miller, G. D. Morris, T. J. Parolin, H. Saadaoui, M. Smadella, and R. F. Kiefl, *Phys. Rev. Lett.* **98**, 167001 (2007).
- [12] W. Eckstein, *Computer Simulation of Ion-Solid Interactions* (Springer, Berlin, 1991).
- [13] D. R. Harshman, E. H. Brandt, A. T. Fiory, M. Inui, D. B. Mitzi, L. F. Schneemeyer, and J. V. Waszczak, *Phys. Rev. B* **47**, 2905 (1993).
- [14] U. Davikar, A. J. Drew, S. L. Lee, R. Gilardi, J. Mesot, F. Y. Ogrin, D. Charalambous, E. M. Forgan, G. I. Menon, N. Momono, M. Oda, C. D. Dewhurst, and C. Baines, *Phys. Rev. Lett.* **92**, 237004 (2004).
- [15] H. Saadaoui, W. A. MacFarlane, Z. Salman, G. D. Morris, Q. Song, K. H. Chow, M. D. Hossain, C. D. P. Levy, A. I. Mansour, T. J. Parolin, M. R. Pearson, M. Smadella, D. Wang, and R. F. Kiefl, *Phys. Rev. B* **80**, 224503 (2009).
- [16] M. Sigrist and T.M. Rice, *Rev. Mod. Phys.* **67**, 503 (1995).
- [17] M. Matsuura, Pengcheng Dai, H. J. Kang, J. W. Lynn, D. N. Argyriou, Y. Onose, and Y. Tokura, *Phys. Rev. B* **69**, 104510 (2004).

Chapter 4. Bibliography

- [18] M. Xu, M. D. Hossain, H. Saadaoui, T. J. Parolin, K. H. Chow, T. A. Keeler, R. F. Kiefl, G. D. Morris, Z. Salman, Q. Song, D. Wang, and W. A. MacFarlane, *J. Magn. Reson.* **191**, 47 (2008).

Chapter 5

Summary and Conclusions

In this work, we have studied the magnetic properties of the cuprate superconductors using the β -NMR technique. In particular, we have addressed two problems: (i) the occurrence (or lack) of time-reversal symmetry in HTSC near the surface, and (ii) the disorder of the vortex lattice. To answer these questions, the magnetic field distribution was measured near the surface of the superconductor. The measurements were done outside the superconductor rather than inside for a few reasons: (i) The Meissner state inside the superconductor shields the magnetic field due to any magnetic order, and therefore any spontaneous fields due to TRSB are greatly reduced in the bulk. (ii) Vortex lattice disorder that occurs on a long length scale cannot be probed inside the superconductor where the features of the short range ordered lattice are dominant. (iii) Fast spin-relaxation of $^8\text{Li}^+$ inside YBCO and PCCO at low magnetic fields leads to weak or no resonance, and the resonances at high field are also complicated by the nuclear quadrupolar interactions. (vi) Implanting $^8\text{Li}^+$ ions inside the superconductor may perturb the superconductivity.

The measurements were done in silver evaporated onto the superconductors. The Ag capping layer is used as a stopping material for low energy $^8\text{Li}^+$ ions. The separation between the mean stopping depth of $^8\text{Li}^+$ and the interface of the superconductor is varied by changing the thickness of the Ag layer and/or the energy of $^8\text{Li}^+$ ions. Silver is an ideal material for measuring a simple NMR resonance, and exhibits a small linewidth in comparison with the field inhomogeneities expected from the vortex lattice at high applied fields, or TRSB fields. Silver is also an ideal normal metal for coating YBCO, as it does not chemically react or diffuse into YBCO, unlike other metals (e.g. Nb, Cu) which are very reactive with the oxygen in YBCO, and

can form an insulating oxide layer at the interface [1]. However, a limitation of Ag is its surface degradation and agglomeration with time [2] (see Appendix B.2). This has been overcome here by taking our data shortly after coating the superconductors with silver. Studying the normal-metal/HTSC interface is also of importance for technological applications, where understanding the interface is critical for manufacturing superconducting devices based on proximity or Josephson effects [3, 4, 5].

To seek evidence of TRSB, the magnetic field distribution was measured in thin silver layers with thicknesses ranging from 15 to 50 nm deposited on YBCO films. The measured field distribution broadens upon cooling below T_c , signaling the appearance of disordered magnetism from the underlying superconductor. The linewidth of the field distribution, above T_c , is consistent with the temperature independent nuclear dipolar broadening from silver moments. Below T_c , the linewidth increases almost linearly with decreasing temperature without saturation or any sign of the secondary transition observed by some tunneling experiments. The broadening of the field distribution occurred in Ag deposited on YBCO films of both (110) and (001) crystal orientation. Theories suggest that time-reversal symmetry can be broken near the surface of (110)-oriented YBCO, but not in the (001)-oriented films [6]. Hence, the measured broadening is unlikely of a TRSB origin. This conclusion is further supported by the field dependence of the broadening at 10 K, which increases linearly with the applied field. From this, we estimate the net broadening extrapolated to zero field is small ~ 0.2 G, and nearly equals the normal state broadening. We conclude that any spontaneous fields generated near the Ag/YBCO interface must be smaller than 0.2 G at a distance of 8 nm.

TRSB has been observed by only a few studies. In some tunnel junctions, it was estimated that spontaneous fields of a fraction of Tesla could be generated near the surface of YBCO films. Our results are inconsistent with these measurements. In our experiment, we detected no strong magnetic field, but rather small randomly oriented magnetic fields near the surface. It is possible that the spontaneous fields of TRSB have a very short decay length scale. For example, the TRSB fields may order into antiferromagnetic

domains of short length scale compared to the distance where our measurements are done (≥ 5 nm), and thus cannot be resolved. Our estimate is larger than SQUID microscopy which measured weak spontaneous fields of $\approx 10^{-5}$ G near *c*-axis oriented YBCO epitaxial thin films [7].

The field inhomogeneities detected by our probe cannot be ascribed to the proximity effect, where superconductivity “leaks” into Ag. For this phenomenon to take place the superconductor has to be in a good electrical contact with the normal metal. However, the Ag layers were deposited ex-situ on all the YBCO samples, where we do not expect a good ohmic contact and the resistivity of the SN contact is high [8]. The proximity effect is well established for metals in contact with the *s*-wave superconductors because of their isotropic order parameter, and large coherence lengths [9]. To rule out completely this effect, experiments should be done on YBCO coated in-situ with silver or gold, and YBCO/insulator/Ag junctions. For comparison, β -NMR experiments should be also conducted on *s*-wave superconductors with in-situ and ex-situ deposited Ag. A recent β -NMR experiment on Nb coated in-situ with Ag showed clear manifestation of the superconducting proximity effect in Ag with features of the field distribution and spin-lattice relaxation that are very different from the results presented in this thesis.

Spin-relaxation experiments are also needed to address the question of TRSB. Preliminary results given in Appendix D have proved the feasibility of such measurement in YBCO (without Ag), although the signal is fast relaxing on the $^8\text{Li}^+$ time scale. Spin-lattice relaxation could be performed as a function of a weak external field (0–200 G) and temperature. Zero field measurements are also possible, provided that the spin-relaxation is not too fast. These could detect dynamic magnetic fields associated with possible fluctuations of the order parameter in YBCO rather than the static fields that have been measured in Chapter 2.

Similar to the TRSB measurements, studies of the vortex lattice of YBCO and PCCO superconductors have been conducted. In principle, β -NMR is able to probe the vortex lattice near the surface of type II superconductors, e.g. NbSe₂ [11]. The technique of proximally probing the vortex lattice field inhomogeneities outside (rather than inside) the superconduc-

tor has been previously demonstrated. For example, it has been used by Low-energy μ SR to probe the field distribution in a silver film associated with the emerging vortices from the underlying YBCO [12]. Similarly, NMR and ESR techniques have used spin labels deposited onto the superconductors to measure the field distribution [13, 14]. Our results clearly show that magnetic flux penetration into YBCO may be dominated by grain and twin boundary effects in many instances. Disorder of the vortex lattice occurring on a long (μm) length scale leads to strong modifications of the field distribution of a long range ordered vortex lattice. Surprisingly, the temperature dependence of the measured penetration depth, if extracted from the field distribution, reflects the temperature dependence of the vortex lattice disorder more than that of the intrinsic penetration depth of the material. Our results thus provide a clear explanation of why early experiments on powders or highly twinned YBCO crystals have measured an effective penetration depth with a temperature dependence close to that expected from the s -wave order parameter. To measure the penetration depth of HTSC, one must use high quality detwinned crystals. In addition, for measurements outside the superconductor, one must probe the field distribution at distances of few nm away from the surface, where the field inhomogeneities of the regular vortex lattice are dominant.

The experiments conducted on the electron-doped superconductor PCCO films have shown a similar, but narrower, field distribution than in YBCO. However, the effect may be related to an intergrowth of insulating CeO_2 layers separating PCCO superconducting layers, which leads to a weakly coupled 2D vortex lattice. We observed a paramagnetic shift of the most probable field. This finding is consistent with bulk μ SR, and attributed to field induced antiferromagnetic ordering of the Cu moments [15]. A new generation of PCCO films are now grown free of the insulating phase, and should be investigated. The order parameter in PCCO cannot be resolved in our measurements due the extrinsic insulating phase as well as the limited temperature range of β -NMR cryostat. This could be overcome once a new low temperature cryostat (under design) is constructed.

In all these experiments, the measured field distribution broadens upon

cooling below T_c . The micro-structure of the SN boundary and surface roughness of the superconductors could also contribute. It is known that precipitates and chemical inhomogeneities including surface roughness lead to a local variation of the order parameter and flux-line energies, giving rise to pinning forces in the normal conductor [16]. However that would not be the leading source here, as the YBCO films had an almost atomically smooth surface. For example, the YBCO film studied in Chapter 3 is atomically flat as confirmed by STM measurements, but displayed higher broadening than the untwinned crystal which has relatively a larger surface roughness. In the TRSB studies, it could be possible that such measurements are influenced by the nm scale roughness, but regardless, the magnitude of the broadening is so small that TRSB can be ruled out safely.

In conclusion, we have ruled out the occurrence of TRSB or any other source of spontaneous magnetic fields exceeding 0.2 G at distances of 8 nm from the YBCO surface, and confirmed that the disorder in the vortex lattice can modify the temperature dependence of the field distribution linewidth, and hence the penetration depth extracted from it. This work demonstrates the applicability of β -NMR to study unconventional superconductors. For example, it would be interesting to probe magnetism near the surface of Sr_2RuO_4 , and compare with the μSR results which detected bulk TRSB. One can also use β -NMR to study the vortex lattice in the newly discovered FeAs-based HTSC.

Bibliography

- [1] Siu-Wai Chan, Lie Zhao, and C. Chen, Qi Li and D. B. Fenner, *J. Mater. Res.* **10**, 2428 (1995).
- [2] K. Sugawara, M. Kawamura, Y. Abe, K. Sasaki, *Microelectronic Engineering* **84**, 2476 (2007).
- [3] P. A. Rosenthal, E. N. Grossman, R. H. Ono, and L. R. Vale, *Appl. Phys. Lett.* **63**, 1984 (1993).
- [4] R. Kalyanaraman, S. Oktyabrsky, and J. Narayan, *J. of Appl. Phys.* **85**, 6636 (1999).
- [5] V. Pendrick; FL Brown, and J. R. Matey, A. Findikoglu, X. X. Xi, and T. Venkatesan, A. Iham, *J. Appl. Phys.* **69**, 7927 (1991).
- [6] C. R. Hu, *Phys. Rev. Lett.* **72**, 1526 (1994).
- [7] R. Carmi, E. Polturak, G. Koren, and A. Auerbach, *Nature* **404**, 853 (2000)
- [8] S. C. Sanders, S. E. Russek, C. C. Clickner, and J. W. Ekin, *Appl. Phys. Lett.* **65**, 17 (1994).
- [9] S. Guéron, H. Pothier, Norman O. Birge, D. Esteve, and M. H. Devoret, *Phys. Rev. Lett.* **77**, 3025 (1996).
- [10] I. Asulin, A. Sharoni, O. Yulli, G. Koren, and O. Millo, *Phys. Rev. Lett.* **93**, 157001 (2004).
- [11] Z. Salman, D. Wang, K. H. Chow, M. D. Hossain, S. Kreitzman, T. A. Keeler, C. D. P. Levy, W. A. MacFarlane, R. I. Miller, G. D. Morris,

- T. J. Parolin, H. Saadaoui, M. Smadella, and R. F. Kiefl, *Phys. Rev. Lett.* **98**, 167001 (2007).
- [12] Ch. Niedermayer, E. M. Forgan, H. Glückler, A. Hofer, E. Morenzoni, M. Pleines, T. Prokscha, T. M. Riseman, M. Birke, T. J. Jackson, J. Litterst, M. W. Long, H. Luetkens, A. Schatz, and G. Schatz, *Phys. Rev. Lett.* **83**, 3932 (1999).
- [13] A. Steegmans, R. Provoost, V. V. Moshchalkov, H. Frank, G. Güntherodt, and R. E. Silverans, *Physica C* **259**, 245 (1996).
- [14] N. Bontemps, D. Davidov, P. Monod, and R. Even, *Phys. Rev. B* **43**, 11512 (1991).
- [15] J. E. Sonier, K. F. Poon, G. M. Luke, P. Kyriakou, R. I. Miller, R. Liang, C. R. Wiebe, P. Fournier, and R. L. Greene, *Phys. Rev. Lett.* **91**, 147002 (2003).
- [16] C. Ciuhu and A. Lodder, *Phys. Rev. B* **64**, 224526 (2001).

Appendix A

RF Modes

In NMR, one applies the RF in two commonly used methods: (i) the continuous wave (CW) where a weak RF oscillating magnetic field is continuously applied, and (ii) the pulsed RF mode, where a short RF pulse is used. In β -NMR we employ similar methods. The pulsed RF is convenient for narrow resonances and has been used in all the TRSB measurements described in Chapter 2, while the CW RF is useful for measuring broader lineshapes in the vortex lattice. In this appendix, I would like to introduce the reader to these two different modes.

A.1 CW RF Mode

In this mode, the RF is on at all times and has a sinusoidal form

$$\mathbf{B}_1(t) = B_1 \cos(\omega t) \hat{x}, \quad (\text{A.1})$$

where $B_1 \sim 0.1 - 1$ G, applied perpendicular to \mathbf{B}_0 and the initial spin polarization. To measure the asymmetry, the frequency $f = \omega/2\pi$ is changed in steps of Δf in a frequency range ΔR . At each frequency, the counts are measured in N bins of time per bin t_b . Each scan is recorded for a time $t_{\text{scan}} = N t_b \Delta R / \Delta f$. For example, for $\Delta R = 100$ kHz, $\Delta f = 250$ Hz, $N = 100$, and $t_b = 10$ ms, the time spent to take each scan is $t_{\text{scan}} = 400$ s. After each scan, the direction of the frequency sweep is reversed and another scan is taken with the same helicity. After two scans with one helicity, the latter is flipped and new scans will be taken, and so on. After about 3-5 good scans for each helicity (10-60 min), one generates the final asymmetry by averaging the scans of each helicity, and taking the difference

A.2. Pulsed RF Mode

of the asymmetry of the two helicities. This mode is convenient for broad lines where the measured width is approximately,¹

$$\sigma = \sqrt{\sigma_{\text{int}}^2 + (\gamma B_1)^2 + (1/T_1)^2}. \quad (\text{A.2})$$

The intrinsic width of the sample is $\sigma_{\text{int}} \geq \gamma B_1$, and $\sigma_{\text{int}} \gg 1/T_1$. Using this mode, we can measure resonances as broad as 20 kHz as reported in Chapter 3. For narrow lines, the resonance has a width comparable to the artificial broadening γB_1 . To overcome this, we use the pulsed mode where the RF is on only a fraction of time.

A.2 Pulsed RF Mode

In order to excite a rectangular frequency band of bandwidth $\Delta\omega$, a shaped RF pulse at the required frequency is applied. The excited frequency range is $\omega \pm \Delta\omega/2$, and the RF is on periodically for short times $t_p \propto 2\pi/\Delta\omega$. A common shape in today's pulsed NMR is the frequency and amplitude modulated hyperbolic secant pulse,²

$$\mathbf{B}_1(t) = B_1 \text{sech}(\beta t) \exp e^{i\phi(t)} \hat{x} \quad (\text{A.3})$$

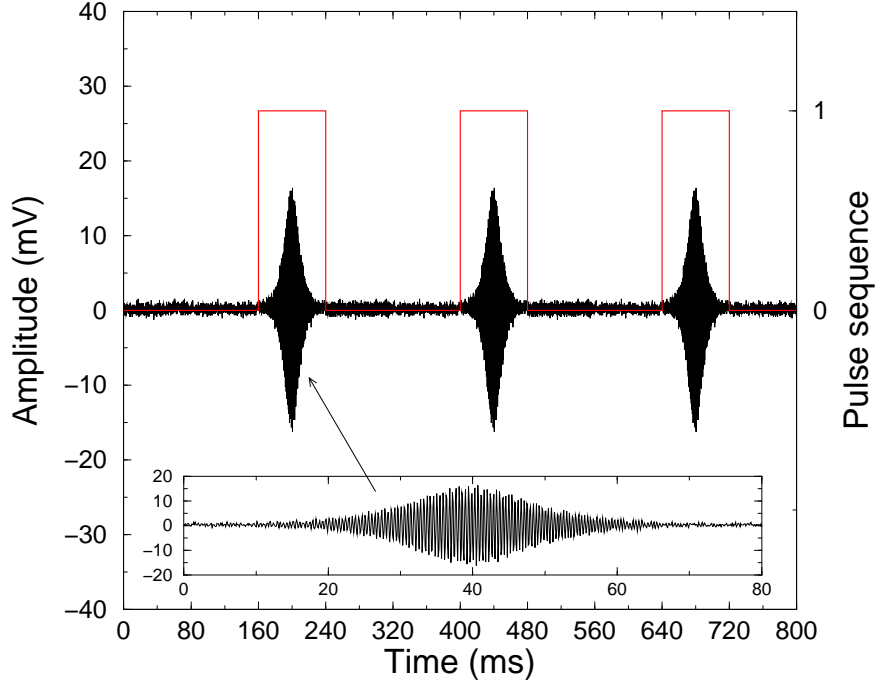
where B_1 is the amplitude ($B_1 \sim 0.1 - 1$ G), β is a constant proportional to the bandwidth, t is truncated between $\pm t_p/2$, $\phi(t) = \mu(\ln(\text{sech}(\beta t)))$ is the phase, and μ is a constant. In β -NMR, short RF 90° pulses are applied periodically to suppress the polarization while the beam is continuous. An example of the pulsed RF is shown in Fig. A.1-(a), where the RF is on during $t_p = 80$ ms corresponding to a bandwidth of $\Delta\omega = 200$ Hz.

The RF pulse is shaped to destroy all the spins in a frequency interval $\omega \pm \Delta\omega/2$. The difference in the polarization after and before the pulse is proportional to the number of spins in that interval. To find the asymmetry, the counts are measured in a time bin t_p before the RF pulse, and after the RF pulse. The asymmetry for each helicity ($h = \pm$) is $A^h(t) = A_a^h(t) - A_b^h(t)$,

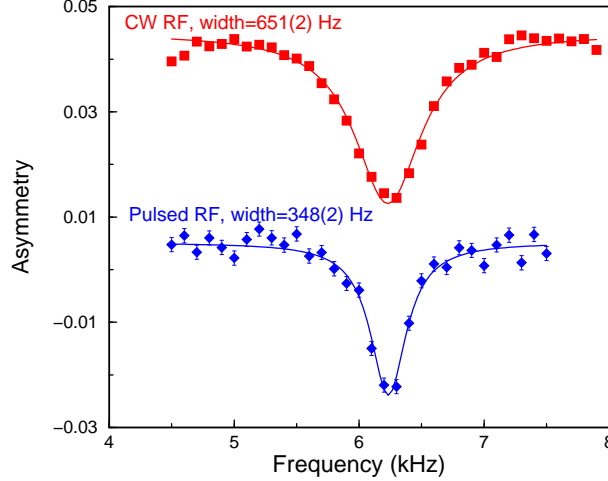
¹T. Parolin *et al.*, Phys. Rev. B **77**, 214107 (2008).

²M. Garwood and L. DelaBarre, J. of Mag. Res. **153**, 1577 (2001).

A.2. Pulsed RF Mode



(a)



(b)

Figure A.1: (a) Pulsed RF sequence where RF is on during a time interval $t_p = 80$ ms. The excited frequencies have a bandwidth $\Delta\omega = 200$ Hz. The functional form is ln-sech, and the pulse sequence controls when the RF is delivered. (b) The spectra in Ag(15 nm)/YBCO at $E = 2$ keV, $T = 10$ K, and $B_0 = 100$ G taken using CW and pulsed RF modes with similar power (B_1) are shown. The width is broadened by a factor of two using CW RF. The width of the resonance taken with the pulsed RF is 348 Hz, which is close to the ideal intrinsic dipolar broadening in Ag of 250 Hz.

A.2. Pulsed RF Mode

where A_b^h is the asymmetry before the pulse, and A_a^h the asymmetry after the pulse for helicity h . The final asymmetry is again the difference of the positive and negative helicity asymmetries $A(t) = A^+(t) - A^-(t)$.

In pulsed RF mode, scanning a frequency range takes few seconds rather than minutes as in the CW mode. The time spent at each frequency is determined by the bandwidth, and is typically 10 ms - 160 ms, i.e. at least 10 times smaller than the CW mode. For example, for $t_p = 160$ ms, the repetition rate is $1/160$ ms = 6.25 Hz (see Fig. A.1-(a)), and for frequency steps $\Delta f = 100$ Hz, one would cover a range $\Delta R = 10$ kHz in $t_{\text{scan}}=16$ s. To accumulate enough statistics each run (final asymmetry) takes about an hour. Because the repetition rate is high, the frequencies of the RF pulse are generated randomly to minimize history effects where slowly recovering polarization after a pulse may contribute to the asymmetry before the next planned pulse.

The pulsed RF has proved useful in the TRSB measurements where the extra broadening below T_c is small and comparable to B_1 . A comparison of the asymmetry measured using the CW and RF pulsed modes is given in Fig. A.1-(b). At the same experimental conditions, the linewidth has been reduced by a factor of two using pulsed RF. Thus, our resolution is higher in pulsed RF than CW RF. The pulsed mode is more convenient for narrow lines of linewidth smaller than $\approx 5 - 10$ kHz. At higher widths, the amplitude of the signal is weak and CW RF is more practical. Note that the net broadening due to the vortex lattice in Chapter 3 is similar using pulsed or CW for resonances of width smaller than 8 kHz.

Appendix B

β -NMR Resonance in Ag

All the results presented in this thesis involved Ag films as a capping layer evaporated on the superconducting materials. The β -NMR resonance in pure Ag will be discussed in this appendix.

B.1 Field and Temperature Dependence

The resonance in Ag is a single Lorentzian at fields below ≈ 1 T, and is a double Lorentzian at higher fields. The two peaks of the resonance above 1 T are due to the $^8\text{Li}^+$ ions stopping in two different sites as discussed in Appendix D. At low fields, since the magnetic splitting is small the two peaks are unresolved, leading to a single resonance.

The single Lorentzian has a weak dependence on field and temperature. The resonance in a silver film of 15 nm grown on an SrTiO_3 substrate has shown no temperature dependence in a low field of 10 G applied parallel to the substrate surface. Shown in Fig. B.1 are the Larmor frequency (ω_L), the full width at half maximum (Δ), the amplitude (A), and the baseline (B) of a Lorentzian fit given by

$$\mathcal{L}(\omega) = B + A \frac{\Delta}{(\omega - \omega_L)^2 + (\Delta/2)^2}. \quad (\text{B.1})$$

The linewidth of the resonance is attributed to the nuclear dipolar moments of the two Ag isotopes. Estimates using the Van Vleck method of moments are found to be between 0.2-0.4 kHz.¹ The β -NMR resonance in Ag has a Lorentzian form independent of the type of RF mode (see Appendix A).

¹A. Abragam, Principles of Nuclear Magnetism (Oxford University Press, 1961).

In Fig. B.1, the data was taken by a pulsed RF mode where the power broadening is minimal.

The absence of any temperature dependence of the resonance spectra proves the advantage of using Ag as a capping layer in this thesis. It also confirms that the broadening observed in Ag/YBCO (see Chapter 2) is exclusively due to the underlying YBCO.

The resonance spectra in a 120 nm Ag film on YBCO, plotted in Fig. B.2-(a), shows the unresolved peaks of the S and O sites at 3.33 T and 100 K. At an energy of 8 keV, all $^8\text{Li}^+$ ions are stopping in the 120 nm Ag layer, and above T_c the lineshape is unrelated to YBCO. It should be noted that the amplitude and resonance shift of the resonance due to $^8\text{Li}^+$ stopping in the S and O is constant below 100 K, as shown in Fig. B.2-(b). Thus, below T_c in the vortex state, the double peaks are almost unresolved, leading to a single resonance as shown in Fig. B.2-(a).

B.2 Effect of the Dewetting Transition in Ag

The β -NMR spectra at low fields in Ag showed an aging effect. An Ag film that was studied one month after it was grown has shown a width of 314 Hz. Measured 8 months later, the same film showed twice the original broadening. A comparison of both resonances is given in Fig. B.3. Fortunately, this effect is only significant if the silver is few months old. All our TRSB experiments were done within 1 to 2 months after the YBCO was capped with Ag. The aging effect leads to a small broadening of the signal, therefore it does not affect our vortex lattice measurements where the broadening is 5-30 kHz. While, the extra broadening measured in Chapter 2 is still twice bigger than the extra age-related broadening.

The extra broadening is likely due to the dewetting transition in Ag.² Using atomic force microscopy (AFM), as shown in Fig. B.4, the surface of a freshly grown Ag (15 nm thick) is smooth, with a root mean square (RMS) roughness between 2-5 nm. The roughness, however, increases for older samples to about 10-20 nm. Impurity atoms that condense onto the

²e.g. M. M. R. Evans, B. Y. Han, J. H. Weaver, surface science **465**, 90 (2000).

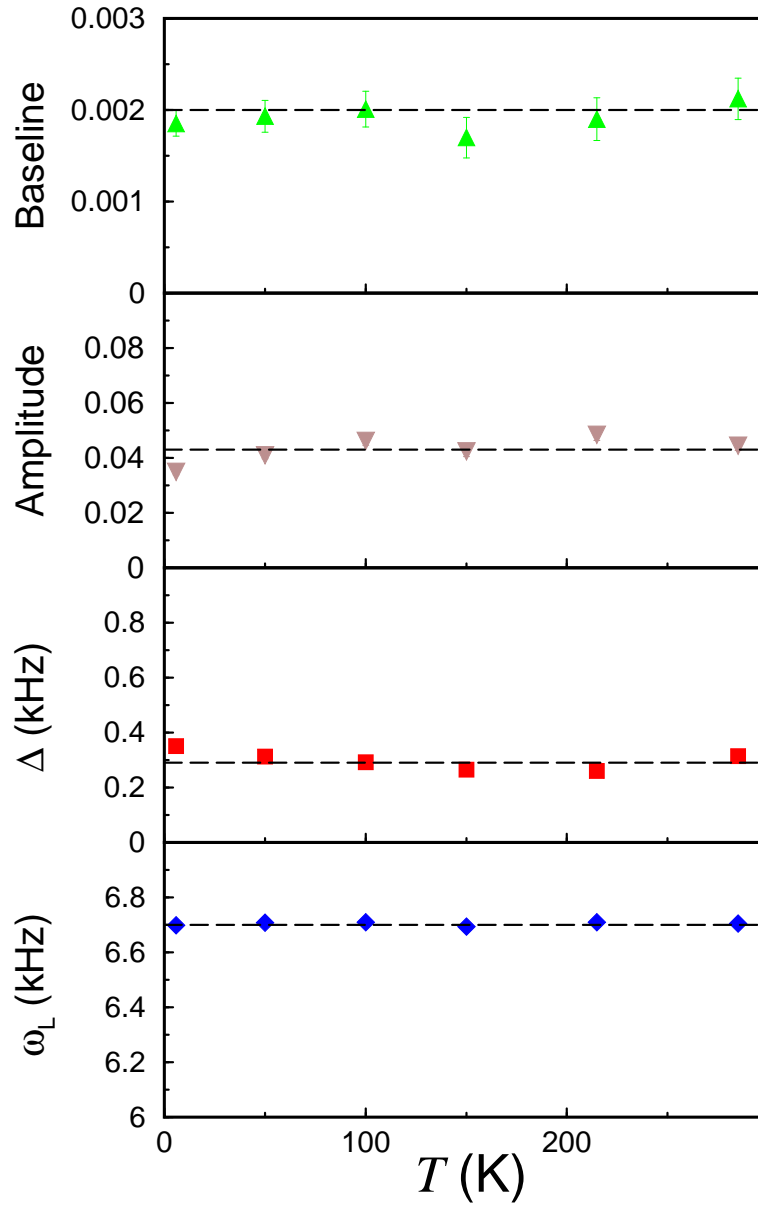


Figure B.1: The temperature dependence the Larmor frequency, FWHM, amplitude and baseline of Lorentzian fits of β -NMR resonances in an 15 nm film thick Ag evaporated on SrTiO₃. The data is taken with a 2 keV $^8\text{Li}^+$ beam in an external field $B_0 = 10$ G, applied parallel to the surface of the substrate.

B.2. Effect of the Dewetting Transition in Ag

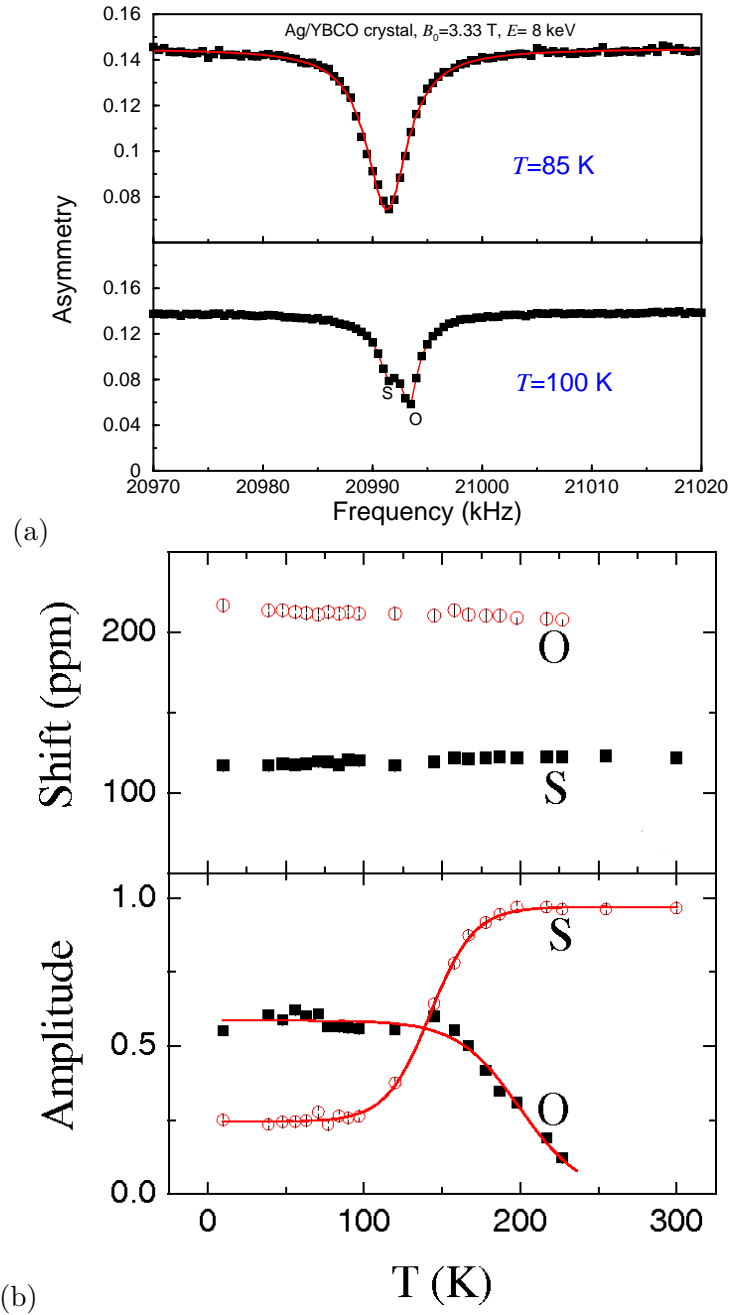


Figure B.2: (a) β -NMR resonances in Ag(120 nm) on YBCO twinned crystal at $B_0 = 3.33$ T and $E = 8$ keV. Solid lines are fits to one (two) Lorentzian(s) at 100 (85) K. (b) The shift and amplitude of the S and O peaks are plotted against temperature at 3 T. Copied from G. D. Morris *et al.*, Phys. Rev. Lett. **93**, 157601 (2004).

B.2. Effect of the Dewetting Transition in Ag

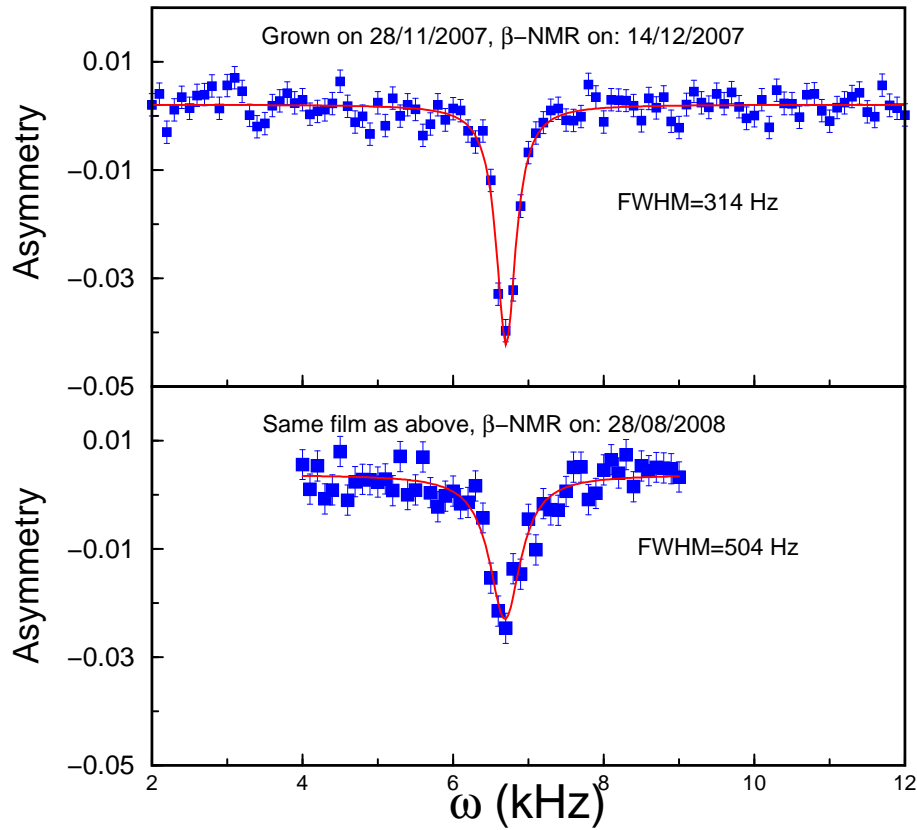


Figure B.3: The β -NMR spectra in Ag(15 nm)/STO at room temperature where $B_0 = 10$ G, and $E_{Li} = 2$ keV. The linewidth increases from 314 Hz, when measured in December 2007, to 504 Hz in August 2008.

surface could also contribute. Auger spectroscopy has shown the existence of carbon and sulfur atoms in the first few atomic layers of the Ag films (Fig. B.5). These parasite atoms have probably precipitated onto the sample after it was exposed to ambient air and may broaden the lineshape if they are magnetic. However, from our measurements it is very clear that in fresh Ag films the dewetting effect and impurity atoms have no contribution to the signal.

B.2. Effect of the Dewetting Transition in Ag

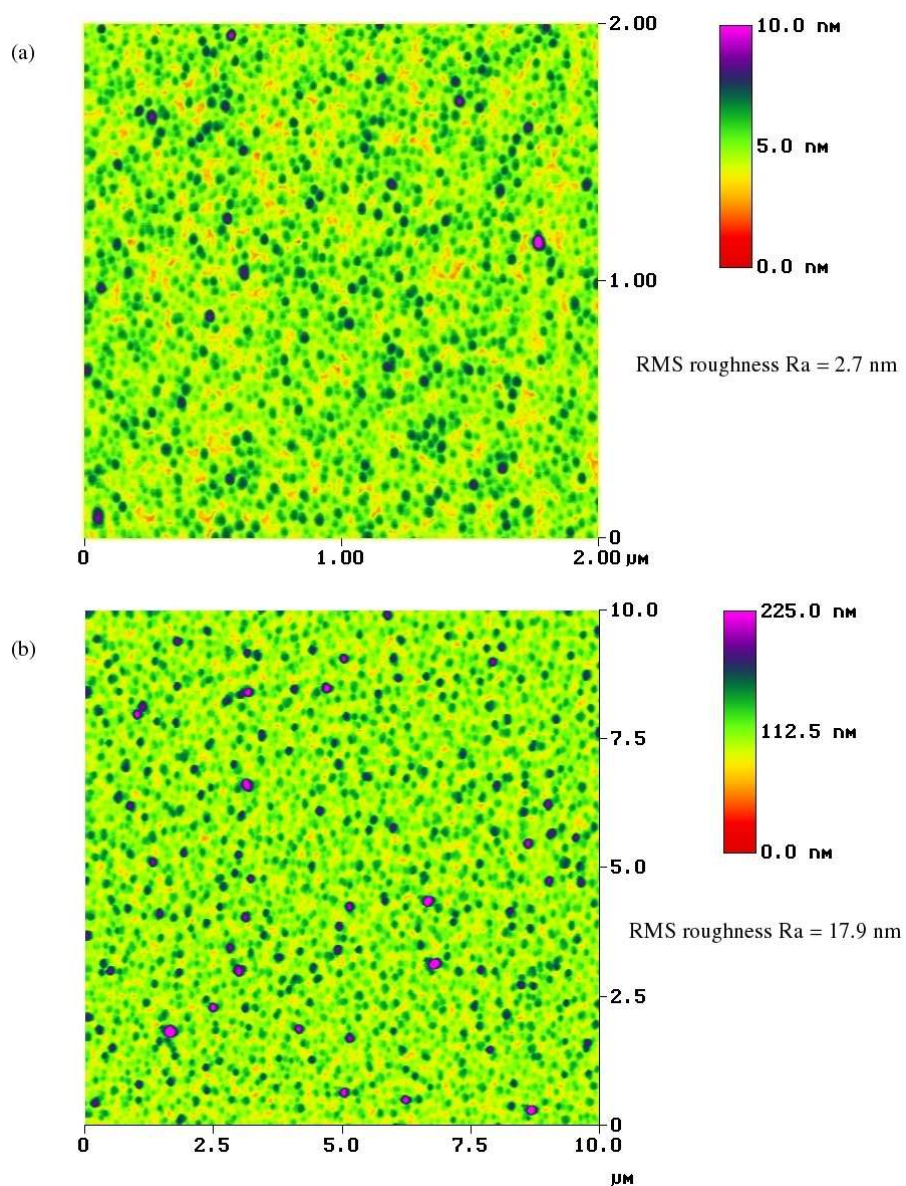


Figure B.4: AFM of silver films showing an increase in the surface roughness with time. (a) AFM is done immediately after evaporating 15 nm of Ag onto an STO substrate. (a) AFM done 8 months after 15 nm of Ag was evaporated onto an STO substrate (this sample is different from the one used in (a)).

B.2. Effect of the Dewetting Transition in Ag

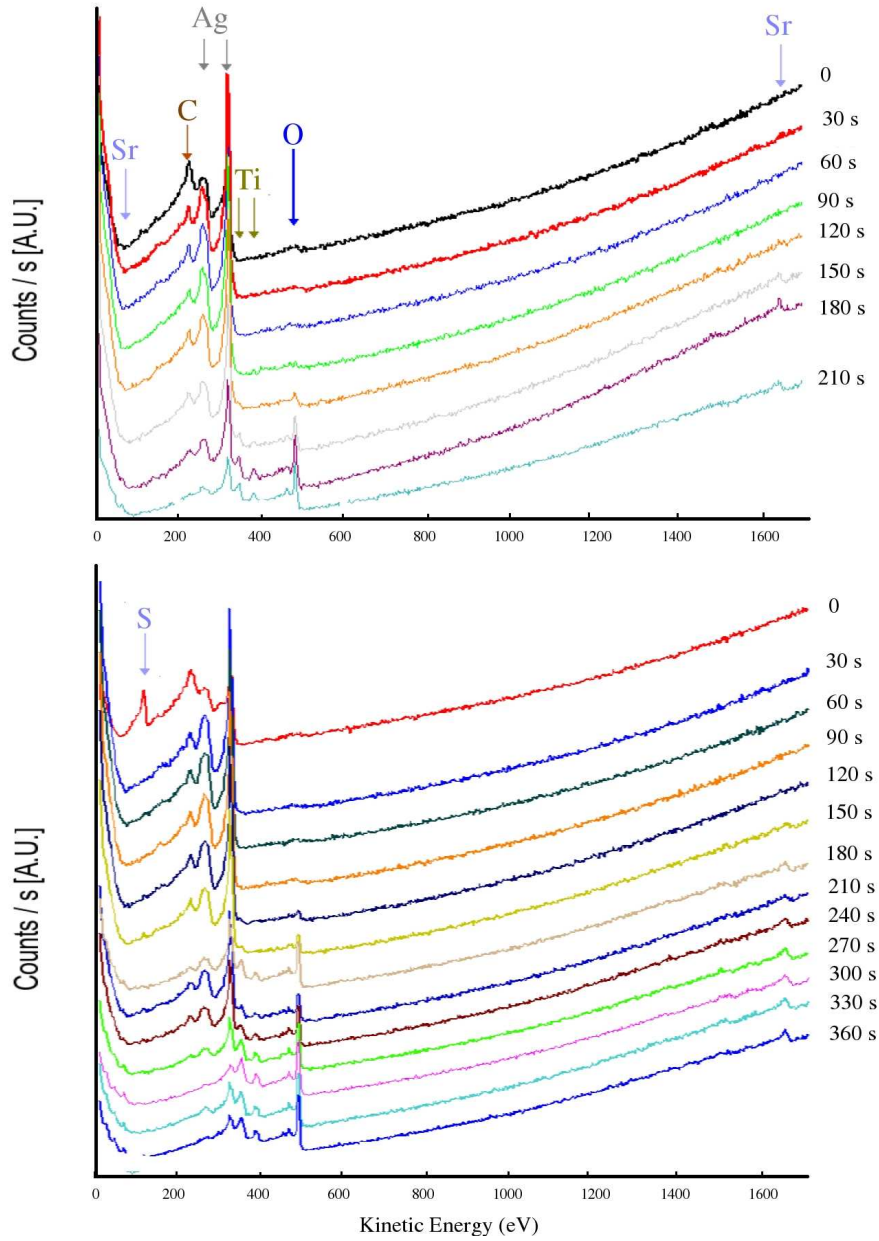


Figure B.5: Auger depth profile of (a) fresh Ag(15 nm)/STO, and (b) few weeks old sample. Ion bombardment time is given in seconds. The sample was sputtered by Ar, removing layers at a rate of ≈ 0.1 nm/s. Carbon, oxygen, and Sulfur atoms have been identified in the first top layers.

Appendix C

Obtaining Zero-Field

The objective of our TRSB measurements is to search for small spontaneous magnetic fields generated near the surface of YBCO superconducting films. In such experiments, the field is applied parallel to the surface of the superconductor, $\mathbf{B}_0 \parallel \hat{z}$, and varied between 10 to 150 G (see Fig. 2.1). However, the applied field may also have x and y -components which originate mainly from stray fields in the Helmholtz coils around the sample. The x -component of the applied magnetic field B_{0x} , perpendicular to the surface (in the low field spectrometer), should be smaller than the lower critical field $B_{c1\perp} \sim 1$ G to reach the Meissner state and avoid inducing a vortex state in YBCO. Minimizing this component also diminishes the demagnetization corrections.

It is not possible to accurately measure the components of the applied field at the sample position due to the lack of sensitive Hall probes that are UHV compatible and can fit in the limited empty space surrounding the sample in the cryostat. However, B_{0x} and B_{0y} , can be accurately set to zero using Morris and Heffner's routine.¹ This method depends on measuring the resonance frequencies in Ag or any other suitable sample with a large narrow resonance in a set of x , y , and z field scans, and then extracting the currents needed to achieve zero field. Here, we set the main component to $B_{0z} = 10$ G, and vary the second component around zero covering a range of few Gauss, while keeping the third component fixed. The exact routine is as follows:

- (i) Set the current I_z to 4.3 A which corresponds to about 10 G.
- (ii) Measure the resonance as a function of I_x , while keeping the other currents fixed: $I_y = 0$ and $I_z = 4.3$ A.

¹G. D. Morris and R. H. Heffner, Physica B **326**, 252 (2003).

Appendix C. Obtaining Zero-Field

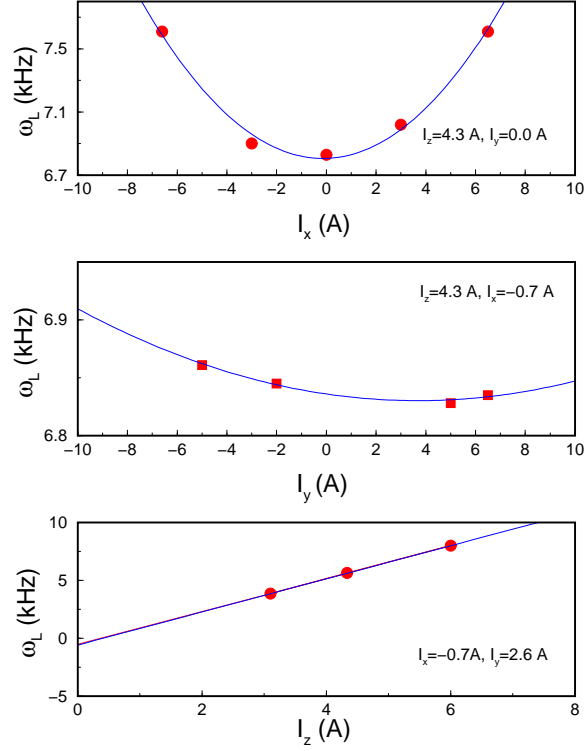


Figure C.1: Variation of the Larmor frequency, ω_L , with the currents I_x , I_y , I_z which run into three Helmholtz coils and create fields along x , y , and z direction, respectively.

- (iii) Fit the resonance to extract the Larmor frequency to $\omega_L = \gamma_{\text{Li}} \sqrt{B_{0z}^2 + (aI_x + b)^2}$ to find the constants a , b , and B_{0z} .
- (iv) Set the current I_x to the value that minimizes ω_L : $I_x = -\frac{b}{a}$.
- (v) Repeat (iii) and (iv) for I_y .
- (vi) Measure the resonance versus I_z and fit the Larmor frequency to $\omega_L = \gamma_{\text{Li}}(aI_z + b)$.
- (vii) If cooling in zero field is necessary, the current I_z must be set to $I_z = -\frac{b}{a}$ above T_c before cooling.

Appendix C. Obtaining Zero-Field

This routine has been used to produce the results in Fig. C.1. The resonances were taken in a gold foil. This procedure minimizes the field along x and y direction to less than 0.1 G which can be estimated from the uncertainty on the minimum of the Larmor frequency in Fig. C.1. Our TRSB measurements required cooling below T_c in zero field, so it was necessary to set the current I_z to a value that leads to zero field.

Appendix D

Spin-Lattice Relaxation

In β -NMR, in addition to measuring the resonance, spin relaxation can also be measured. This offers additional information about the behavior of the spin polarization, which is influenced by the fluctuating magnetic fields in the host material, on a time scale of ω_L^{-1} ; the inverse of the Larmor frequency. This information is complementary to μ SR, as these fields may be static on a time scale of the muon's lifetime $\tau_{\mu^+} = 2.2 \mu\text{s}$. In a material with large fluctuating fields at ω_L , the spin polarization, i.e. asymmetry, is destroyed quickly. Hence, these measurements are also of importance for the resonance measurements, where the polarization is strongly dependent on fluctuating fields and may be destroyed even in the absence of an RF field. In this work, we have made several measurements to study the spin relaxation in Ag, YBCO, and PCCO. Ag/YBCO and Ag/PCCO heterostructures were also investigated to look for the influence of the underlying superconductor on the spin-relaxation signal in Ag. These measurements are discussed in this appendix after a short review of the spin-relaxation method.

D.1 Spin-Relaxation Signal

In the the absence of an RF field, the spin-lattice relaxation of the implanted ^8Li is measured by pulsing the beam, and measuring the time dependence of the spin polarization during and after the pulse. To find the asymmetry, the count rates are measured in a time resolution of 10 ms during the beam-on period (typically 0.5 – 4 s) and the beam-off period (8 – 12 s). A typical spectrum is measured in about 30 min with an incoming $^8\text{Li}^+$ rate $R_0 \sim 10^6$ ions/s. The polarization of $^8\text{Li}^+$, initially being p_0 , measured at a later time

D.1. Spin-Relaxation Signal

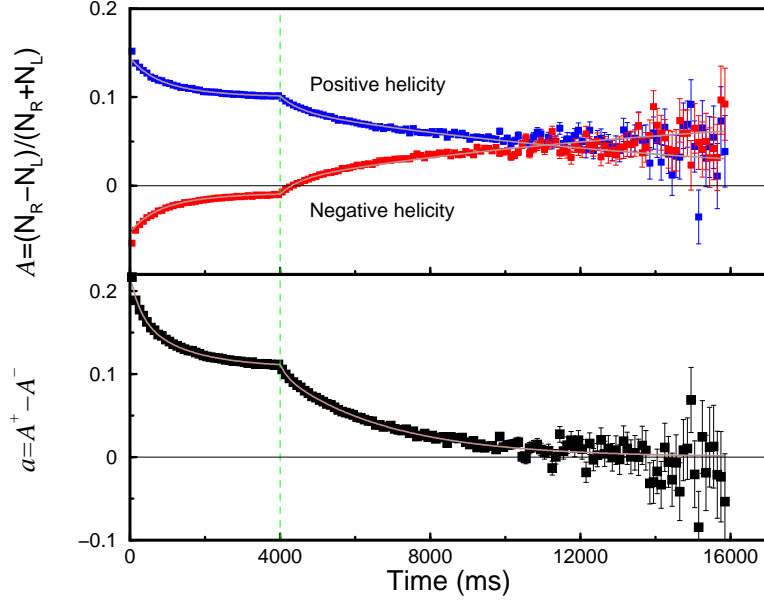


Figure D.1: Spin relaxation spectra recorded in $B_0 = 150$ G. The asymmetry recorded with a Laser of positive (A^+) and negative (A^-) helicity are shown. The overall asymmetry $a = A^+ - A^-$ is also plotted. Solid lines are fits explained in the text.

t yields

$$p(t) = p_0 e^{-t/T_1}, \quad (\text{D.1})$$

where a single mechanism of relaxation with a spin-lattice relaxation rate $1/T_1$ is assumed. During the beam-on, and for a constant incoming beam rate of R_0 , the polarization at t averaged over all times depends on the ${}^8\text{Li}^+$ life time and $1/T_1$,

$$p(t) = \frac{R_0 p_0 \int_0^t dt' e^{-t'/\tau_{\text{Li}}} e^{-t'/T_1}}{R_0 \int_0^t dt' e^{-t'/\tau_{\text{Li}}}}, \quad (\text{D.2})$$

$$= p_0 \frac{\tau' (1 - e^{-t/\tau'})}{\tau_{\text{Li}} (1 - e^{-t/\tau_{\text{Li}}})}, \quad (\text{D.3})$$

where $\frac{1}{\tau'} = \frac{1}{\tau_{\text{Li}}} + \frac{1}{T_1}$. During the beam-on period, the average polarization

approaches the equilibrium value

$$\bar{p} = \frac{R_0 p_0 \int_0^\infty dt' e^{-t'/\tau_{\text{Li}}} e^{-t'/T_1}}{R_0 \int_0^\infty dt' e^{-t'/\tau_{\text{Li}}}} = \frac{p_0}{1 + \tau_{\text{Li}}/T_1}. \quad (\text{D.4})$$

From Eqs. (D.1) and (D.3), the asymmetry $a(t) \propto p(t)$ during (a_d) and after (a_a) the beam pulse of a period Δ , can be written as

$$\begin{aligned} a_d(t) &= a_0 \frac{1 - e^{-t/\tau'}}{1 - e^{-t/\tau_{\text{Li}}}}, & 0 < t \leq \Delta \\ a_a(t) &= a_d(\Delta) e^{-(t-\Delta)/T_1}, & t > \Delta. \end{aligned} \quad (\text{D.5})$$

where a_0 is the maximum β -decay asymmetry at $t = 0$. The above equations are often used to extract $1/T_1$ of ${}^8\text{Li}^+$ in the host material. An example of the spin-relaxation spectra is given in Fig. D.1. The asymmetry was fit to Eq. (D.5) with two functions $a(t) = a^s(t) + a^f(t)$: $a^s(t)$ the asymmetry of a slow relaxing component of rate $1/T_1^s$, and $a^f(t)$ the asymmetry of a fast relaxing component of rate $1/T_1^f$ ($1/T_1^s \ll 1/T_1^f$). The fast component seen in some measurements is likely due to the backscattered ${}^8\text{Li}^+$ stopping in other materials surrounding the sample, such as Cu, Al. The fast component has almost no temperature dependence and is about two orders of magnitude higher than $1/T_1$. The component that we are interested in here is the slow component and we refer to it by $1/T_1$. Note that, β -NMR does not distinguish between $1/T_1$ and $1/T_2$; the spin-spin relaxation; thus all mechanisms are included in $1/T_1$.

D.2 Ag

The relaxation of nuclear spin polarization to equilibrium is generally due to transverse magnetic fields fluctuating at the Larmor frequency. The spin-relaxation rate depends on the temperature and the external magnetic field. In a metal, $1/T_1$ is due to Korringa relaxation of spin flip scattering from the conduction electrons. A feature of this law is the linear variation of $1/T_1$

with temperature as

$$\frac{1}{T_1} = \mathcal{K}^2 T, \quad (\text{D.6})$$

where the Korringa constant \mathcal{K} depends on the density of the conduction electrons at the Fermi levels, and the hyperfine coupling of the conduction electrons to the nucleus. This electronic $1/T_1$ is independent of the magnetic field.

The asymmetry in Ag is strongly temperature dependent due to the Korringa relaxation. This can be seen in Fig. D.2-(a), where the spectra are more slowly relaxing as T decreases. The T -dependence of $1/T_1$, plotted in Fig. D.2-(b), confirms the validity of Korringa law both at low and high temperature and reflects the coupling of $^8\text{Li}^+$ spins to the conduction electrons in Ag. The ‘‘bump’’ in $1/T_1$ at intermediate temperatures is due to the site change of $^8\text{Li}^+$ in Ag. In the FCC lattice of Ag, $^8\text{Li}^+$ could occupy three possible sites of cubic symmetry: substitutional (0,0,0), octahedral (1/2,1/2,1/2) and tetrahedral (1/4,1/4,1/4). The non-cubic sites are excluded due to the absence of quadrupolar splitting in Ag. The substitutional site vacancies are made during the implantation process. From several β -NMR measurements, $^8\text{Li}^+$ at low temperature are trapped in interstitial sites and thermal activation at high temperature leads to a transition to a substitutional site.¹ In Fig. D.2-(b), the relaxation rate is fit to a model with thermally activated O to S transitions.²

The relaxation rate $1/T_1$ is of great importance to the resonance measurements as well. When measuring the resonance, the polarization of a continuously implanted beam approaches the equilibrium value given in Eq. D.4, which defines the baseline of our resonance spectra, i.e. the difference between the off-resonance asymmetry of positive helicity to the negative helicity. Thus, for very fast spin-lattice relaxation ($1/T_1 \rightarrow \infty$), the equilibrium polarization of $^8\text{Li}^+$ approaches zero, making measurements of the resonance impossible. In Fig. D.2-(b), one can see that the baseline of the resonance spectra tracks the same temperature dependence of $1/T_1$. Note

¹G. D. Morris *et al.*, Phys. Rev. Lett. **93**, 157601 (2004).

²M. D. Hossain *et al.*, Physica B **414**, 419 (2009).

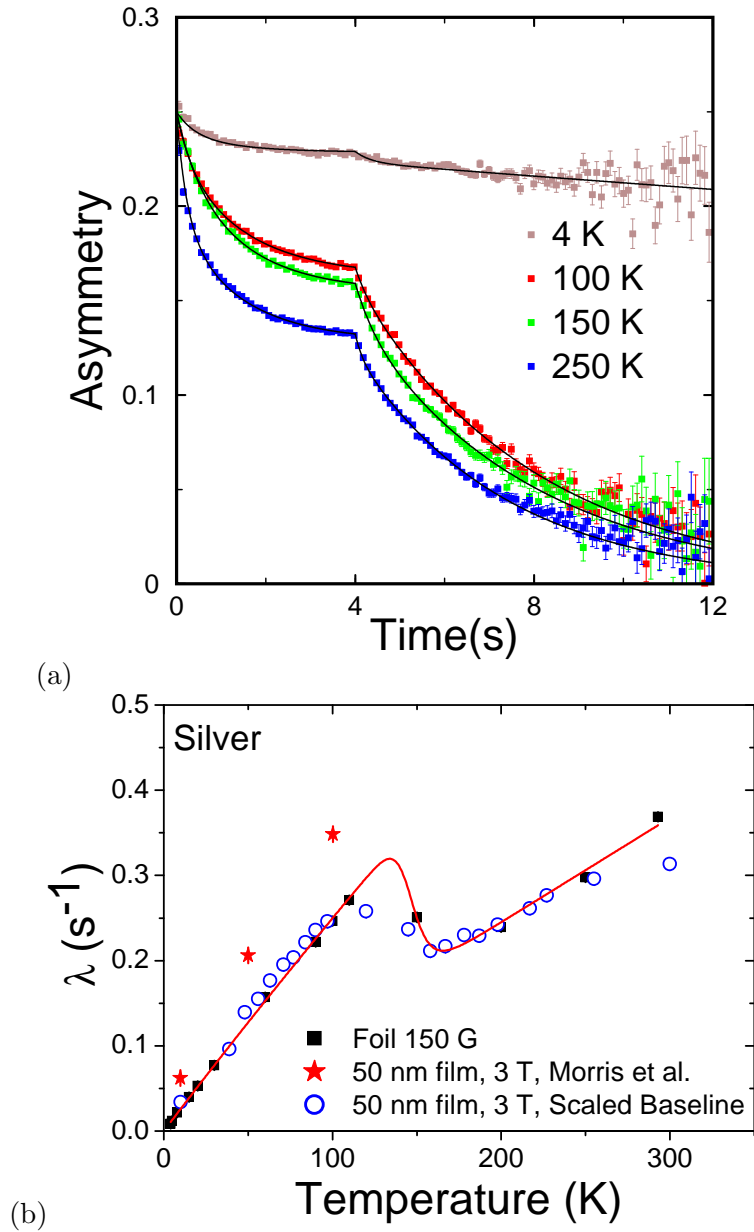


Figure D.2: (a) T -dependence of the spin relaxation in $25 \mu\text{m}$ silver foil at $B_0 = 150 \text{ G}$. The $28 \text{ keV } ^8\text{Li}^+$ beam is implanted into the sample in 4 s pulses every 20 s. Solid lines are fits using Eq. (D.5) with two components. (b) $\lambda = 1/T_1$ (slow component) extracted from (a) compared with the baseline of the resonance in an Ag film (50 nm) taken at 3 T.

that the plotted $1/T_1$ and baseline are extracted from a thin silver film and a bulk Ag foil under different experimental conditions, confirming that the signal is an intrinsic property of Ag and independent of field (see Fig. D.2).

The Korringa law is dominant at high field, where the applied field polarizes a large fraction of the conduction electrons. At very low fields, the polarization approaches zero as the energy levels in $^8\text{Li}^+$ and Ag are degenerate, favoring flip-flop processes between spins.³ The Zeeman splitting created by applying higher magnetic fields lifts this degeneracy and the asymmetry approaches its high field value. This can be seen in Fig. D.3, where at fields below 10 G, the asymmetry falls rapidly to zero, and saturates at fields above 20 G. The enhanced relaxation at low field in Fig. D.3 is attributed to cross relaxation with the Ag spins which is driven by low frequency fluctuations in the magnetic dipolar interaction. This interaction is dominant at low field, while high magnetic fields quenches this interaction leaving only the Korringa relaxation mechanism. For Ag, the $1/T_1$ and amplitude can be fitted to a phenomenological Lorentzian form

$$c_1 + c_2 \frac{B_d^2}{4B_0^2 + B_d^2}, \quad (\text{D.7})$$

where $B_d \approx 12$ (3) G at 293 (5) K (shared between $1/T_1$ and A), is an estimate of the magnitude of the fluctuating field needed to quench the dipole-dipole interaction. These values are comparable to those of $^8\text{Li}^+$ in gold.⁴ The constants c_1 and c_2 are both field and temperature dependent. c_1 values are consistent with Fig. D.2-(b).

From the above discussion, we conclude that one needs to apply an external magnetic field higher than 5 G to measure a signal in Ag with large amplitude. This was taken into account when conducting the TRSB measurements. Ideally, one should do these measurements in zero field. However the loss of polarization in Ag at very low fields requires one to apply a static field that is at least 5 G to obtain a good signal to noise ratio.

³C. P. Slichter, Principles of Magnetic Resonance, 2nd ed., Springer-Verlag (1980).

⁴T. Parolin *et al.*, Phys. Rev. B **77**, 214107 (2008).

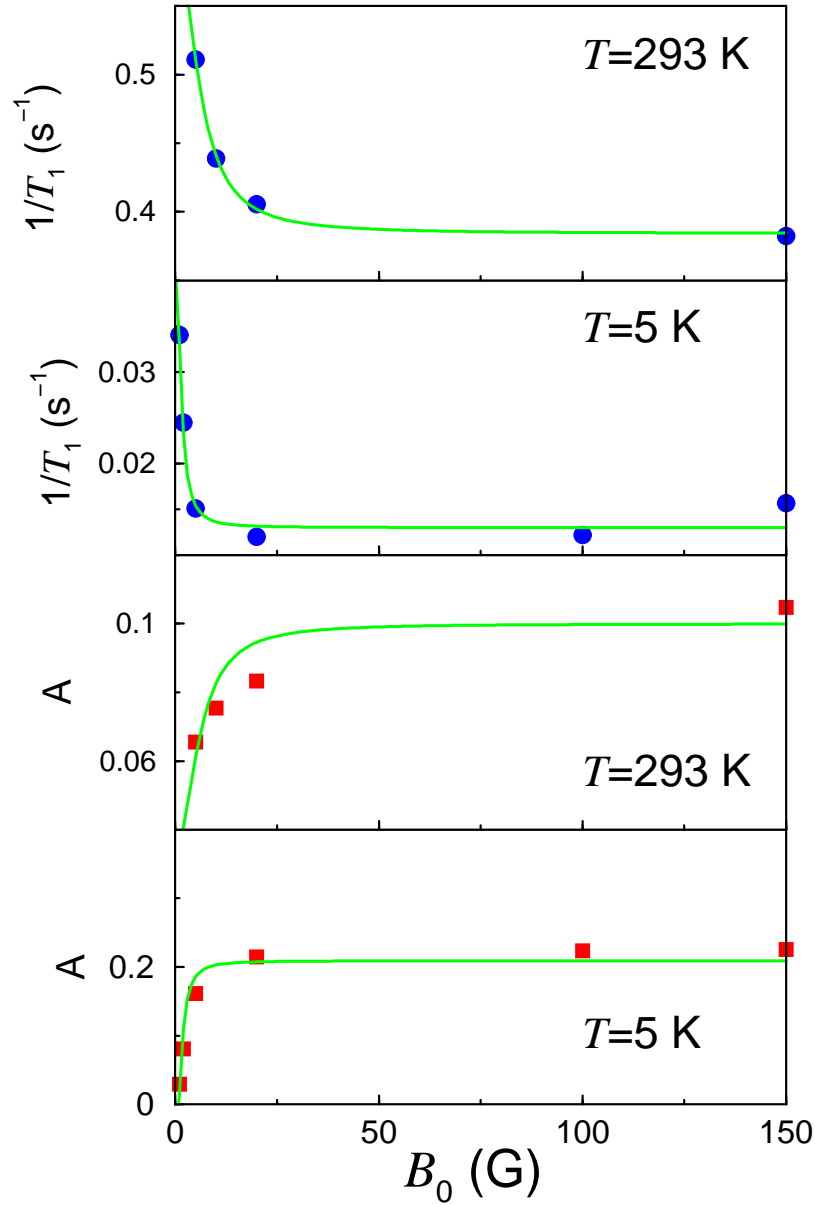


Figure D.3: The B_0 and T -dependence of the amplitude, A , and relaxation rate, $1/T_1$, of $^8\text{Li}^+$ polarization implanted at full energy into a silver foil. The data was extracted by fitting the asymmetry to a pulsed exponential function. A and $1/T_1$ of the slow relaxing part of the function is shown here. The solid lines are fits using a Lorentzian form described in the text.

D.3 Ag/YBCO

The spin-lattice relaxation rate in NMR is a versatile tool in probing the electronic structure of HTSC cuprates. For example, $1/T_1$ of ^{63}Cu have showed evidence of the pseudogap state below the characteristic temperature T^* .⁵ The nuclear and electronic moments of Cu, Y, O atoms in YBCO lead to fast spin-lattice relaxation of $^8\text{Li}^+$ at low magnetic fields. Consequently the $^8\text{Li}^+$ ions stopping in the YBCO do not contribute to the resonance at the Larmor frequency. Thus we are unable to measure the β -NMR resonances in YBCO at low field, but at high field they are seen.⁶

Preliminary measurements of the spin-relaxation of $^8\text{Li}^+$ in Ag on YBCO have shown a fast relaxing signal in YBCO. This sample grown by Theva (Ismaning, Germany), was used in Chapter 2 to study the length scale of the extra broadening observed in Ag below the T_c of YBCO. The asymmetry measured in an applied field of 100 G with a beam of energy 13 keV is shown in Fig. D.4-(a). This shows fast relaxation of the signal at all temperatures due to YBCO with a slow relaxation attributed to Ag. At 13 keV, about 30% of $^8\text{Li}^+$ stops in Ag, 35% in YBCO, and 25% is backscattered.

The spectra at full energy are shown in Fig. D.4-(b) as a function of temperature. At full energy, 15% stops in Ag, 65% in YBCO, and 20% is backscattered. The amplitude of the asymmetry and its temperature dependence look inconsistent with the Ag results (with no YBCO). By plotting the $1/T_1$ versus T as shown in Fig. D.5, one finds a slight upward shift of the relaxation rate from the intrinsic $1/T_1$ of Ag. The extrapolated $1/T_1$ to zero temperature is inconsistent with Ag, and is either due to the Ag/YBCO interface or bulk YBCO. One also notices that the upward shift peaks up at the T_c of YBCO and approaches $1/T_1$ of Ag above T_c .

The energy dependence of the spin relaxation at 10 K is shown in Fig. D.4-(c), and confirms the fast relaxation of the spin polarization as more $^8\text{Li}^+$ stops in YBCO. The energy dependence of $1/T_1$ at 10 K from the above measurements is shown in the inset of Fig. D.5. This shows a linear

⁵See the review: T. Timusk and B. Statt, Rep. of Prog. in Phys., **62**, 61 (1999).

⁶R. F. Kiefl *et al.*, Physica C **326**, 189 (2003).

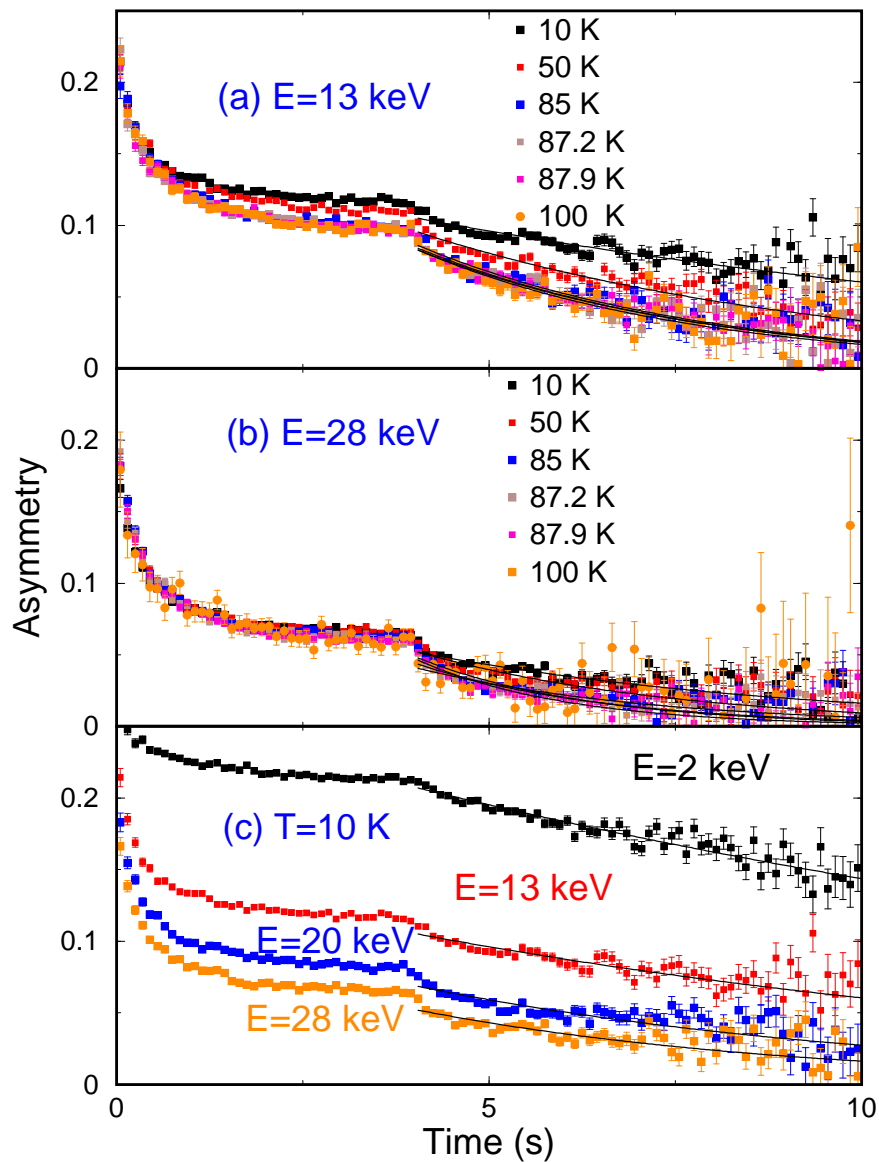


Figure D.4: Spin relaxation of $^8\text{Li}^+$ of energy (a) 13 keV and (b) 28 keV implanted into Ag(50 nm)/YBCO(600 nm) at 100 G applied field under zero field conditions. Solid lines are single exponential fit to the beam off asymmetry. (c) Spin-relaxation spectra versus energy at 10 K.

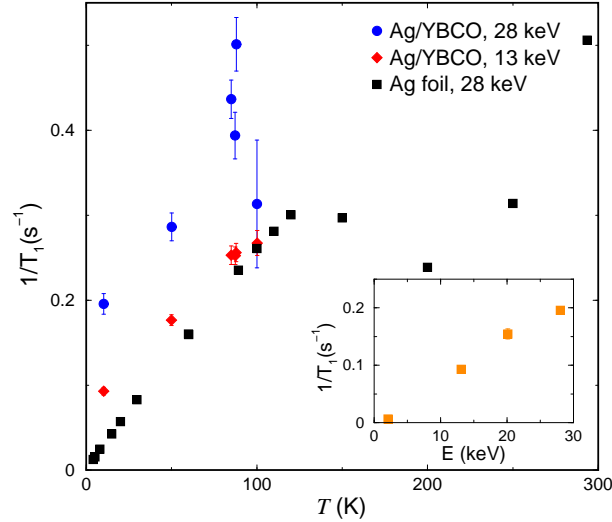


Figure D.5: Temperature dependence of $1/T_1$ in Ag(50 nm)/YBCO(600 nm), at two different energy extracted from Fig. D.4. Also, shown is $1/T_1$ in a Ag foil extracted using single exponential fit to the beam off asymmetry. Inset: energy dependence of $1/T_1$ in Ag/YBCO at 10 K.

increase in the relaxation rate as energy increases, i.e. more $^8\text{Li}^+$ stops in YBCO. It may be of interest to study this signal as a function of field and temperature in a YBCO film or crystal without Ag to draw conclusions about the origin of this signal.

D.4 PCCO

The spin relaxation measured in a 300 nm thick PCCO film grown on STO shows a very small signal, and a fast relaxation. This is plotted in Fig. D.6. This suggests the existence of large dipolar fluctuating fields in PCCO, likely due to the magnetic moments associated with Pr or Cu atoms.

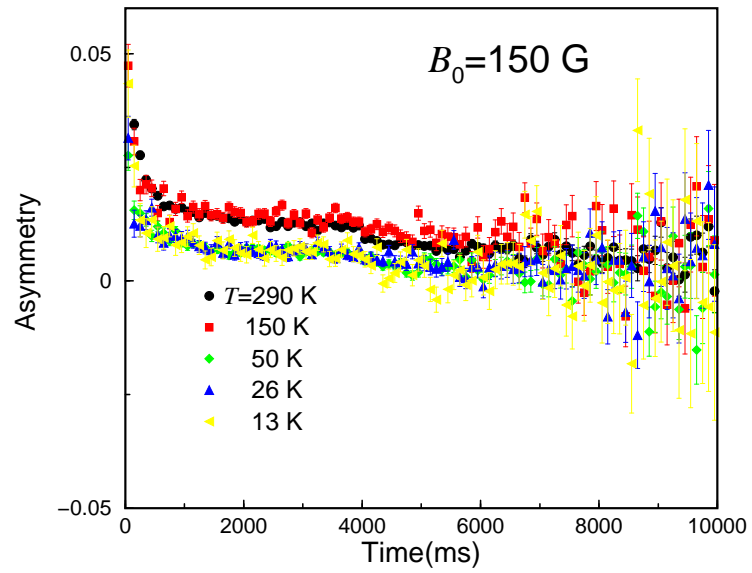


Figure D.6: The Spin relaxation of ${}^8\text{Li}^+$ at full energy implanted into a 300 nm thick PCCO film, in $B_0 = 150$ G.

Appendix E

Sample Characteristics

In this thesis, we have studied several near optimally-doped cuprate superconductors. In Chapter 2, four YBCO samples were studied. The (110)-oriented film was grown on an SrTiO₃ substrate using off-axis RF magnetron sputtering by P. J. Hentges and L. H. Greene at the University of Illinois. The film has a T_c of 84.5 K, an area of $\sim 4 \times 8$ mm, and a thickness of 100 nm. Another sample from the same group was studied. It is (001)-oriented, of $T_c=88.7$ K, size 4×8 mm, and thickness 100 nm. Two other c-axis films were studied. They are provided by a commercial supplier (Theva, Ismaning, Germany). The films are grown using thermal co-evaporation on LaAlO₃ substrates, have T_c of 88 K, and thickness of 600 nm.

In Chapter 3 we studied three YBCO samples. The YBCO crystals were flux-grown by Ruixing Liang, D. A. Bonn, and W. N. Hardy at the University of British Columbia. These crystals are $\sim 2 \times 3$ mm, ~ 0.5 mm thick, and have a T_c of 92.5 K. The results presented in Chapter 3 were taken on these crystals which were capped with 120 nm of Ag (99.99% purity). Also studied in Chapter 3 is a YBCO film (Theva) of 600 nm thickness and $T_c = 88$ K. The film was covered in-situ with 60 nm of Ag (99.99% purity).

The PCCO film (300 nm thick) studied in Chapter 4 was grown by P. Fournier at the University of Sherbrooke using Pulsed Laser Deposition (PLD) on an SrTiO₃ substrate. The film was covered with 40 nm of Ag.

The Ag deposition on all these samples is done ex-situ (except one Theva sample) at room temperature using DC sputtering in an Ar pressure $P_{Ar} = 30$ mtorr. A calibrated thickness monitor is used, with a deposition rate of 0.5 to 1 Å/s, and the growth is done while rotating the sample. A summary of the characteristics of all these samples is given in table E. More details are given in the chapters. Note that the AFM on the YBCO crystals was

Appendix E. Sample Characteristics

done more than two years after the Ag was deposited. Hence, because of the aging effect in Ag (see Section B.2), the estimated roughness is higher than the actual roughness at the time of experiments, which were done few weeks after the silver was deposited.

Sample	Type	Substrate	Lab	T_c (K)	d	Area (mm)	d_{Ag} (nm)	R_a (nm)
YBCO	TW xtal	-	UBC	92.5	≈ 0.5 mm	3 \times 3	120	12.8
YBCO	DTW xtal	-	UBC	92.5	≈ 0.5 mm	2 \times 3	120	47
YBCO	(001)	SrTiO ₃	Theva	87.5	600	10 \times 8	60	-
YBCO	(110)	SrTiO ₃	Urbana	86.7	100	8 \times 6	15	-
YBCO	(001)	SrTiO ₃	Urbana	88.7	100	5 \times 4	15	-
YBCO	(001)	LaAlO ₃	Theva	88	600	10 \times 8	15	2.4
YBCO	(001)	LaAlO ₃	Theva	88	600	10 \times 8	50	-
PCCO	(001)	SrTiO ₃	Sherbrooke	22.5	300	10 \times 8	40	-
Ag	-	SrTiO ₃	AMPEL	-	-	10 \times 8	15	2.7
Ag	-	SrTiO ₃	AMPEL	-	-	10 \times 8	15	5.5
Ag	-	SrTiO ₃	AMPEL	-	-	10 \times 8	15	17.9

Table E.1: Characteristics of the samples used in thesis thesis. TW: twinned crystal, DTW: detwinned crystal. d is the nominal thickness of the films, d_{Ag} the thickness of deposited Ag if applicable, and R_a the RMS surface roughness of the samples after Ag was deposited found measured by AFM.